Department of Precision and Microsystems Engineering

Demonstrator setup for semi-active control of a hydrodynamic journal bearing lubricated with magnetorheological fluid

M.J. Loonen

Report no	: 2024.065
Coach	: G.H.G. van der Meer
Professor	: R.A.J. van Ostayen
Specialisation	: Mechatronic System Design
Type of report	: Master of Science Thesis
Date	: 15 August 2024

TU Delft Delft University of Technology

Challenge the future

Demonstrator setup for semi-active control of a hydrodynamic journal bearing lubricated with magnetorheological fluid

by

M.J. Loonen

to obtain the degree of Master of Science
at the Delft University of Technology,
to be defended publicly on Thursday August 15, 2024 at 13:00.

Student number:	4666615	
Project duration:	September, 2023 – August, 2024	
Thesis committee:	Ir. G.H.G. van der Meer	TU Delft, daily supervisor
	Dr. ir. R.A.J. van Ostayen	TU Delft, supervisor
	Dr. R. Delfos	TU Delft
	Dr. ir. G. Radaelli	TU Delft

TU Delft

Abstract

In a hydrodynamic journal bearing, the lubricant is pressurized by the relative movement of the bearing surfaces, creating a load-carrying capacity. The load-carrying capacity can be increased by using a lubricant with higher viscosity, at the cost of increased friction. A proposed method to increase the maximum load-carrying capacity, while not increasing the friction at lower loads (or at higher speeds), is by using magnetorheological (MR) fluid as lubricant and electromagnets to generate a magnetic field. MR fluid consists of a carrier fluid with micron-sized magnetic particles suspended. Under the influence of an external magnetic field, the viscosity of the fluid increases as the particles form chain-like structures. Using electromagnets, the magnetic field strength can be adjusted based on the operating conditions of the bearing and the bearing can be semi-actively controlled.

The objective of this thesis is to create a visual demonstrator setup, intended for educational purposes, that can be used to investigate the pressure distribution and generated forces in a hydrodynamic half journal bearing using MR fluid and electromagnets. Furthermore, the research objective is to increase the maximum load capacity for a specified minimum film thickness, while not increasing the friction in the hydrodynamic lubrication regime. The test setup was based on an existing setup made by GUNT which is able to show the pressure distribution in a half journal bearing using pressure tubes for various eccentricity ratios. Adaptations to this setup were made to measure the generated forces (horizontal force, vertical force and friction force, defined as the frictional moment divided by the radius of the bearing) and to implement an electromagnet. First, experiments using hydraulic oil were performed to test and improve the performance of the setup. Afterwards, experiments using MR fluid were performed with varying magnetic field strengths. Furthermore, a numerical model based on the two-dimensional Reynolds equation was created and validated with the experimental results.

Both the numerical and experimental results showed comparable trends of increasing pressure, horizontal force and vertical force, meaning an increasing load capacity, for increasing eccentricity ratio and applied current. The numerical friction force also increased with increasing eccentricity ratio and applied current, while the experimental friction force only increased with increasing applied current and did not show a clear trend with increasing eccentricity ratio. The magnitude of the forces differed significantly between the experimental and numerical results, where the largest differences were observed for the vertical force and the friction force. Many plausible causes for the differences are identified, such as bearing tolerances, uncertainties in eccentricity and modeling simplifications. A combination of these causes is believed to lead to the observed differences. The increase in pressure, horizontal force and vertical force due to an increase in applied current was found to be much smaller experimentally than numerically. This was thought to be caused by a larger temperature increase in the experimental tests than was modeled and by simplifications used in the numerical model such as neglecting the shear-thinning characteristics of MR fluids. The friction force differed even more significantly between the numerical and experimental results. Additionally, this is caused by the small magnitude of the friction force in combination with a test setup that is not accurate enough to measure small forces consistently.

The created setup can show the change in pressure distribution when the applied current or eccentricity is changed. It therefore serves as a visual demonstrator setup for an MR lubricated hydrodynamic half journal bearing which can be used for educational purposes. However, demonstrator performance was found to be far from ideal as the changes in fluid column height were very slow because of the high MR fluid viscosity. Performance can potentially be improved by using a different or diluted MR fluid.

Despite the large differences between the numerical and experimental results, both can be used to display the potential of semi-active control using MR fluid and electromagnets. It is shown that the maximum load capacity can be increased while not increasing the friction coefficient in the hydrodynamic lubrication regime.

Several recommendations have been made for changes to the demonstrator setup to improve performance while keeping the setup simple and elegant. The main recommendations include improving the bearing tolerances, testing with a different or diluted MR fluid, implementing capacitive distance sensors and performing experiments at a more consistent ambient temperature.

Acknowledgements

Almost a year ago I started this thesis project which is almost coming to an end. It has been a year with many ups and downs, but most importantly, it has been a massive learning experience. Tackling all the challenges faced during this project would not have been possible without the support of others. Therefore, I would like to express my gratitude here.

To start, I would like to thank my daily supervisor Gerben van der Meer. Your feedback, critical questions and help during our weekly meetings really helped me solve the challenges I faced and pushed me into critically looking at my own work. Furthermore, your optimism when I showed you my experimental results even though I thought the experiments failed really helped me push through. Moreover, I would like to thank Ron van Ostayen for being my supervisor, giving extremely helpful feedback and interesting discussions.

Next, I would like to thank my friends and family for the mental support they provided me with. Daily discussions with Gijs van Veen and Daan Witte during lunch about each other's theses really helped to get some fresh ideas. Furthermore, I would like to thank my girlfriend Janniek Duisenberg who listened to my struggles, complaints and breakthroughs for almost an entire year while continuously supporting me. Lastly, I would like to thank my parents for their continuous support throughout the course of my studies.

Thank you all for your support and I hope you enjoy reading it.

M.J. Loonen
Delft, August 2024

Nomenclature

Abbreviations

Symbol	Definition	Unit
A	Magnetic vector potential	[Wb/m]
A	Area of the coil	[m^2]
a	Radius of particle	[m]
B	Magnetic flux density	[T]
c_f	Transformation constant	[1/Pa]
D	Shaft diameter	[m]
D_t	Diameter of pressure tube	[m]
$d_{wire,coil}$	Diameter of coil wire	[mm]
E	Modulus of elasticity	[Pa]
e	Eccentricity	[m]
$\mathbf{e}_{coil}$	Vector field that represents the coil	[-]
e_X	Eccentricity in X-direction	[m]
e_Y	Eccentricity in Y-direction	[m]
F_f	Friction force	[N]
F_h	Force measured by horizontal load cell	[N]
F_l	Force measured by left vertical load cell	[N]
F_{mag}	Magnitude of the force vector	[N]
F_{mr}	Magnetorheological force component	[N]
F_r	Force measured by right vertical load cell	[N]
F_v	Viscous shear force component	[N]
F_X	Horizontal force in X-direction	[N]
$F_{X,pressure}$	Horizontal force in X-direction due pressure	[N]
$F_{X,shear}$	Horizontal force in X-direction due shear force	[N]
F_Y	Vertical force in Y-direction	[N]
$F_{Y,pressure}$	Vertical force in Y-direction due pressure	[N]
$F_{Y,shear}$	Vertical force in Y-direction due shear force	[N]
f	Mass fraction	[-]
g	Gravitational constant	[m/s^2]
H	Magnetic field strength	[A/m]
H_0	External magnetic field strength	[A/m]
H_B	Bearing height	[m]
h	Film thickness	[m]
h_e	Local mesh element size	[m]
h_{fluid}	Fluid column height relative to tube inlet	[m]
$h_{fluid,external}$	Fluid column height relative to measurement threshold	[m]
h_{max}	Maximal film thickness	[m]
I	Moment of inertia	[m^4]
I_{coil}	Current through the coil	[A]
J	Current density	[A/m^2]
$\mathbf{J_e}$	Externally generated current density	[A/m^2]
$K_{compliant}$	Stiffness of the compliant joint	[N/m]
K_{eq}	Equivalent stiffness of the system	[N/m]
$K_{leafsprings}$	Stiffness of the leaf springs	[N/m]
k	Boltzmann constant	[-]
k_{AD}	Artificial diffusion coefficient in x-direction	[-]
$k_{AD,Y}$	Artificial diffusion coefficient in y-direction	[-]

Symbol	Definition	Unit
L_B	Bearing length	[m]
L_S	Shaft length	[m]
l	Lenght of flexure	[m]
M	Magnetization of the material	[A/m]
M_f	Frictional moment	[Nm]
$F_{f,bearing}$	Frictional moment at the bearing	[Nm]
$F_{f,shaft}$	Frictional moment at the shaft	[Nm]
Mn	Mason number	[-]
M_s	Saturation magnetization	[A/m]
m	Magnetic moment	[Am^2]
N	Surface speed	[m/s]
N_{coil}	Amount of coil windings	[-]
P	Load per unit length	[N/m]
Pe	Peclet number	[-]
P_{mr}	Magnetorheological pressure component	[Pa]
P_r	Viscous pressure component	[Pa]
p	Pressure	[Pa]
R_B	Bearing radius	[m]
R_S	Shaft radius	[m]
Rq	RMS of surface roughness	[m]
R_t	Radius of pressure tubes	[m]
T	Temperature	[K]
U	Velocity in x-direction	[m/s]
U_1	Velocity in x-direction of the shaft	[m/s]
U_2	Velocity in x-direction of the bearing	[m/s]
V	Velocity in y-direction	[m/s]
V_1	Velocity in y-direction of the shaft	[m/s]
V_2	Velocity in y-direction of the bearing	[m/s]
W_B	Bearing width	[m]
$w_{internal,i}$	Weight of lubricant in internal section of pressure tube i	[N]
$w_{tube,i}$	Weight of lubricant in straight section of pressure tube i	[N]
w_{yoke}	Width of the yoke	[m]
X	Global horizontal coordinate	[m]
x	Circumferential coordinate	[m]
Y	Global vertical coordinate	[m]
y	Axial coordinate	[m]
z	Coordinate in direction of film thickness	[m]
β	Contrast factor/coupling parameter	[-]
γ	Electromagnet angle	[°]
$\dot{\gamma}$	Shear rate	[1/s]
Δ	Film thickness parameter	[-]
ΔR	Nominal radial clearance	[m]
Δt_1	Tube inlet spacing large	[m]
Δt_2	Tube inlet spacing small	[m]
ϵ	Eccentricity ratio	[-]
ϵ_X	Eccentricity ratio in X-direction	[-]
$\epsilon_{X,a}$	Actual eccentricity ratio in X-direction	[-]
$\epsilon_{X,p}$	Prescribed eccentricity ratio in X-direction	[-]
ϵ_Y	Eccentricity ratio in Y-direction	[-]
η	Dynamic viscosity	[Pa·s]
η_f	Fluid viscosity	[Pa·s]
λ	Lambda	[-]

Symbol	Definition	Unit
μ	Friction coefficient	[-]
μ_0	Relative permeability of vacuum	[-]
μ_{BL}	Friction coefficient in boundary lubrication	[-]
μ_f	Relative permeability of fluid	[-]
μ_{HL}	Friction coefficient in hydrodynamic lubrication	[-]
μ_p	Relative permeability of particle	[-]
μ_r	Relative permeability of material	[-]
ξ	Variable used in the modified Reynolds equation	[Pa]
ρ	Density	[kg$/$m^3]
σ	Electrical conductivity	[S/m]
τ	Shear stress	[N$/$m^2]
Φ	Circumferential angle in the bearing	[rad]
Φ_{loss}	Friction loss	[Nm/s]
ϕ	Volume fraction	[-]
ω	Rotational velocity	[rpm]

Contents

1 Introduction

1.1. Background

In all devices with relative motion between components, friction and wear play a role. Lubricants are used to reduce friction and wear and ensure cooling. When the pressure in the lubricant film is large enough to carry the load, the mechanical components are fully separated by a fluid film. Mechanical contact is removed, which means that wear is avoided and friction is reduced.

One way of generating the required pressure in the fluid film is by means of hydrodynamic lubrication. When the bearing surfaces have sufficient relative velocity and relative angle, pressure will be built up generating a load capacity [1, 2]. At low speeds, the buildup pressure will not be large enough to sustain the load, causing mechanical contact which results in wear and a large increase in friction. When the speed is increased, the friction will decrease as a fluid film is built up (but surface imperfections will still come into contact). For even higher speeds, the friction coefficient comes to a minimum where full-film lubrication is present, after which it increases linearly with increasing speed. This is typically displayed in a Stribeck curve, which is shown in Figure 1.1. The point of minimum friction coefficient, where the bearing moves from mixed lubrication to full-film lubrication, is called the transition speed. During steady operation, hydrodynamic bearings operate in full-film lubrication; however, in applications where movement frequently stops or changes direction, contact of the bearing surfaces does occur. An example of such an application is the hydrodynamic bearing that supports the shaft of a ship that is maneuvering in a harbor. Full-film (or hydrodynamic) lubrication limits the friction coefficient to only $\mu = 0.001 - 0.01$ [1].

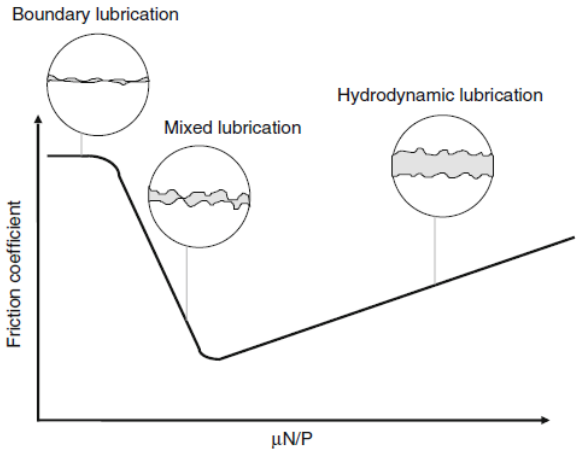

Figure 1.1: Stribeck curve plotting friction coefficient versus Hersey number. Taken from [3].

One method to ensure full-film lubrication for low speeds without increasing the friction coefficient at higher speeds is to actively change the properties of the lubricant using smart fluids. Magnetorheological and electrorheological fluids (MR/ER fluids) are smart fluids whose rheological properties change under the influence of an external magnetic and electric field respectively [4]. By applying and changing the external field, the apparent viscosity of the lubricant can be changed, influencing the load capacity (or transition speed, when the load is kept constant) and friction of the bearing. Increasing the viscosity increases the load capacity and thus reduces the transition speed. In contrast, a higher viscosity

increases friction in the full-film lubrication regime [1, 2]. Therefore, by using a smart lubricant and lowering or removing the external field after the transition to full-film lubrication, it might be possible to decrease the transition speed while maintaining (or even decreasing) the low friction in the full-film lubrication regime. Ideally, the external field can be adjusted in such a way (e.g. by using electromagnets) that the bearing operates at minimum friction for the specified load and bearing velocity (which is at the minimum film thickness in the hydrodynamic lubrication regime). Furthermore, the external field can be applied locally, so that the viscosity is only increased in the region where it is beneficial for pressure buildup [5, 6].

In a test setup where the eccentricity ratio is prescribed, it is not easy to experimentally measure the boundary and mixed lubrication regimes. Therefore, one could also only look at hydrodynamic lubrication and set a minimum film height (for example, an approximation of the film height for which mixed lubrication would start to occur). This minimum film height can then be used to investigate the maximum load capacity for a specific operating speed. This means that only the hydrodynamic regime of the Stribeck curve is investigated.

1.2. Problem definition and research objective

Existing literature on MR fluid application in hydrodynamic bearings has focused solely on a constant magnetic field strength (not changing with operating conditions) and reported an increase in both friction and load capacity when using MR fluids. Therefore, this thesis focuses on showing the potential to increase the load capacity for a specified minimum film thickness while minimizing friction for larger film thicknesses by changing the magnitude of the magnetic field. The research objective is formulated as follows.

Increase the maximum load capacity of a hydrodynamic half journal bearing for a specified minimum film thickness, while not increasing the friction in the hydrodynamic lubrication regime using MR fluid and electromagnets.

Furthermore, based on the gap in existing literature and to reach the research objective, several sub-objectives are defined:

1. Numerically investigate the friction and load capacity of a hydrodynamic half journal bearing lubricated with MR fluid for different magnetic field strengths and shapes and eccentricities.
2. Create a simple and visual experimental demonstrator setup to measure the friction, load vector and pressure distribution in a hydrodynamic half journal bearing lubricated with MR fluid where the applied magnetic field, eccentricity and operating velocity can be changed. The demonstrator setup should visually show the change in pressure distribution under influence of a changing magnetic field.
3. Use the experimental setup to measure the friction and load capacity and determine the maximum load capacity (at specified minimum film thickness) for different magnetic field strengths.
4. Measure the 'optimal' Stribeck curve by changing the magnetic field strength as a function of eccentricity.
5. Compare the theoretical and experimental results and thereby validate the numerical model.

Sub-objective 2 is especially interesting, as existing test setups for hydrodynamic bearings are generally complex to accurately measure the small friction forces. Furthermore, test setups in literature do not visually show the magnetorheological effect. The main goal of this thesis is to create an elegant test setup that can visually show the effect that a magnetic field has on the pressure distribution in the bearing while still being able to measure the generated forces accurately enough to prove that the research objective can be achieved. Such a setup can furthermore be used for educational purposes as the visual results allow for a quick understanding of the magnetorheological effect and the effect of the eccentricity ratio in a hydrodynamic bearing, while the measured forces can be used for a more thorough analysis and understanding of the investigated principles. Sub-objective 4 is related to the semi-active control of the hydrodynamic journal bearing. The current through the electromagnet is changed based on the (required) load capacity such that the friction coefficient is minimized. It is referred to as "semi-active" control as no significant amount of energy is injected into the system to

control the load capacity [7]. Only a magnetic field is introduced to change the viscosity of the MR fluid that indirectly controls the load capacity and the friction coefficient of the bearing.

1.3. Thesis layout

The thesis is structured as follows: First, the experimental setup is introduced in chapter 2. The experimental setup is based on an existing demonstrator setup made by GUNT. To enable testing with MR fluid and to measure the generated forces, many changes to the original setup have been made that are extensively covered. Chapter 3 covers the theoretical model used to model the magnetic field and fluid flow. The experimental and numerical results are presented in chapter 4, where the results are also interpreted and a comparison between the experimental and numerical model is made. Furthermore, possible causes for the differences between the model and the experiments are discussed. Finally, chapter 5 contains the main conclusions and recommendations for further research.

2
Experimental setup

To perform experimental tests and validate the numerical model, a test setup has been created. This chapter will first introduce the original demonstrator setup in section 2.1. The final setup which was created by making several changes to the original setup is covered in section 2.2. In section 2.3 some important parameter definitions are given, which will also be used in the numerical model introduced in chapter 3. The changes made to the original setup will be discussed in section 2.4. The methods used to determine the pressure distribution and generated forces based on the height of the fluid column and load cell measurements are described in section 2.5. The properties of the two lubricants used, including variations in fluid properties as a function of temperature, shear rate and magnetic field strength, are discussed in section 2.6. The experimental procedures will be covered in section 2.7 and finally the limitations of the created setup are discussed in section 2.8.

2.1. Original setup

The experimental setup is based on the Gunt TM260 setup. The TM260 is a drive unit for tribological investigations and can be connected to several different setups to perform tribological experiments. A picture of the TM260 is shown in Figure 2.1. It consists of a display and control unit (1) that acts as the power supply for the AC motor (2), allows for control of rotational speed using a potentiometer (3) and displays measured speed and friction force (4) (friction force measurement not used in the current test setup as it was not compatible with the hydrodynamic bearing attachment). Next to the display and control unit, it consists of a frame (5) on which the AC motor is mounted, that is connected to a gearbox (6) which is mounted on a swivel mechanism (7) to allow for horizontal and vertical positioning of the drive shaft. Some important parameters of the TM260 are given in Table 2.1. The frame also serves as mounting point for the attachment units; in this case this is the TM260.06, which is an experimental demonstrator module of a half journal bearing with pressure tubes to visually show the pressure distribution. The half journal bearing attachment will be described in more detail in the next subsection.

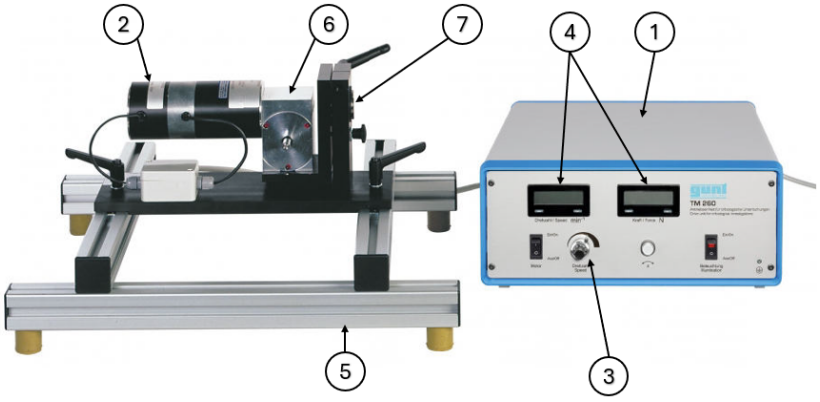

Figure 2.1: GUNT TM260, drive and display unit. 1 - Display and control unit, 2 - AC motor, 3 - Potentiometer for speed control, 4 - Display for speed and force, 5 - Frame, 6 - Gearbox, 7- Swivel mechanism. Taken and adapted from [8].

	Parameter	Value
Motor	Type	AC Motor
	Nominal speed	3600 [rpm]
	Torque	0.31 [Nm]
	Power	117 [W]
Gearbox	Type	Worm drive
	Transmission ratio	15 [-]
Speed Sensor	Type	Incremental rotary transducer
	Number of pulses	6 [per rev.]
	Output signal	0-5 V
Control unit	Power	0.25 [kW]
	Speed range	0-200 [rpm]

Table 2.1: Parameters of the TM260. Taken from [8].

2.1.1. Original demonstrator

The experimental test setup is directly based on the demonstrator module TM260.06 (the half journal bearing attachment) made by GUNT. Many adaptions have been made to this setup to allow for the implementation of the required load cells, MR fluid and an electromagnet. The unchanged original setup will first be introduced to familiarize the reader before going into detail of the changes made to create the experimental setup as used for the experiments in this thesis. A schematic drawing of the setup is given in Figure 2.2a, together with a schematic front view to show the mounting and possible movement of the bearing in Figure 2.2b. The setup is mounted on the frame (1) of TM260. A block (2) is placed under the oil pan (3) to ensure that the shaft is submerged in the oil. The bearing (4) is mounted on four leaf springs (5, see also Figure 2.2b) and the horizontal position can be changed by rotating the micrometer screw (6), which changes the bearing clearance or minimal film thickness (7). The shaft (8) is attached to the drive shaft using a jaw clutch (9). The shaft is supported by two ball bearings that are mounted in a block (10). The whole setup is mounted on a module board (11) which can slide on the frame and is secured using star knobs (12). 13 pressure tubes (13) are mounted on the bearing and have their inlets positioned along the perimeter of the bearing. The first inlet from the left is at 10° with respect to the horizontal. The next four inlets are graduated at 20° and the last eight are at 10° from each other. The distance from the bottom of the bearing to the top of the tubes is 360mm.

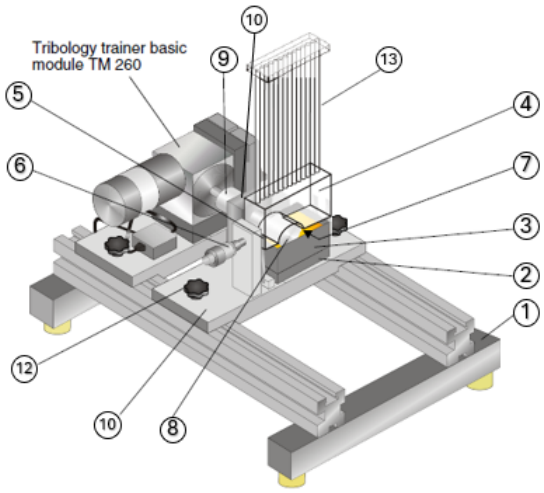

(a) 1 - Frame, 2- Block, 3 - Oil pan, 4 - Bearing, 5 - Leaf springs, 6 - Micrometer screw, 7 - Bearing clearance (minimal film thickness), 8 - Shaft, 9 - Jaw clutch, 10 - Block with two ball bearings to support the shaft, 11 - Module board, 12 - Star knob, 13 - Pressure tubes.

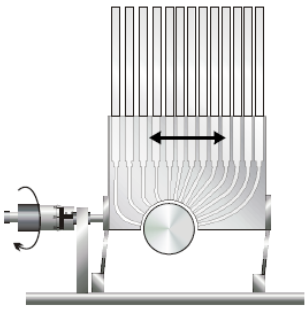

(b) Front view of the setup. Arrows indicate rotation of the micrometer screw introduces horizontal movement of the bearing.

Figure 2.2: Schematic drawings of the GUNT TM260.06. Taken and adapted from [9].

During operation, the shaft will spin clockwise, dragging the lubricant along into the bearing toward the minimal film thickness. The fluid will flow into the pressure tubes visualizing the pressure distribution and some fluid will also flow back into the oil pan while new oil is dragged along into the bearing.

2.2. Final setup

As the original setup was not meant for testing with MR fluid and only included a way to visualize and measure the pressure distribution (and not measure any generated forces), several changes were made to the setup. The final test setup is introduced in this section, while a detailed explanation of the required modifications, including reasoning, is given in section 2.4. The final setup is shown in Figure 2.3 and Figure 2.4. The main differences, which can be seen in Figure 2.4, are the implementation of three load cells (one to measure the horizontal force (4) and two to measure the vertical force (6)), a compliant joint (3) between the micrometer screw and the bearing and the implementation of an electromagnetic consisting of a yoke (13) and a coil (14). The most important parameters of the setup are given in Table 2.2. For the definition of some of the parameters the reader is referred to section 2.3.

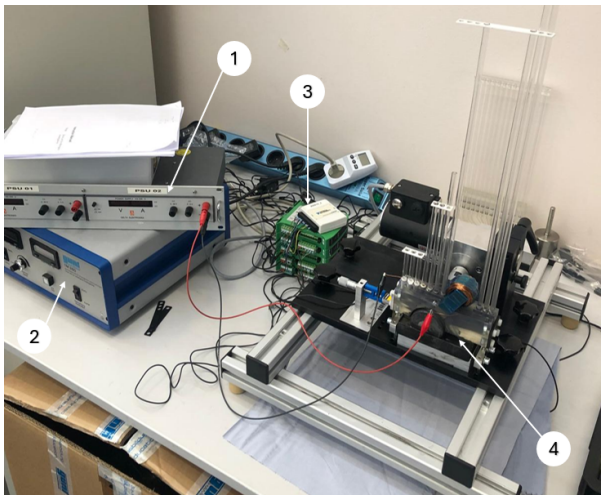

Figure 2.3: Overview of the experimental setup. 1 - Power supply for electromagnet, 2 - Display and control unit, 3 - Data acquisition system, 4 - Demonstrator test setup.

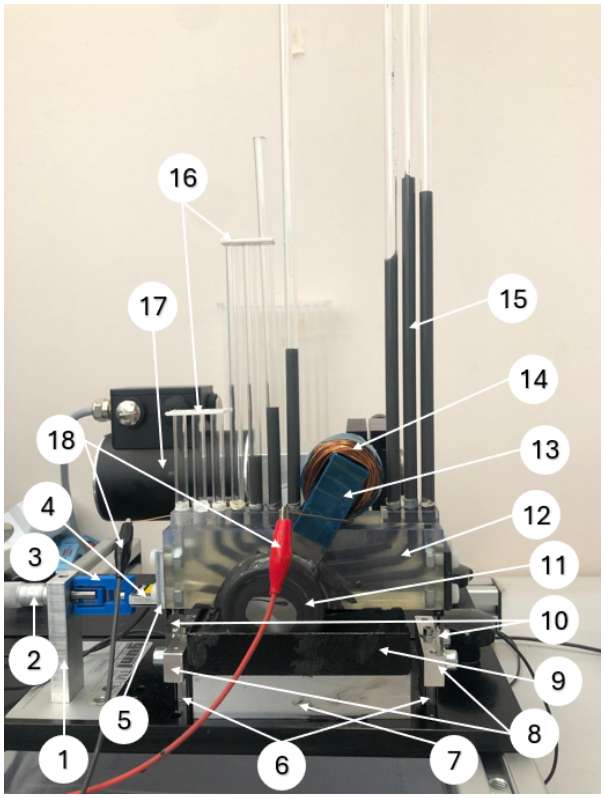

Figure 2.4: Detailed picture of the front of the experimental test setup. 1 - Micrometer stand, 2 - Micrometer screw, 3 - Compliant joint, 4 - Horizontal load cell, 5 - Spring clamp, 6 - Vertical load cells, 7 - Block, 8 - Spring holders, 9 - Oil pan, 10 - Leaf springs, 11 - Shaft, 12 - Bearing, 13 - Electromagnet yoke, 14 - Coil, 15 - Pressure tubes (displayed here during operation with MR fluid), 16 - Tube supports, 17 - AC motor, 18 - Wires connecting coil to power supply.

Parameter	Symbol	Value
Bearing radius	R_B	26.25 [mm]
Shaft radius	R_S	25 [mm]
Radial clearance	ΔR	1.25 [mm]
Rotational speed	ω	50 [rpm]
Eccentricity in X-direction	e_X	0.63 - 0.94 [-]
Eccentricity in Y-direction	e_Y	-0.06 [-]
Diameter of pressure tubes	D_t	5 [mm]
Shaft length	L_S	50 [mm]
Bearing length	L_B	39.6 [mm]
Bearing width	W_B	140.2 [mm]
Bearing height	H_B	40.2 [mm]
Tube inlet spacing large	Δt_1	$\frac{20}{180}\pi R_B$ [mm]
Tube inlet spacing small	Δt_2	$\frac{15}{180}\pi R_B$ [mm]
Amount of coil windings	N_{coil}	360 [-]
Electromagnet angle	γ	30°
Current through coil	I_{coil}	0-1.2 [A]
Amount of pressure tubes	N_{tubes}	10 [-]

Table 2.2: Overview of parameters of the setup and operating conditions.

2.3. Setup definitions

In order to explain the changes made to the original demonstrator setup, the reader is first introduced to some definitions. These definitions will later also be used in the theoretical model as described in chapter 3.

A two-dimensional schematic sketch of the setup is given in Figure 2.5 and Figure 2.6. The setup consists of a half journal bearing with a rotating shaft having a defined eccentricity e_X and e_Y. X and Y define the global coordinate system. O_b and O_s are the center of the bearing and shaft respectively. Φ defines the angle (from 0 to π) around the perimeter of the bearing, starting from zero on the left side of the bearing, while $x = \Phi R_B$ (with R_B being the radius of the bearing) defines the position around the perimeter of the bearing. The axial direction is defined with variable y, while the direction of the film thickness (h) is defined with variable z (z = 0 corresponds to the shaft surface and z = h corresponds to the bearing surface). ω denotes the rotational velocity and the rotational direction of the shaft. The position of the electromagnet is shown to indicate how the magnet angle γ is defined. Furthermore, the final setup only has 10 pressure tubes that are numbered 1-10 starting from the pressure tube on the left side. The length of the bearing in axial direction is defined by L_B. Finally, the diameter of the pressure tubes is given by D_t while the spacing of the pressure tubes is given as Δt_1 and Δt_2.

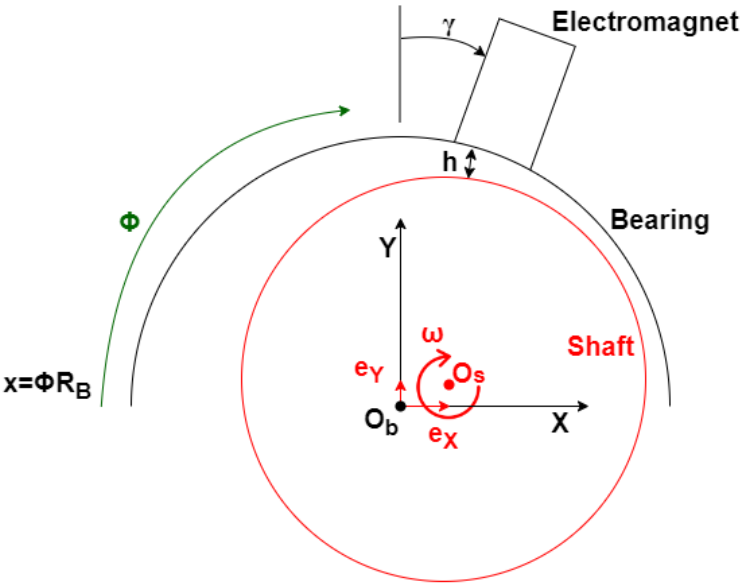

Figure 2.5: Schematic sketch of the two-dimensional setup (front view).

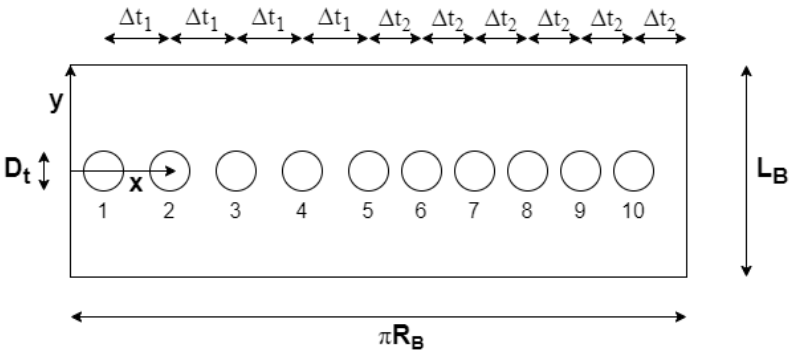

Figure 2.6: Schematic of the flattened two-dimensional bearing setup.

The location of the shaft with respect to the bearing is defined using the eccentricity ratio in the X- and Y-directions. The eccentricity ratio is defined as $\epsilon = \frac{e}{\Delta R}$, where $\Delta R = R_B - R_S$ is the difference between the bearing radius and the shaft radius and e is the eccentricity. An eccentricity ratio of zero means that the shaft is centered in the bearing and ϵ = 1 means that the shaft is touching the bearing. In the experimental setup ϵ_Y (eccentricity ratio in Y-direction) will be set as close as possible to zero (which resulted in $\epsilon_Y = -0.06$), while ϵ_X (eccentricity ratio in X-direction) will be varied in the range of 0.63-0.94.

2.4. Changes to the original demonstrator setup

The modifications made to the original demonstrator setup to create the final setup that is used for the experiments in this thesis (as introduced in section 2.2) will be elaborated on in this section.

2.4.1. Design of the electromagnet

In order to apply and change the magnetic field in the fluid film, an electromagnet was designed and implemented. The goal of the electromagnet design was to have a fairly uniform magnetic field in the fluid gap. The electromagnet was based on the design of Moles [10], where the yoke is U-shaped and the coil is wound around the middle of the yoke. The reasons for the selection of this design are the symmetric magnetic field in axial direction, ease of implementation into the existing setup and the relatively strong and uniform magnetic field across the fluid film. Furthermore, this electromagnet design results in a magnetic field that is comparable to what is used in most literature (either created with permanent magnets or electromagnets). In contrast to Moles [10], it was decided to apply only a local magnetic field just before the minimum film thickness, as it was found by Quinci et al. [5] and Van der Meer et al. [6] that a local magnetic field could increase the load capacity while minimizing the increase in friction coefficient. Similar results were found by Moles [10] when he applied the magnetic field to only the converging section of the bearing and still managed to increase the load capacity. The dimensions of the yoke were driven primarily by the design of the bearing as described in subsection 2.4.2, since the electromagnet had to fit around the bearing while leaving enough space for the pressure tubes. The width of the electromagnet was limited by the width of the bearing while the distance between the two 'legs' of the yoke had to be sufficiently large for the coil. For the coil, the trade-off is between a large amount of windings with a thin wire or a thicker wire with less windings. The advantage of a relatively thin wire is the ease of winding the coil and due to the larger amount of windings, the required current is smaller. The advantage of a larger diameter wire is that a smaller voltage is needed due to the smaller resistance and due to the lower amount of windings it is quicker to produce (when winding is done by hand). A 0.5mm diameter copper wire was selected as this was a good compromise between amount of windings, ease of winding and required current and voltage. The details of the electromagnet are summarized in Table 2.3 and a technical drawing of the electromagnet can be found in Figure H.1. The shape and placement of the electromagnet in the setup are shown in Figure 2.4 and Figure 2.8.

To make sure the magnetic field is fairly uniform in the fluid gap and to create a strong magnetic field, a ferromagnetic shaft is required. Urreta et al. [11] showed both numerically and experimentally that a magnetic shaft was required to have a significant increase in load capacity when a magnetic field is applied and Moles [10] also demonstrated a magnetic shaft is required to achieve the required magnetic field strength. As the original shaft was made of nonmagnetic stainless steel, a new shaft was manufactured from ferromagnetic bright steel. No other changes to the shaft design were made.

The electromagnet was connected to a Delta Elektronika power supply ES 030 - 5, which could deliver up to 10A and 30V, and where maximum current and voltage can be set. For the experiments, the amperage was controlled and varied between 0 and 1.2 A.

Parameter	Symbol	value
Amount of coil windings	N_{coil}	360 [-]
Wire diameter	$d_{wire,coil}$	0.5 [mm]
Material	-	(Ferromagnetic) bright steel

Table 2.3: Most important parameters of the electromagnet.

2.4.2. Design of the bearing

To allow an electromagnet to be fitted to the setup, a new bearing had to be designed. The outer dimensions of the bearing were kept equal to the bearing in the original configuration. The first step was to determine the angle at which the electromagnet would be mounted (γ), with the goal being a large increase in load capacity (as a result of the generated magnetic field) and ease of implementation. The magnet angle γ is defined as previously shown in Figure 2.5. Using the numerical model which will be elaborated on in chapter 3, Figure 2.7 is created which plots the Stribeck curves for constant speed and a constant magnetic field strength where the angle of the electromagnet with respect to the vertical γ is varied. To vary the load capacity for a specific angle of the electromagnet (and thus create the Stribeck curves), the horizontal eccentricity ratio ϵ_X is varied between 0.6 and 0.92. Furthermore, the Stribeck curve where no magnetic field was present is also plotted, which can be used as a baseline.

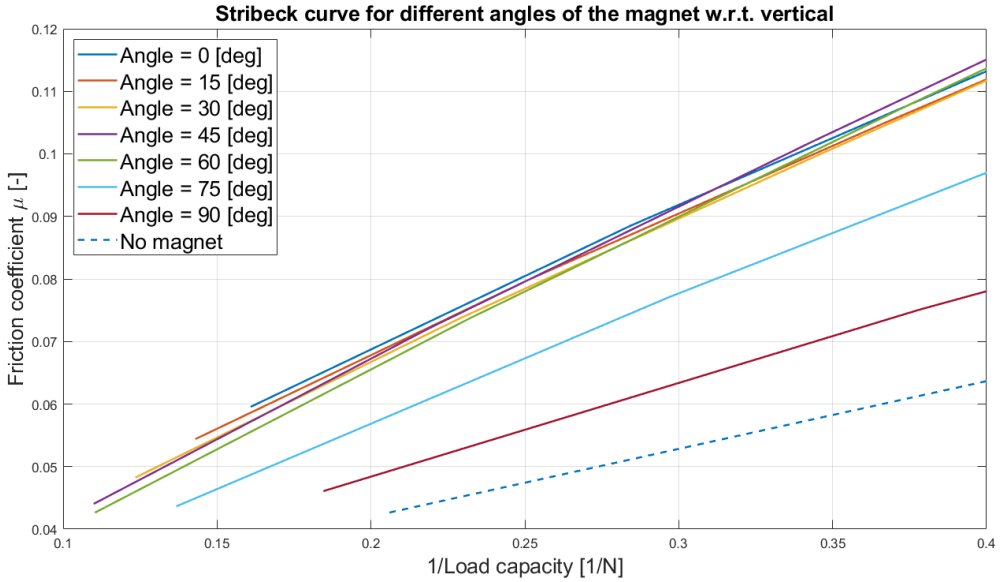

Figure 2.7: Stribeck curve for different magnet angles and constant speed.

For a low eccentricity ratio, the load capacity is small and the friction coefficient is relatively large, which is the case on the right side of the individual curves (as on the x-axis the inverse of the load capacity is plotted). For an increasing eccentricity ratio, the load capacity increases and the friction coefficient decreases, which can be seen as the curves decrease when moving towards the left. The maximum load capacity for the maximum eccentricity ratio of 0.92 (corresponding to a minimum specified film thickness) is the most left point of each individual curve. Compared to the baseline curve where no magnet is present, it can be seen that the Stribeck curves for all values of γ are moved to the left, indicating an increase in maximum load capacity. However, they also moved upward, indicating an increase in friction coefficient. The optimal angle is where the maximum load capacity is increased most, while the friction coefficient increase is kept as low as possible (meaning a Stribeck curve that is located most toward the left while being as low as possible). From this logic, the magnet angle that performs best is 60°, followed by 45° and 30°, where 45° performs better in terms of maximum load capacity, but 30° has a lower friction coefficient for decreasing load capacity. Ideally, the chosen magnet angle would thus be 60°; however, due to the relatively large angle, this would be difficult to integrate mechanically into the setup. The reason for this becomes clear when you look at the entire bearing assembly as shown in Figure 2.8.

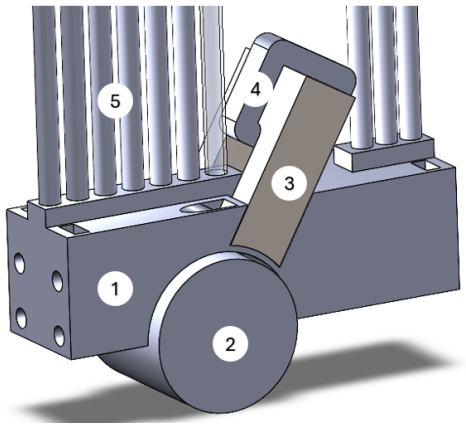

Figure 2.8: The bearing assembly. 1 - Bearing, 2 - Shaft, 3 - Electromagnet yoke, 4 - Coil, 5 - Pressure tubes.

If the angle was set to 60°, the electromagnet would have to be very long to protrude above or to the side of the bearing, which is needed due to the U-shape of the electromagnet. Increasing the length of the electromagnet decreases the efficiency of the yoke significantly. Similar reasoning is true for the 45° angle, so a compromise was made to select a magnet angle of 30°. Ideally, several magnet angles would have been implemented in the bearing design; however, due to space requirements for the pressure tubes and time limitations on making and testing several bearings, this was omitted for this thesis. Furthermore, this analysis was performed without taking the effect of eccentricity on the magnetic field strength into account and was only performed for a single current setpoint (through the electromagnet coil) and is therefore not a complete analysis to determine the optimal electromagnet angle. Optimizing the magnetic field shape and strength for specific operating conditions by determining the optimal electromagnetic angle, electromagnet shape and perhaps even amount of electromagnets is therefore kept as a recommendation for further research.

The next design choice was on the implementation of the pressure tubes. As the MR fluid has a relatively high viscosity it does not flow well through the small pressure tubes. In the original setup the internal tubes (the curved tubes going through the bearing) have a diameter of 3mm. To increase the flow rate into the tubes, the diameter of the internal tubes was increased to 5mm, equal to the internal diameter of the straight tubes on top of the bearing (the straight tubes that were mounted into the bearing). Due to the implementation of the electromagnet, less space was available for pressure tubes. Therefore, the number of pressure tubes was reduced to 10 (as also shown in Figure 2.6). The first inlet from the left is at 10° with respect to the horizontal. The next four tube inlets are graduated at 20° and the last five are at 15° from each other. The length of the straight tubes was determined on the basis of the expected pressure as calculated with the numerical model. The tube lengths are summarized in Table 2.4. The acrylic tubes have an internal diameter of 5mm and an outer diameter of 7mm. Using Teflon tape, they are slid into the bearing to make a leak-tight connection. Some simple 3D-printed supports were slid around the tubes to connect them to each other and provide stability.

Tube number	Length [cm]
1	6
2	6
3	6
4	15
5	15
6	20
7	40
8	55
9	70
10	90

Table 2.4: Length of the pressure tubes. Numbering of pressure tubes as shown in Figure 2.6.

Due to the complex internal pressure tubes, angled cutout for the electromagnet and speed of production, it was decided to manufacture the bearing using stereolithography 3D printing. The bearing was printed with a Formlabs Form 3 printer with an accuracy of $\sim 30 - 100\mu m$ and made from clear resin so that lubricant could be seen in the internal pressure tubes of the bearing. This accuracy is not sufficient for most hydrodynamic bearings, but since the radial clearance of the setup is 1.25mm this is sufficient. The critical region of the printed bearing is the half circular bearing shape, as a small error (e.g. in the range of $\pm 100\mu m$) would have a significant effect on bearing performance. Therefore, to account for the exact shape including the accuracy of the printed bearing, it was decided to perform two 2D measurements of the printed bearing surface and use this as input for the numerical model (see subsection 3.1.4). In this way, although the printed bearing might not be a perfect circular shape with a constant and correct radius, the model and experimental setup will represent the same bearing shape. The bearing assembly including pressure tubes and electromagnet is shown in Figure 2.8. Furthermore, a cross-sectional view of the bearing is shown in Figure 2.9 to show the internal pressure tubes of the bearing. Note the larger radius of the tubes at the top of the bearing, which allows the straight external pressure tubes to be slid into.

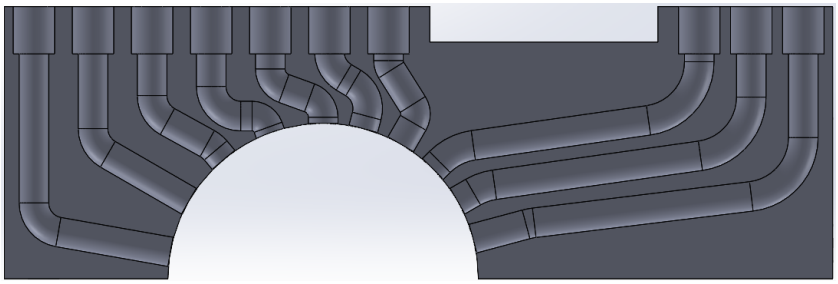

Figure 2.9: Cross-sectional view of the bearing (part 1 in Figure 2.8) showing the internal pressure tubes.

2.4.3. Load cell implementation

Next to the pressure measurements performed using the pressure tubes, the generated forces on the bearing need to be measured. In order to do this, three load cells were integrated into the setup. The selected load cells were Futek LSB 200 load cells. One load cell was placed between the bearing and the micrometer screw (to measure the horizontal force) and the other two were placed between the blocks the leaf springs were mounted on (these are referred to as "spring holders") and the module board (to measure the vertical load). The placement of the load cells is also indicated in Figure 2.4. The horizontal load cell was calibrated at a range of $\pm$45N and the vertical load cells were calibrated at a range of $\pm$8.9N. The load cells were connected to a National Instruments USB-6008 data acquisition device. This is a 12-bit acquisition device, resulting in a step size (and thus uncertainty) of $\pm\frac{45}{2^{(12-2)}} = 0.044$N in horizontal force and $\pm\frac{8.9}{2^{(12-2)}} = 0.0087$N in vertical force (as 1 bit is used for defining the sign, meaning tension or compression, of the force). A data acquisition device with more bits would allow for a lower uncertainty; however, the noise due to misalignment of the shaft and bearing and the vibrations introduced caused a larger uncertainty than the step size. As the forces were averaged over a period of 30 seconds (see section 2.7) and the fluctuations in force during these intervals were larger than the step size (fluctuations of at least 3-4 steps), the introduced error should not be dominated by the uncertainty due to the discrete step size.

The introduction of these three load cells required multiple additional modifications of the setup. Firstly, the spring holders needed an extra hole to mount the load cells. For the attachment of the load cells to the module board, new holes were also made in the module board. The goal of the two vertical load cells is to be able to measure not only the vertical force generated, but also to calculate the friction force by using the relative distance of the two load cells and the difference in vertical force measured. To minimize the effect of the horizontal force exerted by the micrometer screw on the measured moment, the horizontal load cell was placed directly in line with the bottom of the bearing (such that the horizontal force acts through the center of the bearing and thus does not influence the frictional moment). For the attachment of the load cell to the bearing, a custom piece was manufactured whic will be referred to as 'spring clamp'. To ensure that the micrometer screw aligned with the load cell and the bottom of the

bearing, the micrometer screw stand needed to be lowered (and thus a new part was manufactured). The last modification had to be made to the leaf springs. Due to the implementation of the vertical load cells the bearing was raised. To ensure that the relative height of the bearing with respect to the shaft did not change, the leaf springs were shortened. To compensate for the increase in stiffness of the leaf springs (due to the decrease in length), the thickness of the leaf springs was decreased. The thickness of the leaf springs was reduced from 0.5mm to 0.25mm. An explanation of the determination of the thickness of the leaf springs is given in Appendix A.

Friction at the micrometer screw
During testing it was discovered that the interface between the micrometer screw and the horizontal load cell introduces friction which takes up part of the vertical force. This introduces uncertainty and an incorrect measurement of the vertical force. To minimize this friction force, the effectiveness of two potential mitigating measures was investigated. The first option was to slightly push against the bearing during operation to temporarily reduce the normal force and potentially remove the elastic deformation at the interface that causes the friction force. The second option was to introduce a compliant joint between the micrometer screw and the horizontal load cell. A simple test was performed to test the effectiveness of these methods, which is elaborated on in Appendix B. The conclusion was that with the introduction of a compliant joint, the error introduced in the vertical force measurement was reduced to about 1%. The compliant joint was 3D printed from PET-G and the technical drawings of the part can be found in Figure H.2.

2.5. Determination of the generated forces

The purpose of the measurements was to determine the load capacity, friction force and pressure distribution for different values of horizontal eccentricity e_x and magnetic field strength H (only for measurements with MR fluid). The pressure in each tube was calculated using Equation 2.1, where p is the pressure, ρ the density of the lubricant, h_{fluid} the height of the fluid column measured from the tube inlet and g the gravitational constant.

$$p = \rho g h_{\textit{fluid}} \tag{2.1}$$

The horizontal and vertical forces based on the measured forces are calculated as in Equation 2.2 and Equation 2.3 respectively, where F_h is the force measured by the horizontal load cell, F_l is the force measured by the left vertical load cell and F_r the force measured by the right load cell, $w_{tube,i} = h_{fluid,external} A_{tube} \rho g$ is the weight of the fluid column in the straight (external) section of pressure tube i (where $h_{fluid,external}$ is measured relative to the measurement threshold) and $w_{internal,i} = V_{internal,i} \rho g$ (with $V_{internal,i}$ being the volume of the internal section of pressure tube i) is the weight of the fluid in the internal section of the pressure tube (inside the bearing). See also Figure 2.10 for the location of the force vectors. Note that $w_{internal,i}$ is only added when $w_{tube,i}$ for the same tube is larger than zero (the fluid column protrudes above the measurement threshold), which will be explained below.

$$F_X = -F_H \tag{2.2}$$

$$F_Y = -F_l - F_r + \sum_{i=0}^{10} w_{tube,i} + \sum_{i=0}^{10} w_{internal,i} \tag{2.3}$$

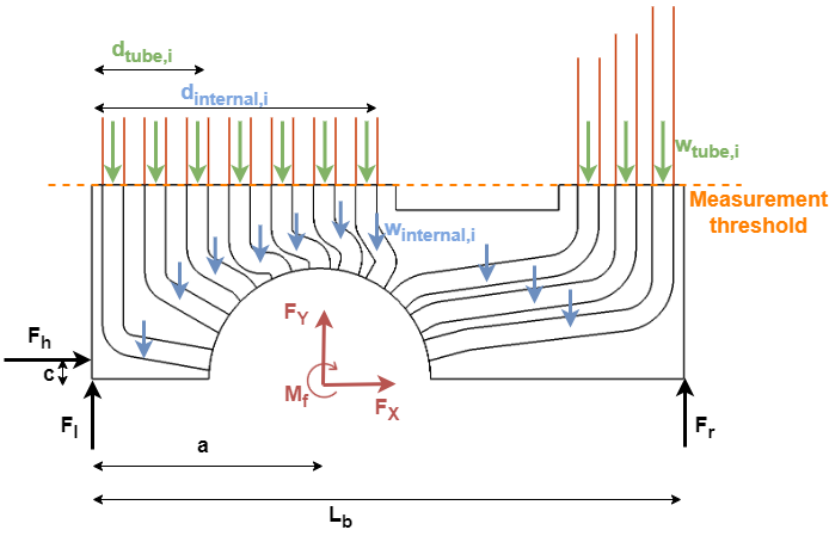

Figure 2.10: Two-dimensional free body diagram of the experimental setup (front view of the setup). Location of the $w_{internal,i}$ arrows is only indicative. External pressure tubes are shown in orange.

The horizontal force was measured using the horizontal load cell and the vertical force using the sum of the forces measured by the two vertical load cells. However, the vertical force is also affected by the weight of the lubricant in the pressure tubes as a result of the bend of the tubes. As the inlet is at an angle that depends on its location on the bearing surface, the lubricant pressure pushes against the tube (and thus the bearing) under an angle. This force is equal to the force that would have been pushing on the bearing if the tube had not been there. However, the weight of the lubricant pushes straight down onto the bearing and this force would not have been present if the tube was not there (this situation is comparable to the force of an incompressible fluid on a pipe bend as described by Phay et al. [12]). This downward force means that the upward vertical force measured by the load sensors is smaller than the upward hydrodynamic force we are interested in. To compensate for the weight of the fluid, the vertical force is adjusted by adding the approximated weight of the lubricant in the pressure tubes, using the measured height of the fluid column. The weight of the fluid within the bearing $w_{internal,i}$ (in the curved tubes) is added separately from the weight of the fluid in the straight (external) pressure tubes $w_{tube,i}$. The weight of the fluid within the curved tubes in the bearing was only included once the fluid rose above the "measurement threshold" as indicated in Figure 2.10 (the "measurement threshold" also indicates the division between the internal section of the pressure tubes and the external section of the pressure tubes). If the fluid level was below the measurement threshold, it was impossible to determine the exact height of the fluid due to the limited transparency of the bearing and therefore the

assumption was made that the pressure tube was empty (and thus the lubricant weight in that pressure tube was assumed to be zero) when the fluid was below the measurement threshold. Therefore, the calculated weight, and thus vertical force, will be a slight under-approximation, as fluid could be present in the tubes but not yet protrude above the measurement threshold.

The frictional moment is calculated using the difference between the vertical force measurements, using equation Equation 2.4, where M is the frictional moment, a is the distance from the left of the bearing to the center of the bearing hole, F_Y is the vertical force, L_b is the length of the bearing, c is the distance of the micrometer screw above the bottom of the bearing, $d_{tube,i}$ is the horizontal distance of pressure tube i measured from the left side of the bearing and $d_{internal,i}$ is the horizontal distance of the center of gravity of internal tube i measured from the left side of the bearing (see also Figure 2.10).

$$M_f = a \cdot F_y + L_b \cdot F_r - c \cdot F_h - \sum_{i=0}^{10} w_{tube,i} d_{tube,i} - \sum_{i=0}^{10} w_{internal,i} d_{internal,i} \tag{2.4}$$

Similarly as for the vertical force, the moment due to $w_{internal,i}$ is only included if for the same tube $w_{tube,i}$ is greater than zero, as this means that the fluid column protruded above the bearing (measurement threshold) and thus the entire internal tube was filled with lubricant. The distance c will be close to zero in the experimental setup (as explained in subsection 2.4.3); however, it is included in the equation to account for a small misalignment that could affect the measured frictional moment. The friction force F_f can then be simply calculated by dividing the frictional moment by the radius of the bearing. The summation takes into account the weight of the lubricant in the pressure tubes (as explained before, this should be taken into account as this is measured by the force sensors but is not part of the hydrodynamic forces generated). However, because the fluid does not rise above the measurement threshold in the first few pressure tubes on the left (depending on the operating conditions), a portion of the moment induced by the fluid weight is neglected. As this is mainly on the left side of the shaft, this assumption will cause the measured frictional moment to be slightly smaller than it actually is.

Finally, it is important to note that where normally the load capacity of a journal bearing is defined as the vertical force, in this thesis the load capacity is defined as the magnitude of the force vector F_{mag} as given in Equation 2.5. The reason for this is that the eccentricity of the bearing is prescribed, where normally the bearing is free to move to a position where the horizontal force component is equal to zero and the vertical force component is the load capacity. To not neglect the horizontal force component, it is more logical to set the load capacity equal to the magnitude of the force vector.

$$F_{mag} = \sqrt{F_X^2 + F_Y^2} \tag{2.5}$$

The friction coefficient can be calculated using Equation 2.6.

$$\mu = \frac{M_f / R_B}{F_{mag}} = \frac{F_f}{F_{mag}} \tag{2.6}$$

Due to the leaf springs and weight of the setup, the force sensors will measure a force without operation of the bearing. This force will vary based on the eccentricity and magnetic field strength (as the electromagnet pulls the bearing towards the shaft). To correct for this force, calibration measurements are performed and the difference between the normal measurements and the calibration measurements is used to determine the forces and moment generated by the hydrodynamic bearing.

2.6. Fluid properties

For the test measurements of the setup AVIA Fluid RSL 32 was used, which is a hydraulic mineral oil. The MR fluid used for the measurements is a diluted variant of MRHCCS4-A made by Liquids Research Ltd, of which the mass fraction of carbonyl iron particles is reduced from 70% to 20%. Furthermore, the ratio of additives was altered and $\sim 10\mu m$ Boron Nitride particles (with the goal of reducing bearing wear due to iron particles) were added. The fluid properties are summarized in Table 2.5. The hydraulic oil has a much lower viscosity compared to the MR fluid in the absence of a magnetic field and therefore the performance of both lubricants should not be directly compared. The tests and simulations with hydraulic oil are mainly intended to investigate the performance of the test setup and to understand the potential differences between the experiments and the model.

	Property	Value
MR fluid	Carrier oil	Hydrocarbon
	Particles	Carbonyl iron
	Particle size	1-2 μm
	Mass fraction	20%
	Volume fraction	~ 2%
	Density	1218 $[kg/m^3]$
	Dynamic viscosity	Figure 2.11
	Anti-wear particles	Boron Nitride
	Anti-wear particle size	$10\mu m$
Hydraulic oil	Density	852 $[kg/m^3]$
	Dynamic viscosity	Figure 2.11

Table 2.5: MR fluid properties.

To determine the dynamic viscosity of both fluids for different temperatures, shear rates and (for the MR fluid) magnetic field strengths, the fluids were tested on the Anton Paar MCR 302 rheometer. Figure 2.11a plots the viscosity versus the shear rate and clearly shows the strong shear-thinning behavior of the MR fluid. The viscosity of the hydraulic oil decreases very slightly with increasing shear rate, indicating its very weakly shear-thinning. The shear rates encountered during testing with the hydraulic oil, were in the range of 10-2500s^{-1} (as found using the numerical model) over which the viscosity was pretty much constant (variation of only ± 0.3% with respect to the average viscosity over this shear rate range). Therefore, in the theoretical model the average viscosity over the encountered shear rate was used.

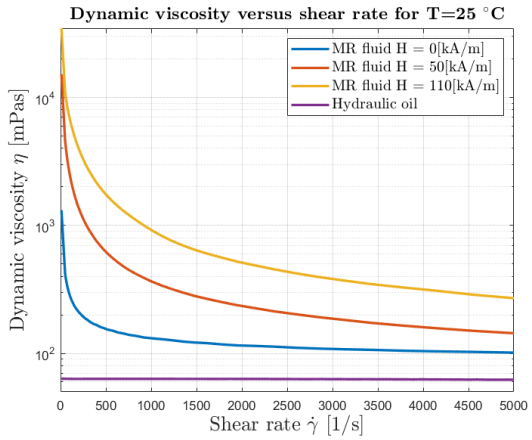

(a) Dynamic viscosity versus shear rate for hydraulic oil and MR fluid for different magnetic field strengths.

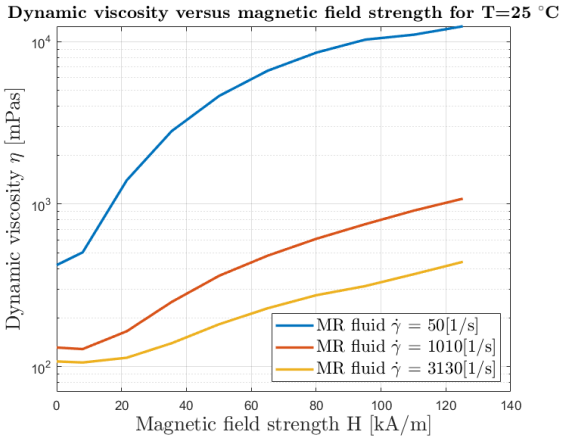

(b) Dynamic viscosity versus magnetic field strength for MR fluid for different shear rates.

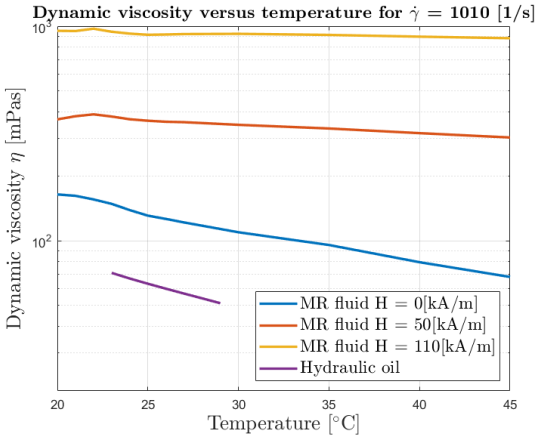

(c) Dynamic viscosity versus temperature for hydraulic oil and MR fluid for different magnetic field strengths.

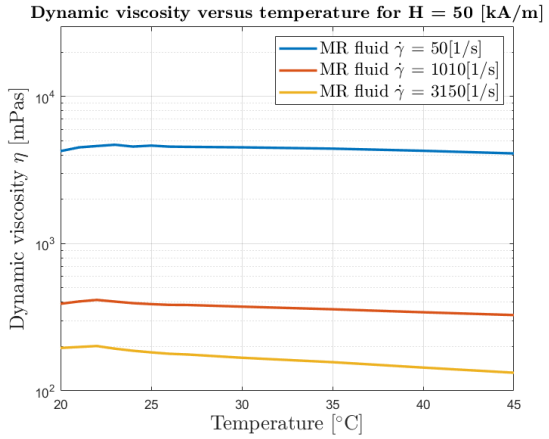

(d) Dynamic viscosity versus temperature for MR fluid for different shear rates.

Figure 2.11: Viscosity of the MR fluid and hydraulic oil.

Figure 2.11b plots the dynamic viscosity versus the applied magnetic field strength for different shear rates. The viscosity increases strongly for increasing magnetic field strength, where it must be noted that the magnetorheological effect is significantly stronger for low shear rates. This is probably due to the fact that the particles chains can be formed easier and are less quickly broken due to the low sliding velocity. For a shear rate of $50s^{-1}$ the viscosity increases almost by a factor 30 with an applied magnetic field of 125kA/m while for a shear rate of $1010s^{-1}$ this is decreased to a factor 8 and for a shear rate of $3130s^{-1}$ the increase is only a factor 3.5. This is an important characteristic as the encountered shear rates in the performed experiments are in the range 10-2500s^{-1} (as found using the numerical model). Moreover, it can be noted that for a very small magnetic field strength, the viscosity barely increases which is probably due to the fact that the magnetic field is not strong enough for particle chains to fully form. For large magnetic field strength it can be noted the curves flatten as the amount of formed particle chains reaches its limit due to magnetic saturation of the particles.

The effect of temperature on viscosity can be seen in Figure 2.11c. For both the hydraulic oil and the MR fluid, the viscosity decreases with increasing temperature. This effect is strongest for the hydraulic oil, while for the MR fluid the effect decreases for increasing magnetic field strength. This is the case because for high magnetic field strengths, the particle chains have the dominant effect over the carrier oil on the viscosity [13]. Note that the hydraulic oil was tested for a different temperature range, as both fluids were tested only for the temperatures encountered during testing.

Finally, since the MR fluid is strongly shear-thinning, the effect of temperature might also be different

at different shear rates. The dynamic viscosity as a function of temperature for different shear rates is shown in Figure 2.11d. The hydraulic oil is not plotted in this graph as the viscosity was found to be almost constant for different shear rates, so the temperature effect was also equal for different shear rates. It can be seen that for higher shear rates, the effect of temperature (the decrease in dynamic viscosity due to an increase in temperature) is slightly larger. A potential reason for the slightly stronger temperature dependence at high shear rates is that at higher shear rates the influence of the carrier oil might become more dominant relative to the influence of the particle chains on the viscosity.

2.7. Experimental procedures

In this section, the experimental procedures are introduced. Experiments are performed with both hydraulic oil and MR fluid as lubricant, which differ slightly and are therefore discussed separately in subsection 2.7.1 and subsection 2.7.2 respectively. The measurements using hydraulic oil and MR fluid were performed without disassembling the bearing setup. This ensures that the uncertainties in vertical and horizontal eccentricity are limited. Due to the finite stiffness of the compliant joint, there is a difference between the prescribed displacement by the micrometer screw and the actual displacement of the bearing. The effect of this on the eccentricity ratios tested for, is described in subsection 2.7.3.

2.7.1. Experimental procedure for hydraulic mineral oil tests

All tests were performed at a constant rotational speed of 50rpm. For measurements with hydraulic oil as lubricant, the eccentricity ratio was varied from 0.6 to 0.92 in steps of 0.04 (or equivalently, a fluid gap of 0.5mm to 0.1mm in steps of 0.05mm). First, calibration measurements were performed while the shaft was stationary. The bearing was moved to an eccentricity ratio of 0.6 and then moved in steps of 0.04 (steps of 0.05mm) until an eccentricity ratio of 0.92 was reached. For each eccentricity ratio, the average force measured by each sensor was calculated over a measurement period of 30 seconds to average out noise. Next, the oil pan was filled with the lubricant and the actual test was performed. Again, the bearing was moved from an eccentricity ratio of 0.6 to 0.92. Before each measurement, the shaft was spun for 5 minutes at 50rpm, to give the lubricant the time to rise in the pressure tubes and reach equilibrium. After 5 minutes, the measurement was performed for a period of 30 seconds over which the average was taken. This was done to average out the noise and the force oscillations caused by the oscillating eccentricity ratio (due to misalignment of the shaft and the bearing and the eccentricity of the shaft in the ball bearings; see also subsection 4.1.2). Furthermore, the height of the fluid columns in the pressure tubes was measured by hand using a steel ruler. Finally, the temperature of the lubricant in the oil pan was measured using a type K thermocouple, with an accuracy of $\pm 1^{\circ}$C. After the measurement was performed, the eccentricity ratio was increased by turning the micrometer screw (while keeping the motor turned on) and the same procedure was followed. This procedure was repeated until the largest eccentricity ratio was reached, after which the motor was turned off. After a test was performed, the setup was moved back to an eccentricity ratio of 0.6 so that the oil could flow back out of the pressure tubes into the oil pan, before repeating the test. The test was repeated five times to verify repeatability and have multiple data points. During the tests, the load cell data was captured every 50ms (or equivalently at 20Hz).

2.7.2. Experimental procedure for MR fluid tests

Several changes to the experimental procedure for the tests with hydraulic mineral oil had to be made to test with MR fluid. This is due to two factors:

1. The tests with MR fluid had to be performed for several magnetic field strengths (different values of applied current).
2. The viscosity of the MR fluid is very high and the MR fluid is gray and opaque. This had two implications. First of all, because of the high viscosity, it took a long period of time before the fluid reached equilibrium in the pressure tubes. Second, it was impossible to see a decrease in pressure as a layer of the opaque fluid would stick to the inside of the pressure tube even if the fluid column lowered.

All tests were again performed at 50rpm. For the measurements with MR fluid the eccentricity ratio was again varied from 0.6 to 0.92, however, in steps of 0.08 (or equivalently in steps of 0.1mm). This was done because the experiments were quite time consuming as it took a long period of time for the

lubricant to reach equilibrium in the pressure tubes due to the high viscosity. Equilibrium was assumed if after a time period of ten minutes the height of the fluid columns increased by less than 1mm. This took anywhere between 1 and 2 hours, depending on the temperature and eccentricity ratio. After increasing the magnetic field strength the same criterion of equilibrium was used and the time period needed was in the range of 30 to 50 minutes (the increase in column height was smaller than for a new eccentricity ratio, so less time was needed). The current through the coil was increased from 0A to 1.2A in steps of 0.4A.

Due to the second issue, the tubes had to be cleaned after an experiment was performed at a specific eccentricity. For this reason, the tests were performed in a slightly different order. MR fluid tests were performed per eccentricity. First (when the motor was turned off), a 30-second calibration measurement was made at the set eccentricity. Then the current through the coil was increased and for each current setpoint a calibration measurement of 30 seconds was performed. Afterwards, the current was set equal to zero again and the motor was turned on. When equilibrium was reached (as described above), a 30-second measurement was performed, the height of the fluid columns in the pressure tubes was measured and the temperature of the lubricant in the oil pan was measured. Additionally, the temperature of the fluid near the yoke (at the side of the bearing as the thermocouple was too large to place inside the fluid film between the shaft and the bearing) and the temperature of the yoke itself were measured, as the electromagnet introduces extra heat into the system. After the measurements were performed for all current setpoints, the electromagnet and motor were switched off. Afterwards, the straight (external) pressure tubes were removed and cleaned by pushing a piece of paper through the tubes. Then the procedure including calibration was repeated for the next eccentricity ratio. This procedure was repeated three times for every eccentricity ratio. The load cell data was captured every 10ms (or equivalently at 100Hz) to have a bit more data points (compared to the experiments with hydraulic oil), especially to analyze the time-dependent fluctuations in the measured forces.

2.7.3. Eccentricity

The prescribed eccentricity ratio in the horizontal direction $\epsilon_{X,p}$ was varied between 0.6 and 0.92, with incremental steps of 0.04. However, because of the finite stiffness of the compliant joint, the actual eccentricity ratio of the bearing is smaller. The actual displacement $x_{bearing}$ of the bearing based on the displacement set by the micrometer screw $x_{micrometer}$, the measured horizontal force F_h and the determined stiffness of the compliant joint $K_{compliant}$ can be calculated using Equation 2.7 (see Appendix B for a detailed explanation).

$$x_{bearing} = x_{micrometer} - \frac{F_h}{K_{compliant}} \tag{2.7}$$

This results in slightly different eccentricity ratios measured for (the actual eccentricity ratios $\epsilon_{X,a}$), which are given in Table 2.6. For the MR fluid test, only half of the eccentricity ratios (steps of 0.08 between eccentricity ratios) were tested for due to the length of the tests. This means that MR fluid tests were performed for $\epsilon_{X,a} = 0.63, 0.70, 0.78, 0.86, 0.94$. Throughout this thesis, the actual eccentricity will be referred to as ϵ_X. The vertical eccentricity was set as close to zero as possible using gauge blocks which resulted in $\epsilon_Y = -0.06$ (due to a small mistake in setting the correct height, it was not exactly equal to zero). These values for ϵ_X and ϵ_Y were used as input for the numerical model. Furthermore, since ϵ_Y = -0.06, the horizontal force will not be perfectly aligned with the bottom of the bearing, resulting in c = -0.075mm (see Figure 2.10 for the definition of c).

Prescribed eccentricity ratio $\epsilon_{X,p}$	Actual eccentricity $\epsilon_{X,a}$
0.6	0.63
0.64	0.67
0.68	0.70
0.72	0.74
0.76	0.78
0.80	0.82
0.84	0.86
0.88	0.90
0.92	0.94

Table 2.6: Prescribed versus actual eccentricity ratio.

2.8. Limitations

Several limitations in the setup are identified which are discussed below.

1. **Temperature control** As the lubricant is contained in the open oil pan and no temperature control measures are included in the setup, the temperature will be mainly influenced by the environmental temperature. Due to the relatively large film thickness and low operating speed, not much heat will be generated as a result of the operation of the test setup. When current is applied to the coil, the electromagnet will heat up quite quickly. This also increases the temperature of the lubricant flowing through the bearing. The increase in temperature cannot be controlled in the current setup, but to ensure that it can be taken into account, the temperature of the lubricant will be measured during testing. The temperature of the lubricant is important as it directly affects the viscosity (as explained in section 2.6).
2. **Force magnitude** The magnitude of the generated load capacity is limited due to the stiffness of the leaf springs and the height of the pressure tubes. As the minimal film thickness is on the right side of the bearing and the shaft rotates clockwise, the buildup pressure will push the bearing towards the right (away from the micrometer screw). This means that the horizontal force generated by the bearing cannot exceed the horizontal force due to the leaf springs that keep the bearing pressed against the micrometer screw. Stiffer leaf springs could be used to increase this force; however, this would also introduce a larger horizontal reaction force which is transferred to the load cells measuring the vertical force. This is not desired, as this could potentially damage the load cells and might affect the accuracy of the vertical force measurements. Some tests were performed to check the performance of the vertical load cells when loaded horizontally. These can be found in Appendix B, where the performance of the compliant joint and the effect of horizontal loading on the vertical load cells are investigated simultaneously. Furthermore, the pressure generated is limited by the length of the pressure tubes; however, as the design allows for the tubes to be swapped out, longer tubes can be fitted if necessary.
3. **Minimal film thickness** As the eccentricity of the bearing is prescribed in the setup using a micrometer screw, the best accuracy reached in the eccentricity is around ± 0.01mm. However, every slight misalignment or eccentricity of the shaft with respect to the ball bearings it rotates in causes an inconsistent eccentricity (with respect to the hydrodynamic bearing) over a shaft revolution. Due to this inconsistent eccentricity over a shaft revolution, it is basically impossible to reach very large eccentricity ratios, as over a revolution the shaft and bearing will then touch.
4. **Uncertainties in eccentricity** The vertical location of the bearing is set by attaching it to the leaf springs. The leaf springs have slotted holes to allow for some freedom in aligning the bearing. However, this makes it very difficult to mount the bearing with high accuracy relative to the shaft. To reduce this uncertainty, the bearing was placed on top of gauge blocks to accurately define the height. This ensures that the height is accurately known and kept constant while the leaf springs can be attached. The horizontal eccentricity is also hard to determine accurately due to misalignment of the shaft and bearing and the eccentricity of the shaft with respect to the ball bearings it is mounted in. The horizontal eccentricity is determined using $\epsilon_X = 1$ as a reference point, which is the case when the micrometer screw does not touch the bearing (because then the bearing is

pushed against the shaft due to the leaf springs). This was done without any lubricant present in the system. By turning the micrometer screw until the horizontal load cell measured a force, it was determined when the micrometer screw started moving the bearing and thus started decreasing ϵ_X (the micrometer screw pushes the bearing away from the shaft and thus decreases the eccentricity ratio). Furthermore, the maximum eccentricity ratio was determined for which the horizontal force was constant throughout a full shaft rotation, indicating that the bearing and shaft do not touch anymore. The difference between these is a measure of the uncertainty in horizontal eccentricity over a shaft rotation, which was equal to $\sim$0.08mm. The final uncertainty in the horizontal eccentricity is the deformation of the compliant joint. The deformation was approximated based on the measured stiffness of the leaf springs and the reduction in horizontal force for a given prescribed displacement with the compliant joint installed (see Appendix B). As explained in subsection 2.7.3 the eccentricity is compensated for the stiffness of the compliant joint; however, this off course still introduces a small uncertainty due to the approximated compliant joint stiffness.

3
Theoretical model

The numerical model was constructed using COMSOL MULTIPHYSICS 6.1. The model consists of two different physics which can be simulated independently; a magnetic field model and a fluid flow model. The magnetic field model is a three-dimensional simulation of the electromagnet and bearing setup and is used to calculate the magnetic field strength within the fluid film. The results of this simulation were used as input for the two-dimensional fluid flow model, where the Reynolds equation is used to solve for the pressure within the fluid film. This chapter will discuss the theory behind the fluid flow and magnetic field model separately in section 3.1 and section 3.2 respectively. Note that some definitions as defined in section 2.3 will be used again. Verification of the models introduced in this chapter can be found in Appendix E.

3.1. Fluid flow model

The fluid flow can be modeled separately from the magnetic field. First, the implementation of the Reynolds equation and the cavitation algorithm is discussed in subsection 3.1.1. The magnetic field model, as introduced in section 3.2, is used to calculate the magnetic field strength at the bearing surface, which is used as input for the viscosity of the MR fluid as described in subsection 3.1.2. The definition of the film thickness profile is explained in subsection 3.1.3. In subsection 3.1.4 the implementation of the actual bearing shape (since the bearing shape of the actual bearing was not perfectly circular) is elaborated on. Then, the equations used to calculate the forces generated in the bearing using the pressure distribution found by solving the Reynolds equation are presented in subsection 3.1.5. Finally, the COMSOL implementation of the model is discussed in subsection 3.1.6

3.1.1. Reynolds equation

Fluid flow is normally described using the Navier-Stokes equations in combination with a continuity equation (to include mass conservation). Generally, simplifications are made to make the equations easier and quicker to solve. For the application of the Navier-Stokes equations in hydrodynamic bearings, many simplifying assumptions can be made resulting in the much simpler Reynolds equations. A full list of the simplifying assumptions needed for the Reynolds equation is given in Appendix C, but the most important simplification is that inertial forces are neglected. The two-dimensional Reynolds equation is given in Equation I.9 [1], where h is the film thickness, ρ the fluid density, η the viscosity, p the pressure and U_1, U_2, V_1 and V_2 the velocity of the boundaries in the x- and y-directions at the shaft and bearing surface respectively (where x is in the circumferential direction, y is in the axial direction, subscript 1 refers to the shaft and 2 to the bearing).

$$\frac{\partial}{\partial x}\left(\frac{\rho h^3}{12\eta}\frac{\partial p}{\partial x}\right)+\frac{\partial}{\partial y}\left(\frac{\rho h^3}{12\eta}\frac{\partial p}{\partial y}\right)=\frac{U_1+U_2}{2}\frac{\partial \rho h}{\partial x}+\frac{V_1+V_2}{2}\frac{\partial \rho h}{\partial y}+\frac{\rho h}{2}\frac{\partial}{\partial x}(U_1+U_2)+\frac{\rho h}{2}\frac{\partial}{\partial y}(V_1+V_2)+\frac{\partial \rho h}{\partial t} \tag{3.1}$$

Equation 3.1 can be further simplified because in a hydrodynamic bearing there is no vertical surface velocity (for steady and stationary operation) and no surface velocity in y-direction. This means $\delta h/\delta t$, V_1 and V_2 can all be set equal to zero. Furthermore, the fluid is assumed to be incompressible, meaning the density can be cancelled out of the equation, resulting in Equation 3.2 (where $U = U_1 + U_2$).

$$\frac{\partial}{\partial x}\left(-\frac{h^3}{12\eta}\frac{\partial p}{\partial x}+\frac{Uh}{2}\right)+\frac{\partial}{\partial y}\left(-\frac{h^3}{12\eta}\frac{\partial p}{\partial y}\right)=0 \tag{3.2}$$

An important phenomenon to take into account when modeling hydrodynamic bearings is cavitation. In the diverging region of a hydrodynamic bearing the pressure will become below the cavitation pressure, causing gas bubbles to form in the fluid film which consequently change the pressure distribution. To accurately account for this effect, a cavitation model should be implemented. In this thesis, the cavitation algorithm of Alakhramsing et al. [14] is implemented, which is based on the JFO boundary conditions. The modified Reynolds equation that is solved with this algorithm implemented is given in Equation 3.3. In their algorithm, both the mass fraction f and the pressure p are replaced by functions of a newly introduced variable ξ. These transformation functions for pressure and mass fraction are given in Equation 3.4a and Equation 3.4b respectively.

$$\frac{\partial}{\partial x}\left(\frac{-h^3}{12\eta}\frac{\partial \xi}{\partial x}+\frac{hf}{2}\right)+\frac{\partial}{\partial y}\left(\frac{-h^3}{12\eta}\left((\xi \geq 0)+(\xi<0)k_{AD,y}\right)\frac{\partial \xi}{\partial y}\right)=0 \tag{3.3}$$

$$p=(\xi \geq 0)\xi \tag{3.4a}$$

$$f=1+(\xi<0)c_f\xi \tag{3.4b}$$

The modified Reynolds equation can then be solved for ξ and the pressure and mass fraction can consequently be calculated using the transformation functions. The cavitation pressure is assumed to be equal to the ambient pressure (equal to zero for the proposed model), which is a good assumption since the lubricant is often exposed to ambient pressure for long periods of time. When $\xi \geq 0$, it equals the pressure and the mass fraction is equal to 1. When $\xi < 0$, cavitation is present and the pressure is equal to zero while the mass fraction can be determined using Equation 3.4b. c_f is a transformation constant that is needed to numerically stabilize the convection-dominated Reynolds equation (within the cavitated region) by introducing some artificial diffusion. The amount of artificial diffusion can be chosen freely; however, should not be so large causing too much damping while being large enough to suppress oscillations in the solution [14]. When using $c_f = \frac{h^2}{3\eta h_e}$ for linear elements (or $c_f = \frac{2h^2}{3\eta h_e}$ for quadratic elements), where h_e is the local mesh element size, the modified Reynolds equation including artificial diffusion can be written as in Equation 3.3. Furthermore, the equation is numerically stabilized in y-direction as well, by adding artificial diffusion in the crosswind direction by means of $k_{AD,y}$. $k_{AD,y}$ is chosen similar to the artificial diffusion in x-direction, but is scaled relative to the angle between the gradient of the flow solution and flow direction and is defined as in Equation 3.5 with $\delta = 1e-10$. For a complete derivation of Equation 3.3 including a more elaborate explanation of the chosen transformation constant c_f, k_{AD} and $k_{AD,y}$, the reader is referred to [14].

$$k_{AD,y} = k^*_{AD,y}k_{AD} \tag{3.5a}$$

$$k^*_{AD,y} = \left(\frac{\left|\frac{\partial \xi}{\partial x}\right|\left|\frac{\partial \xi}{\partial y}\right|}{\left(\frac{\partial \xi}{\partial x}\right)^2+\left(\frac{\partial \xi}{\partial y}\right)^2+\delta}\right) \tag{3.5b}$$

3.1.2. Magnetorheological fluid model

MR fluids have a yield stress under the influence of a magnetic field (below which they behave like a solid) and are (strongly) shear-thinning, meaning the viscosity strongly depends on the shear rate. In literature, many viscoplastic rheological models exist to capture this behaviour of MR fluids, such as the Bingham plastic model and the Herschel-Bulkley model (see also Appendix D). The shear rate changes over the thickness of the film, which means that the viscosity of the MR fluid is not constant throughout the film. In order to take into account variations in fluid properties across the film thickness, Dowson [15] derived the generalized Reynolds equation. As implementation of the generalized Reynolds equation in combination with a viscoplastic rheological model and a proper cavitation model can be complex and creating an 'ideal' model was not the main focus of this thesis, it was decided to stick to the non-generalized Reynolds equation. To capture the strongly varying shear rate in the bearing, the shear rate in the middle of the fluid film was calculated, which is just the shear rate due to Couette flow (in the

middle of the fluid film the shear rate due to Poiseuille flow is equal to zero). The viscosity of the MR fluid was then determined by performing a two-dimensional interpolation of the viscosity for the local shear rate and the magnetic field strength normal to the fluid film. This is a strong simplification as the shear rate also largely varies in radial direction which is now neglected; however, it does allow us to stick to the non-generalized Reynolds equation. Furthermore, the measured viscosity as a function of shear rate and magnetic field strength can be implemented directly by means of interpolation without having to fit a viscoplastic model to the viscosity data.

3.1.3. Film thickness profile

To solve the Reynolds equation as given in Equation 3.3, the film height must be defined around the bearing surface. Using an eccentricity ratio in X- and Y-direction (as defined in Figure 2.5), the film thickness can be defined as in Equation 3.6.

$$h = \Delta R(1 + \epsilon_X \cos(\Phi) - \epsilon_Y \sin(\Phi)) \tag{3.6}$$

As the experimental test setup contains multiple pressure tubes with relatively large inlet holes, this should be incorporated into the model. Over the area of the inlets, a constant (but unknown) pressure is expected. This is implemented by setting the film height at the tube inlet locations a factor 100 (arbitrary but large) higher than the radial clearance. This ensures that the pressure over the inlets is constant. Another implementation was to set the pressure gradient at the inlets equal to zero; however, this method is computationally more demanding as extra constraints are introduced and the simulation convergence is less good.

3.1.4. Bearing shape implementation

As the bearing was 3D-printed, tolerances of the bearing were not ideal. The tolerance of the circular section of the bearing is critical as a difference of $\pm$0.1mm has a significant effect on bearing performance. As the bearing tolerance could not easily be improved with the current production method, two 2D measurements of the bearing were made at DEMO (Dienst Elektronische en Mechanische Ontwikkeling) to determine the actual shape of the bearing. A measurement determining the radius and roundness found a deviation from the intended radius of $\sim 0.05 - 0.15$mm and a deviation on the roundness of ~ 0.1mm. This indicated a significant deviation on the bearing shape. To capture the actual bearing shape in the model, a full 2D measurement was performed where a point cloud was stored of the actual bearing shape. This measurement was taken on both sides of the bearing (front and back) and was used to determine the radius of the bearing as a function of the circumferential position. To simplify the COMSOL implementation, the average radius of the two measurements was used as input for the model. Figure 3.1 shows the determined radius at the front and back of the bearing, the average radius and the intended radius of 26.25mm.

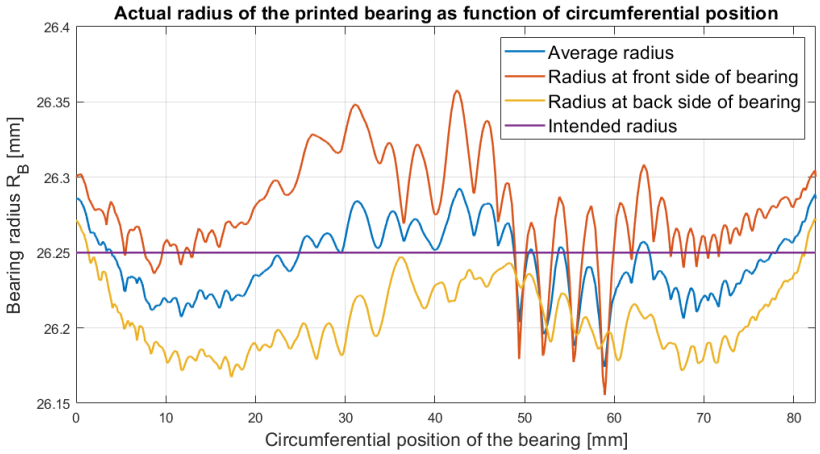

Figure 3.1: Radius of the printed bearing as function of circumferential position.

Several interesting conclusions can be drawn from the measured radius. The radius of the bearing oscillates around the intended radius and has a maximum error of ± 0.1mm. Furthermore, the radius at the front is about 0.05-0.1mm larger than the radius at the back of the bearing. This can be due to how the bearing is printed or due to some warping during curing of the bearing. The oscillation of the radius at front and back of the bearing does seem to have a similar shape. Many smaller oscillations can be seen, which are probably due to the discretization of the printer and printer settings. Finally, the larger oscillations at the front side of the bearing around the circumferential position of 50-60mm can be caused by the fact that a small crack was formed during production, which was repaired by filling it with some glue.

The non-constant bearing radius meant that Equation 3.6 had to be slightly modified as ΔR is not a constant value but varies with circumferential position. The equation implemented for the height of the film is given in Equation 3.7, where $R_{B,actual}$ is the average radius as shown in Figure 3.1 and thus varies with the circumferential position in the bearing and R_S is the radius of the shaft.

$$h = (R_{B,actual} - R_S)(1 + \epsilon_X \cos(\Phi) - \epsilon_Y \sin(\Phi)) \tag{3.7}$$

3.1.5. Derived values

Using the pressure distribution found by solving Equation 3.3 and using Equation 3.4a, the generated forces were calculated. The horizontal and vertical forces were calculated by integrating the pressure over the bearing domain using Equation 3.8 and Equation 3.9 respectively, where Φ is the circumferential position as defined in Figure 2.5.

$$F_{X,pressure} = \iint_S -p \cos\Phi dA \tag{3.8}$$

$$F_{Y,pressure} = \iint_S p \sin\Phi dA \tag{3.9}$$

In addition to the forces due to the fluid pressure, forces are generated due to the shear stress exerted on the bearing and shaft. The shear stress can be calculated using Equation 3.10 [1]. By plugging in z=0 or z=h, the shear stress can be calculated at the shaft surface and bearing surface respectively.

$$\tau_{z,x} = \frac{1}{2}\frac{\partial p}{\partial x}(2z - h) + \eta\frac{U_2 - U_1}{h} \tag{3.10}$$

The shear stress causes a resultant (frictional) moment and a horizontal and vertical force defined at the center of the bearing. Normally in hydrodynamic bearings, the friction force is a factor 100-1000 smaller than the load capacity [1]. Therefore, the effect of the shear stress on the load capacity can be neglected. However, in the experimental setup in this thesis the rotational velocity is low and the radial gap is relatively large (1.25mm). Therefore, the effect of the shear stress on the load capacity cannot be neglected. The horizontal and vertical force components exerted on the bearing due to the shear stress are calculated using Equation 3.11 and Equation 3.12 respectively.

$$F_{X,shear} = \iint_S -\tau_{zx} \sin(\Phi)\Big|_{z=0} dA \tag{3.11}$$

$$F_{Y,shear} = \iint_S -\tau_{zx} \cos(\Phi)\Big|_{z=0} dA \tag{3.12}$$

The magnitude of these was found to be in the range of 2 to 13% of the pressure-induced force components for oil and in the range of 1 to 20% for MR fluid (depending on eccentricity ratio and current through the coil, where for a small eccentricity ratio and a large current, the shear induced forces are more significant). Calculating these at the shaft and bearing surface should not matter; however, the

calculated forces were found to differ. Simply implementing a geometry term did not solve the differences and more research is needed to determine how to correctly implement the equations at both surfaces, as there is no existing literature on this topic (as the effect of the shear stress on the load-carrying forces is normally neglected). As it is assumed that the differences are due to a geometric effect and in the model the shaft surface is assumed to be 'flat' (the geometric change in film thickness is attributed to the bearing surface), the load-carrying forces due to the shear stress are calculated at the shaft surface. These are added to the load capacity as calculated in Equation 3.8 and Equation 3.9 resulting in the total force in X- and Y-direction as given in Equation 3.13 and Equation 3.14 (the shear-induced forces are subtracted from the pressure-induced forces as they are calculated at the shaft surface and the direction at the bearing is thus opposite). The magnitude of the force vector is determined using Equation 3.15 (this is also referred to as the load capacity throughout this thesis, as explained in section 2.5).

$$F_X = F_{X,pressure} - F_{X,shear} \tag{3.13}$$

$$F_Y = F_{Y,pressure} - F_{Y,shear} \tag{3.14}$$

$$F_{mag} = \sqrt{F_X^2 + F_Y^2} \tag{3.15}$$

The frictional moment exerted on the bearing can be calculated at either the shaft surface or at the bearing surface. In the model, the shaft surface is assumed to be flat, while the bearing surface is defined with respect to this flat surface (to define the geometry of the bearing). For this reason, a geometric friction component should be included when integrating the shear force at the bearing surface.

The frictional moment (defined around the center of the bearing) can then be calculated at the shaft and bearing surface using Equation 3.16 and Equation 3.17 respectively [16].

$$M_{f,shaft} = \iint_S R_B \tau_{zx} \Big|_{z=0} dA \tag{3.16}$$

$$M_{f,bearing} = \iint_S R_B (-\tau_{zx} - p\frac{\partial h}{\partial x}) \Big|_{z=h} dA \tag{3.17}$$

Note that the integration is performed only over the domain excluding the tube inlets, as at these locations the pressure cannot exert a shear force on the bearing but on the fluid only. The frictional moment at the bearing and shaft surface is equal in magnitude but opposite in direction.

The friction force is simply defined as the the frictional moment divided by the bearing radius as in Equation 3.18. This is a fictitious force that is defined to analyze the magnitude of the friction compared to the load capacity of the bearing. Therefore, only the magnitude of this force is of interest, so it does not matter whether it is calculated using the frictional moment at the bearing or shaft.

$$F_f = \frac{M_{f,shaft/bearing}}{R_B} \tag{3.18}$$

Another method of determining the friction force is using the concept of friction loss. By calculating the friction loss using Equation 3.19 and dividing it by the sliding velocity, the (magnitude of the) friction force can also be determined [16]. This method can be used to verify the correct implementation of geometric friction calculation in the model.

$$\Phi_{loss} = \int_a^b \left(\eta \left(\frac{\partial u}{\partial z} \right)^2 + \eta \left(\frac{\partial v}{\partial z} \right)^2 \right) dz = \frac{h^3}{12\eta} \left(\frac{\partial p}{\partial x} + \frac{\partial p}{\partial y} \right)^2 + \frac{\eta}{h} (U_2 - U_1)^2 \tag{3.19}$$

Finally, the friction coefficient μ can be calculated by dividing the friction force by the load capacity as in Equation 3.20.

$$\mu = \frac{F_f}{F_{mag}} \tag{3.20}$$

3.1.6. COMSOL implementation

The Reynolds equation as given in Equation 3.3 is implemented by means of a General Form PDE in COMSOL Multiphysics 6.1. Quadratic-order Lagrangian shape functions were used for discretization. Convergence was assumed when the relative tolerance was less than 1 x 10^{-3}. Due to symmetry, only half of the bearing needs to be simulated and the computational domain is given in Figure 3.2. On the symmetry boundary, a zero flux boundary condition was set while on the other boundaries a Dirichlet boundary condition with p = 0Pa (atmospheric pressure was set equal to zero, such that the calculated pressure is relative to the atmospheric pressure) was imposed. Furthermore, the film thickness is determined using Equation 3.7 for most of the domain except for within the circular pressure tube inlets, where the film height is set equal to 125mm (factor 100 larger than the radial clearance ΔR) as explained in subsection 3.1.3. The temperature is assumed to be constant throughout the bearing. Finally, the viscosity of the MR fluid is interpolated in two dimensions based on the shear rate due to the Couette flow only (in the middle of the fluid gap) and the magnetic field strength found using the magnetic field model. For the simulations of the reference oil, the viscosity was assumed to be constant throughout the domain.

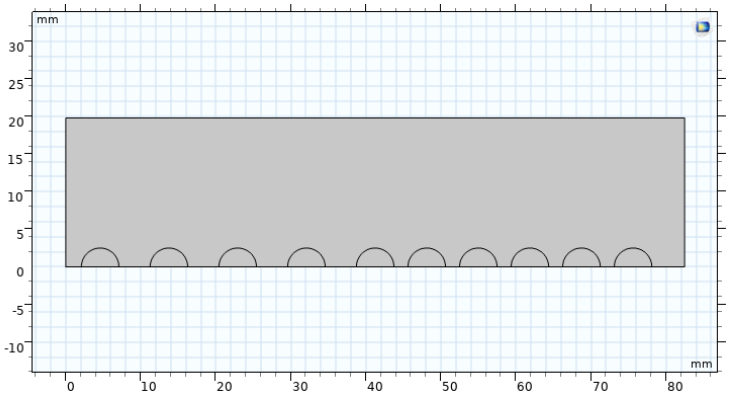

Figure 3.2: Computational domain of the fluid flow simulation.

A mesh convergence study was performed to determine the mesh refinement needed for accurate results. The magnitude of the force vector (F_{mag}) is plotted against the number of degrees of freedom (DoF) solved for in Figure 3.3a (the number of DoF increases with the amount of mesh elements). Similarly, the friction force (F_f) is plotted against the number of DoF solved for in Figure 3.3b. As can be clearly seen, both variables converge for approximately 8000 DoF solved for. The convergence of these variables was analyzed, as these are directly compared to the experimental results. Based on the mesh convergence study, an ”extra fine” free triangular mesh was generated in COMSOL, resulting in 9211 DoF solved for or 4012 mesh elements. The final mesh is shown in Figure 3.4.

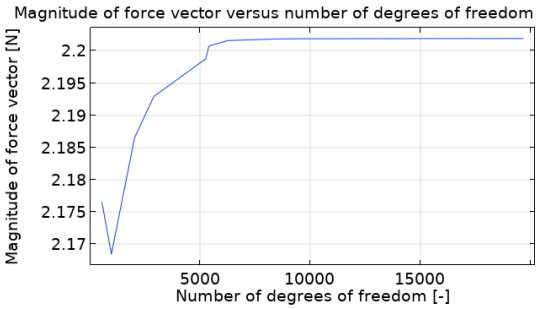

(a) Convergence of force magnitude F_{mag}.

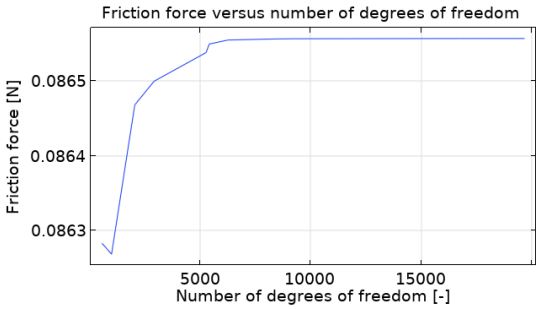

(b) Convergence of friction force F_f.

Figure 3.3: Convergence of F_{mag} and F_f, plotted versus number of DoF solved for.

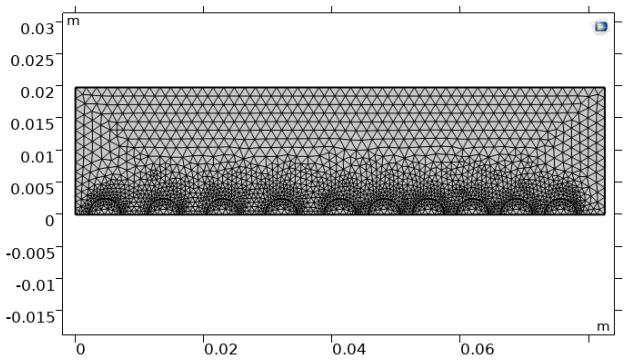

Figure 3.4: Mesh used in the fluid flow model.

3.2. Magnetic field model

The second numerical model that is implemented is used to calculate the magnetic field strength in the fluid film. As the magnetic field depends strongly on the dimensions and relative distances of the components of the setup (electromagnet, bearing and shaft), a three-dimensional model had to be constructed to calculate the magnetic field strength within the fluid film. The output of this model (the magnetic field strength in the fluid film) was used as an input for the fluid flow model to determine the viscosity of the MR fluid. First, the theoretical background of the model is discussed in subsection 3.2.1 . Second, the determination of the material properties is explained in subsection 3.2.2. Finally, the COMSOL implementation of the magnetic field model is discussed in subsection 3.2.3.

3.2.1. Theoretical background

The magnetic field is induced by an electromagnet consisting of a coil and a yoke. Using Equation 3.21 [17] the magnetic flux density within a material can be determined, with μ_0 the magnetic permeability of free space ($4\pi 10^{-7}$), **M** the magnetization of the material, **H** the magnetic field strength and μ_r the relative magnetic permeability of the material.

$$\mathbf{B} = \mu_0(\mathbf{H} + \mathbf{M}) = \mu_0\mu_r\mathbf{H} \tag{3.21}$$

To calculate the magnetic field strength, COMSOL solves Equation 3.22, Equation 3.23 and Equation 3.24 [18], where **J** is the current density, **A** is the magnetic vector potential (the variable solved for), σ is the electrical conductivity, **E** is the electric field intensity and $\mathbf{J_e}$ is the externally generated current density (specifically the current in the coil here).

$$\nabla \times \mathbf{H} = \mathbf{J} \tag{3.22}$$

$$\mathbf{B} = \nabla \times \mathbf{A} \tag{3.23}$$

$$\mathbf{J} = \sigma \mathbf{E} + \mathbf{J_e} \tag{3.24}$$

$\mathbf{J_e}$ is calculated using Equation 3.25 [18], where N_{coil} is the amount of windings, I_{coil} the current through the coil, A the area of the coil and $\mathbf{e}_{coil}$ is a vector field that represents the local wire density, length, average cross section and direction of the wires.

$$\mathbf{J_e} = \frac{N_{coil} I_{coil}}{A} \mathbf{e}_{coil} \tag{3.25}$$

The magnetic field strength normal to film height was determined and used as input for the fluid film model (as the magnetic field strength in that direction influences the formation of particle chains and thus the viscosity of the MR fluid).

3.2.2. Material properties

To accurately model the magnetic field in the fluid film, the magnetic permeability of the materials used must be known. The bearing was made from non-magnetic 3D-printed clear resin and therefore the relative magnetic permeability was set equal to 1. Furthermore, for the air and the fluid film the relative magnetic permeability was also set equal to 1. The relative magnetic permeability of the MR fluid could be greater than 1, however according to Zheng et al. [19] the relative magnetic permeability for MR fluids with volume fraction of $\sim$ 2% (as is the case for the MR fluid used in this thesis) is close to 1. The relative magnetic permeability of the iron shaft and electromagnet yoke is unknown, as this is generally not supplied by the raw material manufacturer. The relative permeability of ferromagnetic steel is in the range of 100-1000 [20]; however, the exact number is difficult to determine. To make sure the model accurately resembles the experimental magnetic field, the relative magnetic permeability of the shaft and yoke was determined by performing experimental measurements of the magnetic field strength for different current magnitudes. A simple 3D-printed test jig was made to mount the shaft and electromagnet (and keep the relative distance constant), with a small hole in between where a Gauss meter probe could be placed (see Figure 3.5).

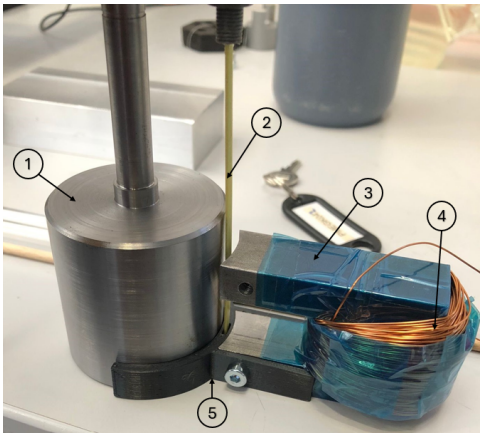

Figure 3.5: Setup to measure the magnetic field strength between the electromagnet and the shaft. 1 - Shaft, 2 - Gauss meter probe, 3 - Yoke, 4 - Coil, 5 - Test jig.

The magnetic field strength was measured for a current of 0A up to 2A, in steps of 0.1A. Furthermore, the test was repeated eight times. A linear fit was made through the origin using the measurements shown in Figure 3.6. As the magnetic field model is linear with respect to the current through the coil, this linear fit could be used to tune the relative permeability of the shaft and yoke. Because both were manufactured from similar materials, they were assumed to have equal relative permeability.

From the comparison of the magnetic field strength calculated using the magnetic field model and the experimental measurements, it was found that the relative magnetic permeability of the ferromagnetic steel used is ∼250, which is also in the expected range of 100-1000 for ferromagnetic steel. The relative magnetic permeability of the different components is summarized in Table 3.1.

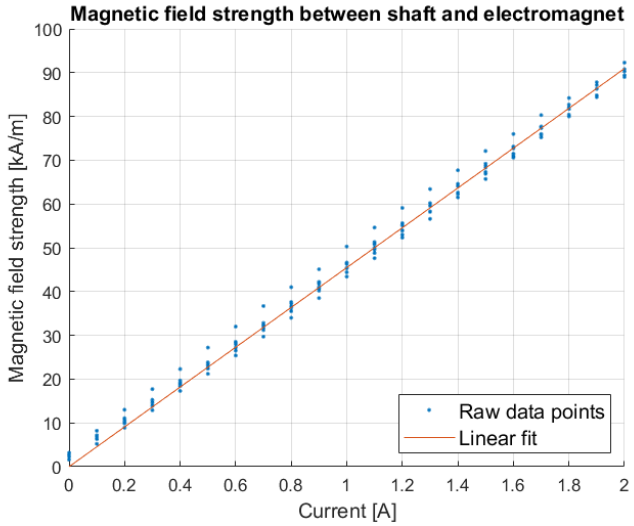

Figure 3.6: Linear fit of magnetic field strength versus current through coil.

Parameter	Value
μ_{shaft}	250
μ_{yoke}	250
$\mu_{bearing}$	1
μ_{air}	1

Table 3.1: Relative magnetic permeability of different components.

The assumption here is that the difference between the measurements and the model can be attributed solely to the unknown magnetic permeability and not to any other imperfections or effects that differ between the simulations and the experiments. This is of course not a correct assumption; however, it is used in this case because the magnetic field strength as calculated by the model is only needed to determine the viscosity of the MR fluid and in this way it is as close to the experimental magnetic field strength as possible.

3.2.3. COMSOL implementation

The magnetic field model was implemented in COMSOL using the Magnetic Fields (mf) interface. Quadratic order elements were used for the magnetic vector potential. Convergence was assumed when the relative tolerance was less than 1 x 10^{-3}. The model was made completely in three dimensions and without symmetry because due to the eccentricity of the shaft no symmetry plane could be determined. A large cube-shaped domain was created around the setup geometry with a magnetic insulation boundary condition on its boundary surfaces. The coil was modeled as a Homogenized Multiturn Conductor, which means the coil represents a bundle of insulated wires (as is the case for the coil in the experimental setup). To transfer the magnetic field strength from the three-dimensional magnetic field simulation to the two-dimensional fluid flow simulation, a general extrusion was used. The study of the model was broken down into two steps. First, a Coil Geometry Analysis was performed to compute the current flow in the coil. Afterwards, a stationary study was performed to compute the magnetic field strength in the domain. The computational domain is shown in Figure 3.7. Note that the bearing was simply modeled as a cylinder (and not as the full bearing), as the relative permeability was equal to 1 (similar to air) and it was only needed to create separate domains for the bearing and fluid film.

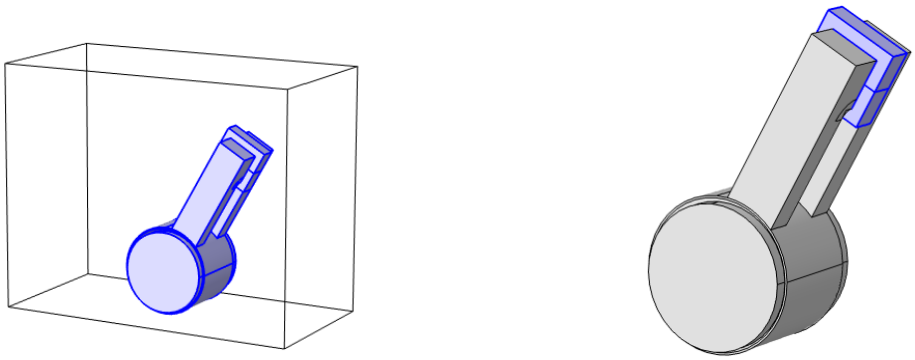

(a) Complete computational domain of the magnetic field simulation (including simulated box of air).

(b) Computational domain of the shaft, bearing and electromagnet (coil highlighted in blue).

Figure 3.7: Computational domain of the magnetic field simulation.

As the radial clearance is relatively large (1.25mm) and the range of eccentricity ratios tested for is also quite large (0.63-0.94), the distance between the yoke and shaft will vary quite a lot and have a significant effect on the magnetic field strength in the fluid gap. Therefore, the magnetic field simulation is performed for every eccentricity ratio separately (instead of for just one eccentricity ratio as is done in most literature) to accurately calculate the magnetic field strength. This does increase the computational costs significantly, as the three-dimensional magnetic field model is computationally heavy compared to the fluid film model. A free tetrahedral mesh was generated where the size was set to 'coarse' for the simulated air around the setup and 'normal' for the yoke, coil and shaft, as these are relatively large parts where no exact output is required from. The mesh size in the bearing and fluid gap was set to 'finer' as these are relatively small domains and an increased amount of mesh elements smooths the magnetic field strength solution, which is directly coupled to the fluid flow model to calculate the viscosity of the MR fluid. A too coarse mesh in these domains causes numerical spikes, which causes unrealistic local viscosities. This results in 1,895,328 DoF solved for or 351,685 mesh elements (the exact number depends on the eccentricity ratio of the shaft). The final mesh (excluding the simulated air around the setup) is shown in Figure 3.8.

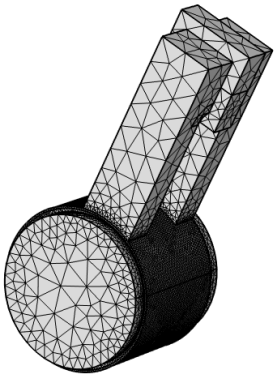

Figure 3.8: Mesh used in the magnetic field model.

The magnetic field strength normal to the film height at the bearing surface (the change in magnetic field strength over the film height is negligible) for ϵ_X = 0 and $I_{coil} = 1.2A$ is given in Figure 3.9a. As expected, the magnetic field is symmetric around the middle of the bearing, relatively constant in the areas covered by the yoke and is very close to zero elsewhere in the bearing. The magnetic field strength normal to the film height for $\epsilon_X = 0.94$ and $I_{coil} = 1.2A$ is shown in Figure 3.9b. Note that

the magnetic field strength is significantly stronger but also less uniform in the area covered by the yoke. This is because the magnetic field strength is strongly related to the distance between the yoke and shaft, which is not a constant distance in the area covered by the yoke when an eccentricity in X-direction is applied to the shaft.

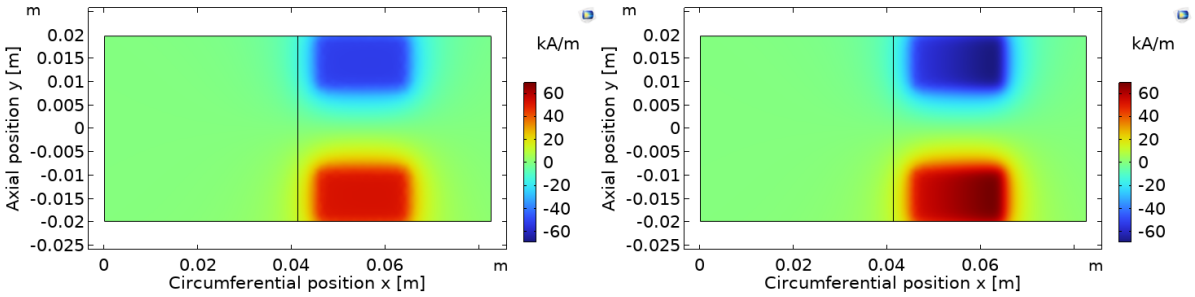

(a) $\epsilon_X = 0$ **(b)** $\epsilon_X = 0.94$

Figure 3.9: Magnetic field strength normal to the fluid film at the bearing surface for $I_{coil} = 1.2A$ and two different values of ϵ_X.

4

Results and discussion

The numerical and experimental results will be discussed in this chapter. The experimental and numerical results are presented for the experiments with hydraulic oil and MR fluid as lubricant in section 4.1 and section 4.2 respectively. Both sections follow the same structure, where the numerical and experimental results are presented first, followed by a discussion of the results and an explanation of the differences between the model and experiments. Section 4.3 elaborates on the visual results and performance of the demonstrator setup. Finally, in section 4.4 the performance of the semi-actively controlled hydrodynamic journal bearing lubricated with MR fluid is discussed in relation to the research objective.

4.1. Hydraulic oil lubrication

In this section the experimental and numerical results of the hydraulic oil lubricated hydrodynamic journal bearing will be presented and discussed. First, the results are presented in subsection 4.1.1. Afterwards, the results and the differences between the experimental and numerical results are discussed in subsection 4.1.2.

4.1.1. Results

As explained in section 2.8 the temperature varied during and between tests. Because the viscosity strongly depends on the temperature, a direct comparison of the individual tests is not representative. To compensate for the change in temperature and thus viscosity, the experimental results are normalized for the temperature measured during the test. This is done by calculating the relative change in viscosity with respect to the viscosity at 25°C and multiplying the measured pressure and forces by this factor. This is a valid method because forces and pressure should scale linearly with viscosity based on the Reynolds equation. The lubricant temperature during individual tests, the viscosity of the hydraulic oil at this temperature and the relative viscosity with respect to the viscosity at 25°C are given in Table 4.1. All results presented in this section are normalized for temperature, but plots of the raw data (not normalized for temperature) can be found in Appendix F.

Test number	Lubricant temperature [°C]	Viscosity [mPas]	Viscosity at 25°C relative to viscosity at measured temperature
1	23	70.9	0.89
2	24	66.8	0.95
3	25	63.1	1
4	27	56.8	1.11
5	29	51.2	1.23

Table 4.1: Temperature, viscosity and relative viscosity during different tests.

Pressure

The pressure is measured at ten circumferential positions on the bearing, which are again shown for reference in Figure 4.1.

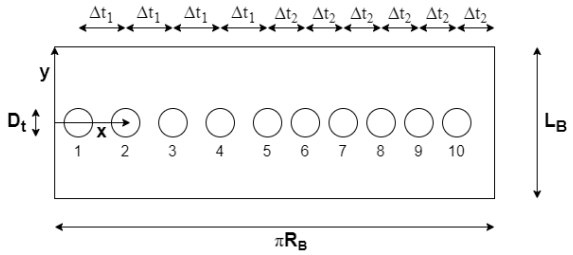

Figure 4.1: Locations of the ten pressure tubes schematically shown on the 'flattened' bearing.

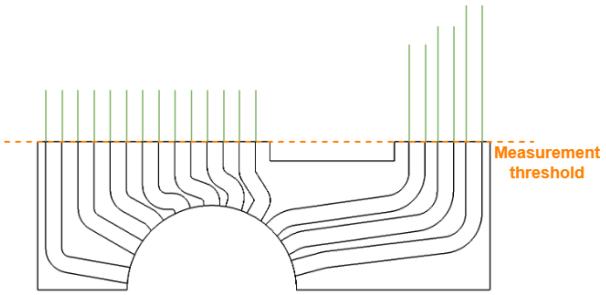

Figure 4.2: Measurement threshold. Level below which the fluid pressure could not be determined. External pressure tubes are shown in green.

The experimental results of the pressure distribution for different eccentricity ratios are shown in Figure 4.3. The shaded areas indicated the maximum and minimum of the experimental measurements and the dashed line indicates the mean of the five measurements performed. The "minimum measurable pressure" represents the pressure below which the pressure could not be determined experimentally. This is because it was impossible to accurately determine the height of the fluid column once it did not reach the measurement threshold (equal to the top of the bearing as shown in Figure 4.2), because the bearing was not fully transparent. The parabolic shape of the "minimum measurable pressure" is caused by the difference in height (with respect to the top of the bearing) of the inlets due to the circular shape of the bearing.

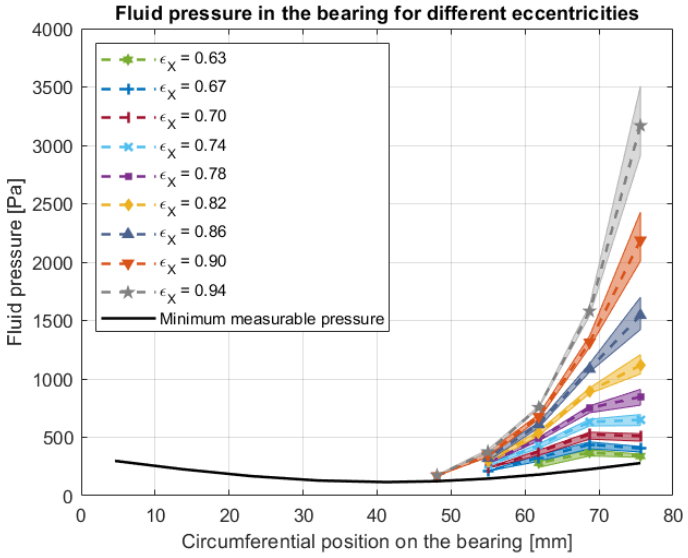

Figure 4.3: Experimental pressure distribution for different eccentricity ratios with hydraulic oil lubricant compensated for temperature.

At first glance, it may seem that the experimental pressure measurements are missing on the left side of the bearing (small values of the circumferential position) because the experimental data are not plotted there. However, this means that the pressure measurements of the individual experiments were all below the minimum measurable pressure and would therefore result in a pressure of zero. To avoid confusion for the reader, these data points are omitted from the graph and only measured pressures are displayed. Furthermore, for data points where the mean is slightly above the threshold, some

pressure measurements of individual experiments were actually below the threshold. As the exact pressure was unknown in these cases, they were also removed from the mean and spread of the data points. It could be argued that setting the pressure equal to the minimum measurable pressure would better show the spread of these data points. However, since the data points need to be normalized for temperature and are therefore multiplied by the relative viscosity (factor), this assumption could result in an overestimation of the pressure and it was therefore decided to omit those data points.

It can be seen that the repeatability of the experiments is good with a wider spread for the maximum pressure of each eccentricity ratio. This is logical because the peak pressure is the most sensitive to small changes in the bearing or testing conditions. The pressure increases for an increasing eccentricity ratio, where the increase in pressure (between subsequent eccentricity ratios) is also larger for higher eccentricity ratios.

In Figure 4.4 the experimental results are compared with the numerical results for each eccentricity ratio. For an increasing eccentricity ratio ϵ_X, the pressure increases and the maximum pressure moves towards the right side of the bearing (towards the location of minimum film thickness). Around the center of the bearing the numerical pressure is generally larger than the experimental pressure. However, the slope of the experimental pressure profile is larger than that of the numerical pressure, which means that the experimental pressure is larger close to the minimum film thickness (on the right side of the bearing, except for ϵ_X = 0.94). For ϵ_X = 0.63, 0.67, 0.70, 0.74 and 0.78, the model predicts a decrease in pressure for the pressure tube located on the right side of the bearing relative to the pressure tube on its left. This pressure decrease towards the minimum film thickness is only observed in the experimental results for ϵ_X = 0.63, 0.67 and 0.70.

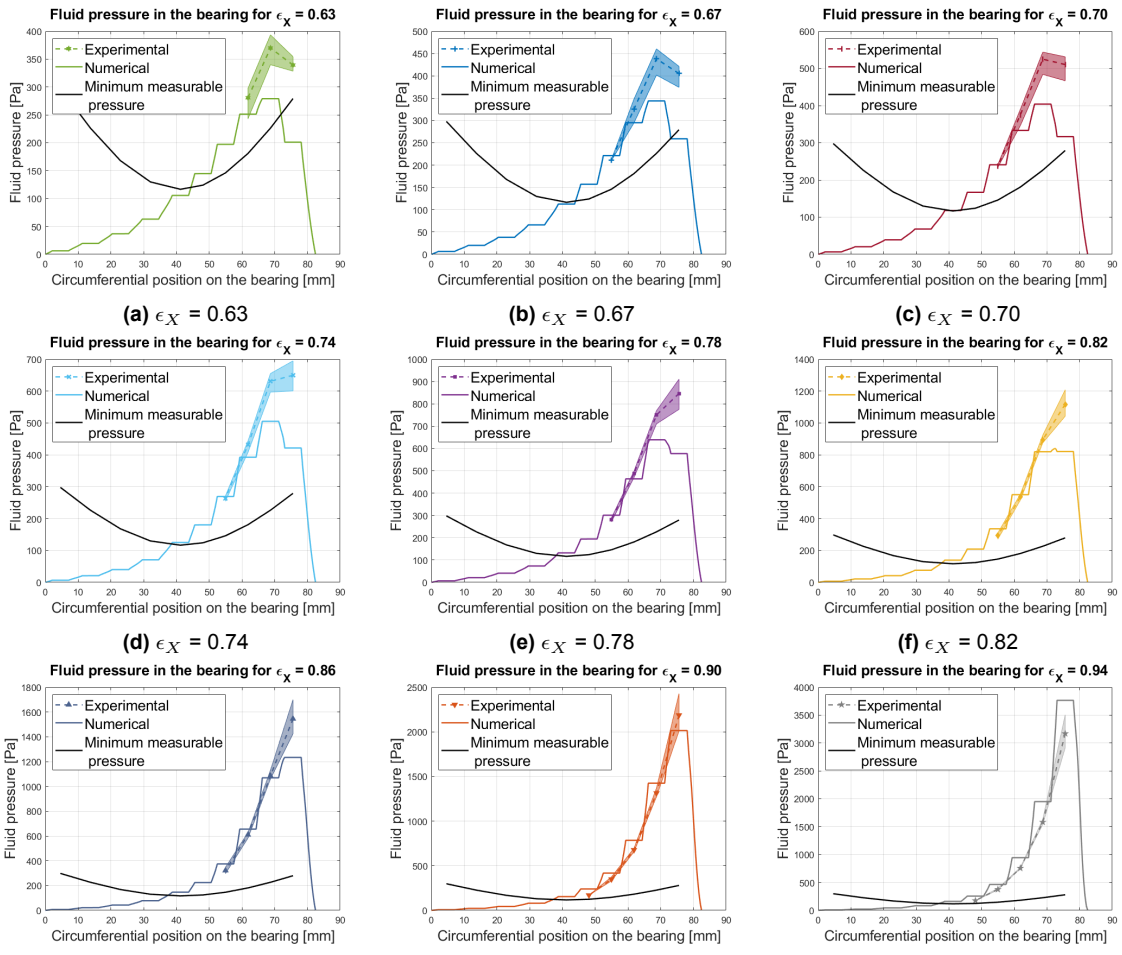

(a) ϵ_X = 0.63 **(b)** ϵ_X = 0.67 **(c)** ϵ_X = 0.70

(d) ϵ_X = 0.74 **(e)** ϵ_X = 0.78 **(f)** ϵ_X = 0.82

(g) ϵ_X = 0.86 **(h)** ϵ_X = 0.90 **(i)** ϵ_X = 0.94

Figure 4.4: Experimental and numerical results of the pressure distribution at the center of the bearing with hydraulic oil lubricant for different eccentricity ratios.

Generated forces

The experimental and numerical results of the horizontal force F_X, vertical force F_Y, friction force F_f and the force magnitude F_{mag} plotted versus the eccentricity ratio ϵ_X are given in Figure 4.5. In Figure 4.6 the Stribeck curve for constant speed is presented, which plots the friction coefficient μ versus $\frac{1}{F_{mag}}$ (the force magnitude on the x-axis is varied by changing the eccentricity ratio). As both the force magnitude F_{mag} and the friction coefficient μ vary between the individual experimental measurements, the spread should be in two dimensions (a spread on the x-axis and on the y-axis per eccentricity). However, to make the graph more readable and easier to interpret, the Stribeck curve is plotted with the inverse of the mean force magnitude on the x-axis and the spread between measurements is given as a shaded area on the friction coefficient μ (y-axis). One measurement set had big and clear outliers on the friction force and was therefore removed from these plots.

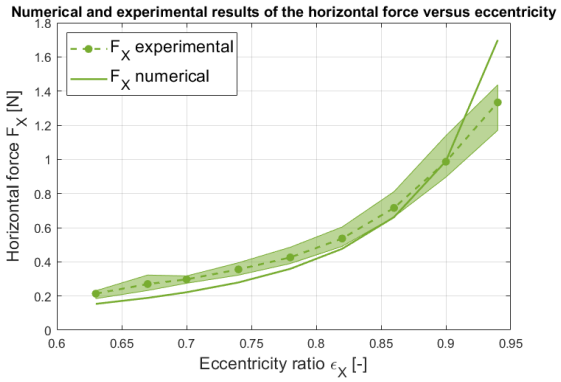

(a) Experimental and numerical horizontal force (F_X) plotted versus eccentricity ratio.

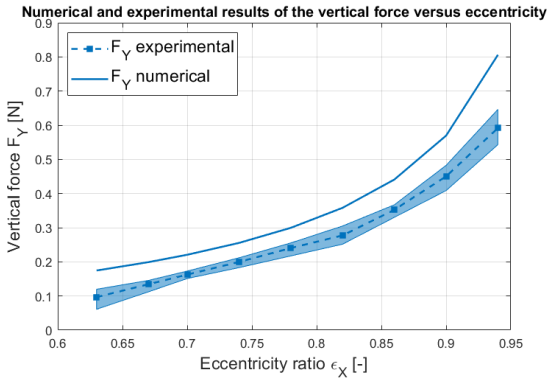

(b) Experimental and numerical vertical force (F_Y) plotted versus eccentricity ratio.

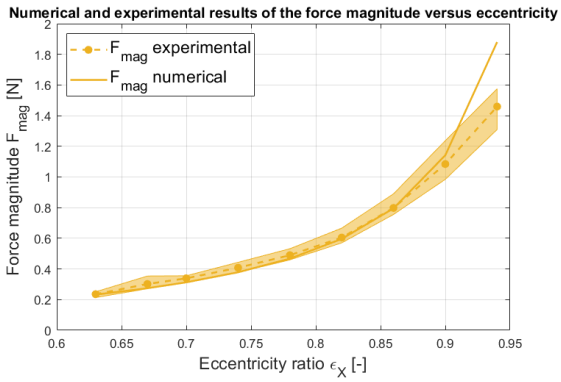

(c) Experimental and numerical force magnitude (F_{mag}) plotted versus eccentricity ratio.

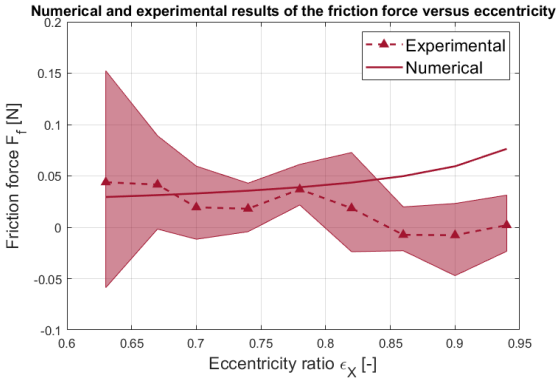

(d) Experimental and numerical friction force (F_f) plotted versus eccentricity ratio.

Figure 4.5: Experimental and numerical results of the generated forces in the bearing with hydraulic oil lubricant.

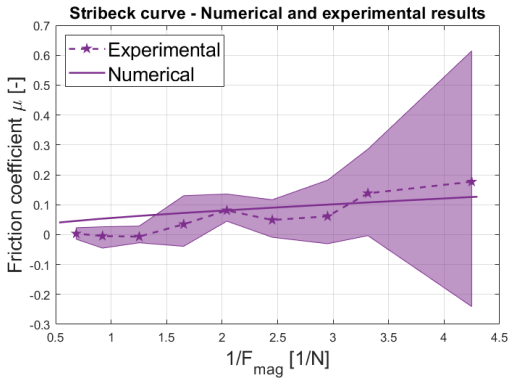

Figure 4.6: Experimental and numerical Stribeck curve for hydraulic oil for a constant speed of ω = 50rpm.

When comparing the experimental and numerical results, it is interesting to see that the general trend of the load-carrying forces (F_X, F_Y and F_{mag}) is similar between the experimental and numerical results. All of them are increasing with increasing eccentricity ratio and the force increase grows with eccentricity ratio. The experimental results for the horizontal force are a bit higher than the numerical model except for the highest eccentricity ratio tested for. The experimental vertical force is significantly lower than the numerical force, although the shape of the graph is comparable. Looking at the force magnitude, the results match pretty well except for ϵ_X = 0.94, where the numerical force is much larger.

Upon analysis of the friction force, it must be noted that the spread in the experimental measurements is quite a bit larger than for the load-carrying forces. The general trend of the experimental friction force is that it slightly decreases with eccentricity ratio and even becomes slightly negative for some eccentricity ratios. This is very unrealistic, as this means that the friction experienced by the bearing is in the opposite direction of the rotational direction of the shaft. The numerical friction force is of similar magnitude, but increases with increasing eccentricity ratio. Looking at the Stribeck curve, both the experimental and numerical results are of similar magnitude and the general trend is comparable, where the friction coefficient increases with decreasing force magnitude (or equivalently increasing $\frac{1}{F_{mag}}$). The experimental friction coefficient for the smallest values of $\frac{1}{F_{mag}}$ is smaller than the numerical model, mainly due to the very small (or even negative) friction force measured.

4.1.2. Discussion

Decent agreement is observed between the numerical and experimental results; however, mainly on the pressure distribution, vertical force and friction force clear differences can be seen. In addition to the visual comparison of the results in the figures in the previous section, the differences between the numerical and experimental results as a percentage of the numerical results are given in Table 4.2. A positive value means that the experimental result is larger than the numerical result. The color coding indicates the magnitude of the difference, where red means a large difference and bright green means a small difference (close to 0%).

ϵ_X	P_{max}	F_X	F_Y	F_{mag}	F_f
0.63	33%	39%	-45%	1%	49%
0.67	27%	43%	-33%	10%	33%
0.7	30%	34%	-26%	8%	-41%
0.74	29%	27%	-22%	8%	-49%
0.78	32%	19%	-20%	5%	-5%
0.82	33%	13%	-23%	1%	-57%
0.86	25%	8%	-20%	0%	-115%
0.9	9%	0%	-21%	-5%	-113%
0.94	-16%	-22%	-27%	-22%	-97%

Table 4.2: Difference between the numerical and experimental results as percentage of numerical results for hydraulic oil lubrication. A positive value means that the experimental result is larger than the numerical result.

Pressure and load-carrying forces
The general change in pressure and load-carrying forces for increasing eccentricity ratio is consistent between the experimental results and the numerical model as discussed above. Looking at the horizontal and vertical forces, both the experimental and numerical results show an increase in force with increasing eccentricity, where the horizontal force increases more strongly than the vertical force. This is expected as the maximum pressure moves towards the minimum film thickness (on the right side of the bearing) for increasing eccentricity ratio, primarily causing a rise in horizontal force. Moreover, more pressure builds up with an increasing eccentricity ratio, so the maximum pressure and the magnitude of the forces increase as well. In addition, the fact that the generated forces increase more rapidly with increasing eccentricity ratio is expected, as the relative change in minimum film thickness increases.

As can be seen in Table 4.2 and Figure 4.5c, the force magnitude shows good agreement between the experimental results and the numerical model, while larger differences can be seen for the maximum pressure, the horizontal force and vertical force (especially for the vertical force). The experimental horizontal force is generally larger than the numerical model (except for ϵ_X = 0.94), while the experimental vertical force is significantly smaller compared to the model. The magnitude of the experimental force matches pretty well with the model, where the difference is only in the range of -5% to 10% (except for ϵ_X = 0.94, which will be discussed separately). The experimental maximum pressure is generally higher than that found using the numerical model, with a difference of 9% to 33% (again except for ϵ_X = 0.94). The differences are quite significant, which can be caused by multiple factors.

First of all, the difference can be explained by the uncertainty in eccentricity. Due to a non-perfect alignment of the bearing and shaft and an uncertainty on the prescribed displacement of the bearing, the exact position of the shaft in the bearing is uncertain and varies during a rotation of the shaft. As no distance sensors were implemented, this made it impossible to precisely determine the horizontal and vertical eccentricity ratio during the tests. The uncertainty was further increased due to the finite stiffness of the compliant joint and bearing. The finite stiffness was adjusted for as explained in subsection 2.7.3; however, it still introduces an additional uncertainty. Determining when the micrometer screw started moving the bearing was very difficult (as also explained in section 2.8), as this depends on the angular position of the shaft due to its eccentricity with respect to its supporting ball bearings (it was found during the experiments that the position of the shaft with respect to the bearing varied during a rotation of the shaft). In addition, the mounting of the bearing introduced an uncertainty in the vertical eccentricity ratio ϵ_Y, which has been minimized by installing the bearing using gauge blocks. Imperfections and tolerances on the edges of the 3D-printed bearing could still affect the vertical eccentricity ratio and cause it to differ from what is used in the numerical model.
As an uncertainty on both ϵ_X and ϵ_Y is present and both influence the generated pressure and forces differently, it is difficult to determine whether there exists a combination of both for which the results match better (within a realistic uncertainty range). The only way to know for sure whether the differences between model and experiments are mainly influenced by a difference in eccentricity ratio between the experiments and model is by implementing distance sensors in the setup to accurately measure the eccentricity.
The uncertainty in both eccentricity ratios can cause the film height profile in the numerical model to differ from the film height profile in the experimental setup. This means that the pressure profile will differ and can cause the direction of the force magnitude to be different in the numerical model and the experiments, while the magnitude could be similar. Therefore, this could be a reason why the magnitude of the force vector agrees better with the model than the horizontal and vertical force.
A final note can be made about why the experimental maximum pressure and the forces generated for ϵ_X = 0.94 are much lower than the model. This probably has to do with the fact that the fluid gap became so small for this measurement that it might even be reduced to zero at some places in the bearing during a shaft revolution (due to the imperfect alignment and shape of the bearing and shaft). This could cause the generated pressure to be significantly lower than expected because the lubricant is pushed out momentarily or locally, and therefore the pressure cannot build up fully. Basically, the eccentricity ratio became too high to create a reliable film height, as variations in the film height during operation are too significant (since the minimum film height for ϵ_X = 0.94 is only 75μm).

The second reason for the significant differences in pressure distribution and load-carrying forces could be the exact shape of the bearing, which is not a perfect circle with the intended radius. As explained in subsection 3.1.4, the actual bearing shape was measured and implemented in the model to com-

pensate for this. However, since the model assumes a constant film height in the axial direction and the measurements showed a change in radius along the axial direction, this introduced an error with respect to the experimental setup. Furthermore, misalignment of the shaft and bearing also means that the film thickness changes in the axial direction. Finally, since the bearing is not a perfect circle, the normal force to the bearing surface is at a slightly different angle compared to the case where the bearing surface is perfectly circular (which is used to calculate the horizontal and vertical force component in the numerical model).

Third, the differences in force magnitude could be caused by inaccurate measurements of the load cells, mainly for the vertical force. Two factors could play a role here. First, a source of error could be the calibration forces. As explained in section 2.7, calibration measurements were performed without a rotating shaft to determine the forces in the load cells due to internal stresses, bearing weight and the force exerted by the deformed leaf springs. A small change in conditions between calibration and testing (e.g. slightly different eccentricity ratio or slightly different internal stresses due to vibrations or touching of the setup) could influence the accuracy of the calibration forces. This effect was also observed as the calibration forces between different measurements differed, especially for the vertical load cells, while these should ideally be identical. Second, the friction force at the micrometer screw, which takes up part of the vertical force, could be a source of error on the measured vertical force. Any friction force present here decreases the vertical force measured. Due to the introduction of the compliant joint, this friction force was shown to only take up a small portion, only around $\sim 1\%$, of the vertical load (see Appendix B).

Fourth, the implementation of the load-carrying forces due to the shear force could be incorrect. As explained in subsection 3.1.5, the resulting forces due to the shear force were found to differ on the shaft and bearing side. The difference was assumed to be due to a geometry term which was not correctly implemented and therefore the forces calculated at the shaft side were used (as this is assumed to be the 'flat' surface in the model). More research is needed to find out whether the implementation is indeed correct now and if the difference is indeed only due to a geometry term in the calculation on the bearing side. Again, the differences between the experimental and numerical results are larger than the impact the shear force can have on the load-carrying forces, so it is not assumed to be the main reason for the differences.

Finally, the difference in pressure distribution (and thus also in force magnitude) could be influenced by the pressure tubes and mainly the tube inlets. The tube inlets have a diameter of 5mm, which is relatively large in the 40mm wide bearing (especially since 10 inlets are placed on a circumferential length of $\pi R_B \approx 82.5mm$). The inlets are placed on the center line of the bearing, where the pressure buildup is largest. These inlets are modeled as if the film height was very large at the inlet locations, causing the pressure to be constant at the inlets. This should be a good approximation, but could cause a difference between the model and reality. The weight of the lubricant present in the pressure tubes could also have a large influence on the vertical force measured. As explained in section 2.7, the weight of the lubricant in the pressure tubes was obtained using the measured height of the fluid columns. The weight was then added to the vertical force measured as it counteracts the hydrodynamic force generated. This implementation slightly underestimates the actual weight of the lubricant in the pressure tubes, because the pressure could only be measured once the fluid column rose above the measurement threshold (see Figure 4.2). The weight of the lubricant in the tubes with a pressure below the minimum measurable pressure was therefore neglected. This factor could explain in part why the experimentally measured vertical force is lower than the numerical vertical force. However, even if it was assumed that all tubes would at least be filled to the measurement threshold (which is a large overestimation as some tubes were basically empty for all eccentricity ratios), it would still account for only ~ 0.034N, which is less than the difference between the numerical and experimental vertical force.

In conclusion, it is most likely that the differences in pressure buildup and load-carrying forces are due to a combination of the uncertainty in eccentricity, tolerances of the bearing and shaft, modeling of the pressure tubes (and associated weight of the fluid in the pressure tubes) and misalignment of the shaft and bearing causing oscillations in film height during shaft revolutions.

Friction force

The numerical friction force increases with an increasing eccentricity ratio, which is as expected as the pressure builds up, causing a larger pressure gradient, which is proportional to the shear stress (see

also Equation 3.10). The experimental friction force has a large spread between measurements, but decreases slightly with increasing eccentricity ratio, which is not expected. The order of magnitude of the experimental friction force is comparable to that of the numerical model, indicating that it is in the correct range, although the difference between the model and the mean of the experimental measurements is still in the order of -115% to 49% (the spread on the individual experimental measurements is so large that the numerical friction force falls into the measurement range for ϵ_X = 0.63-0.0.82).

The uncertainties as discussed for the load-carrying forces (such as uncertainty on the eccentricity ratio, tolerances of the bearing and misalignment of bearing and shaft) are also valid here. Some additional causes for the difference in magnitude and trend of the friction force can be identified.

First, the friction force is calculated on the basis of the difference in measured force between the two vertical load cells. The step size in vertical force measured is $\pm 0.0087N$ due to the 12-bit data acquisition device (see subsection 2.4.3). This results in a step size of the friction force of $\pm 0.03N$, while the measured friction force ranges from -0.05 to 0.15N. This is a very significant step size and explains the large spread in the experimental results. Furthermore, this also explains why it is impossible with the current setup to measure the increase in friction force for increasing eccentricity ratio. Using a data acquisition device with more bits might solve this issue, although the amount of noise and oscillations in the vertical force is larger than the magnitude of the step size (due to vibrations and eccentricity oscillations during shaft revolutions) and might therefore still not provide a much more accurate measured friction force.

Other reasons for the measured friction force to decrease for an increasing eccentricity ratio are the frictional force at the compliant joint or misalignment of the horizontally applied force. Although the compliant joint minimizes the friction force, some friction will still be present, which opposes the moment exerted on the bearing. This means that the moment (and thus friction force) as measured by the vertical force sensors is smaller than the actual moment exerted. Moreover, if the horizontal force is not applied perfectly in line with the bottom of the bearing, a moment will be exerted (see Equation 2.4, a misalignment means that 'c' is not equal to zero). As the horizontal force is generally larger than the vertical force, a small misalignment could already have a significant effect on the determined friction force. The horizontal force and thus also the friction at the compliant joint increase with an increasing eccentricity ratio. Therefore, the decrease (and error) in the measured friction force due to these effects will increase with increasing eccentricity ratio.

Finally, compensation for the weight of the lubricant is also done using some non-perfect assumptions. As explained in section 2.5, the moment due to the weight of the fluid in the pressure tubes is implemented using the volume of the internal tubes and the measured height of the fluid column. This does not take into account the weight of the lubricant in the pressure tubes where the fluid did not rise above the measurement threshold (see Figure 4.2). This is the case for the tubes on the left side of the bearing (pressure is lowest there), meaning the friction is, in reality, a bit larger (if this fluid weight was correctly taken into account). In the extreme case where it is assumed that all tubes would at least be filled to the measurement threshold, the measured friction force would be increased by at most 0.03N. This could explain a large portion of the differences between the experimental and numerical results, especially for the larger eccentricity ratios where the measured friction force decreased. It would also be logical that this simplification has the most effect on measurements with high eccentricity ratios, because more "neglected" fluid is present in the pressure tubes on the left side of the bearing due to the larger pressure. It must be noted that this effect cannot explain the entire difference between the experimental and numerical results, since the difference for the three largest eccentricity ratios is larger than 0.03N.

In conclusion, the current setup can approximate the order of magnitude of the friction force but is not accurate enough to determine it accurately and measure the difference in friction force due to a change in the eccentricity ratio (for the current operating conditions).

Stribeck curve

Both the numerical and experimental Stribeck curves show an increase in the friction coefficient for decreasing force magnitude. This is expected as a smaller force magnitude is caused by a lower eccentricity ratio, and the force magnitude decreases stronger with decreasing eccentricity ratio than the friction force.

The large spread on the experimental friction coefficients is mainly caused by the friction force measurements. When comparing the experimental and numerical results, both curves have a similar shape and order of magnitude. The friction coefficient is lower for the experimental model (except for the two lowest force magnitudes), which is caused by the lower friction force and the slightly larger force magnitude. The causes of the differences have all been discussed in the discussion of the forces above. Although differences are significant, the general trend of the Stribeck curve is well captured in the experimental results.

4.2. MR fluid lubrication

In this section the experimental and numerical results of the hydrodynamic journal bearing lubricated with MR fluid will be presented and discussed. First, the results are presented in subsection 4.2.1. Then, the results and the differences between the experimental and numerical results are discussed in subsection 4.2.2.

4.2.1. Results

In contrast to the results with hydraulic oil as lubricant, the results with MR fluid as lubricant are not normalized for temperature. The reason is that the effect of temperature on viscosity strongly varies with the magnetic field strength and the shear rate (see Figure 2.11c and Figure 2.11d). Therefore, it is impossible to compensate the different experimental measurements for temperature with a simple factor or ratio. As the tests are performed on multiple days, the temperature spread between different tests is in the order of a few degrees Celsius. As this cannot be easily compensated for, a greater spread in the experimental results is expected. Furthermore, because of the heat produced by the electromagnet, the temperature of the MR fluid also increased during experiments when the magnetic field strength was increased. The mean and spread of the temperatures of the MR fluid in the oil pan, of the MR fluid near the magnet and of the magnet itself for the three tests performed for different values of I_{coil} are given in Table 4.3. As temperature effects are not included in the model and thus only one temperature can be chosen for which the model is solved, the average temperature of the oil near the magnet is used for each value of I_{coil}. This means that for I_{coil} = 0-0.4A the viscosity at a temperature of 23°C is used, for I_{coil} = 0.8A the viscosity at a temperature of 25°C and for I_{coil} = 1.2A the viscosity at a temperature of 30°C. These temperatures are chosen instead of the temperature of the MR fluid in the oil pan, as this is the temperature close to the maximum pressure in the fluid film and therefore, more critical to the pressure and forces generated.

I_{coil} [A]	Average temperature of lubricant in oil pan (range) [°C]	Average temperature of lubricant near magnet (range) [°C]	Average temperature of magnet (range)[°C]
0	23 (20-25)	23 (20-25)	23 (20-25)
0.4	23 (20-25)	23 (20-25)	23 (21-26)
0.8	23 (21-26)	25 (23-28)	29 (27-32)
1.2	25 (23-27)	30 (26-32)	40 (39-42)

Table 4.3: Temperature of the oil, oil near the magnet and magnet during experiments

Pressure

The experimental and numerical results of the pressure distribution for different eccentricity ratios and applied currents are shown in Figure 4.7. The results are grouped by eccentricity ratio to increase the readability of the plots. Again, the minimum measurable pressure is shown, but this is now slightly higher as a result of the larger density of the MR fluid compared to the hydraulic oil. Experimental data points below the minimum measurable pressure are omitted as was also done in the pressure plots for hydraulic oil lubrication. The repeatability of the experiments is slightly worse than for the tests with hydraulic oil; however, this was expected as these results are not compensated for temperature differences between measurements. In Appendix G the numerical and experimental pressure distributions have been plotted per eccentricity ratio and applied current in separate graphs, to improve the readability of the graphs and be able to compare the results in more detail.

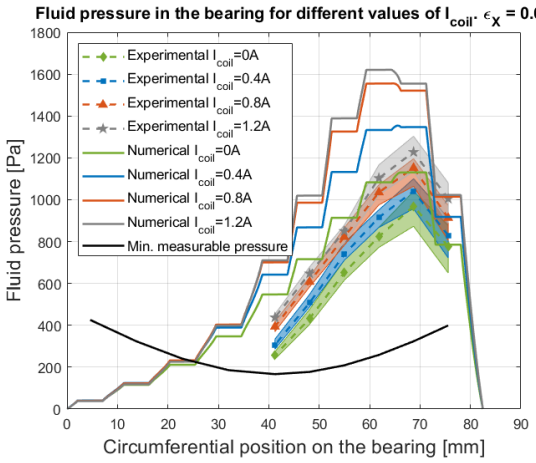

(a) $\epsilon_X = 0.63$

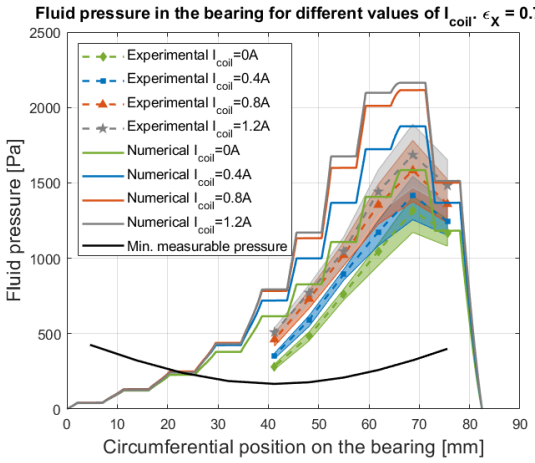

(b) $\epsilon_X = 0.70$

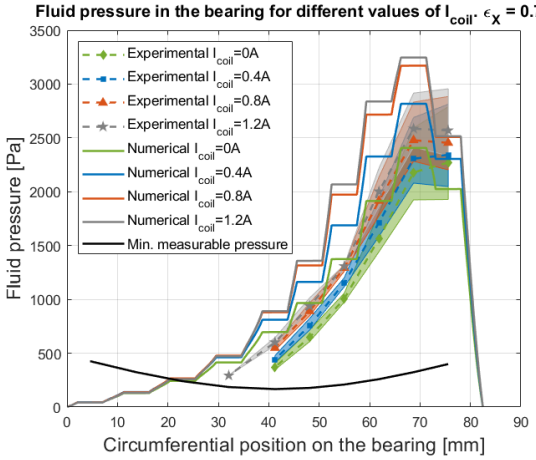

(c) $\epsilon_X = 0.78$

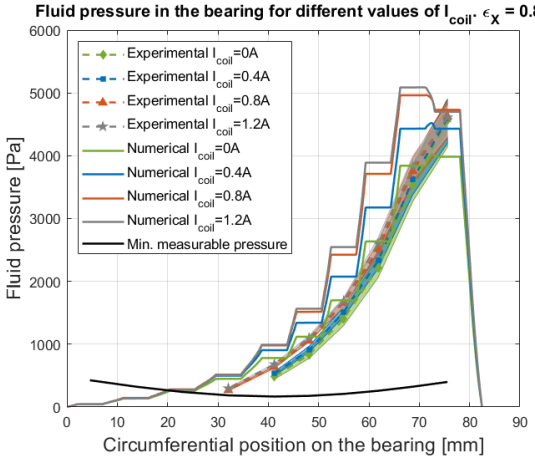

(d) $\epsilon_X = 0.86$

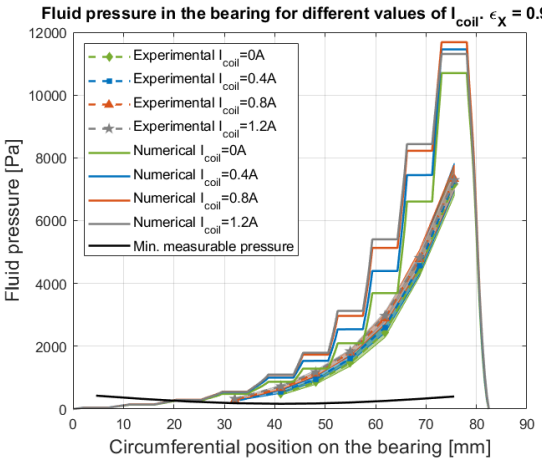

(e) $\epsilon_X = 0.94$

Figure 4.7: Experimental and numerical results of the pressure distribution at the center line of the bearing with MR fluid lubricant for different eccentricity ratios and values of applied current.

Similarly to the results with the hydrodynamic oil, the pressure increases for increasing eccentricity ratio, where the relative increase (between subsequent eccentricity ratios) is larger for a larger eccentricity ratio. This is observed for both the experimental and numerical results. Furthermore, the numerical pressure distribution is larger than the experimental one and the increase in numerical pressure due to an increase in applied current is also larger (meaning the difference between numerical and experimental results increases for increasing applied current). For ϵ_X = 0.63, 0.70, 0.78 and 0.86 the numerical and experimental pressure distributions are relatively comparable in magnitude while for ϵ_X = 0.94 the numerical pressure distribution is significantly larger. Moreover, note that the pressure decreases towards the most right measurement point for ϵ_X = 0.63, 0.70 and 0.78, which is the case in both numerical and experimental results, while for ϵ_X = 0.86 this is only the case for the numerical results. Finally, note that for ϵ_X = 0.94 the numerical maximum pressure is lower for I_{coil} = 1.2A compared to I_{coil} = 0.4 and 0.8A. This is caused by the much higher temperature for I_{coil} = 1.2A. In the experimental results this is not really observed, although it must be noted that (as explained in subsection 2.7.2) a decrease in pressure was almost impossible to measure, as a layer of the opaque MR fluid sticks to the inside of the pressure tube even if the height of the fluid column decreases.

Generated forces

The experimental and numerical results of the horizontal force F_X, vertical force F_Y, friction force F_f and force magnitude F_{mag} plotted versus eccentricity ratio ϵ_X are given in Figure 4.8. Figure 4.9 shows the Stribeck curve, which plots the friction coefficient μ versus $\frac{1}{F_{mag}}$. The same procedure to create the Stribeck curve as explained in subsection 4.1.1 is used. All plots show the results for different values of applied current. One measurement with $\epsilon_X = 0.70$ had large and clear outliers and was therefore removed from the results.

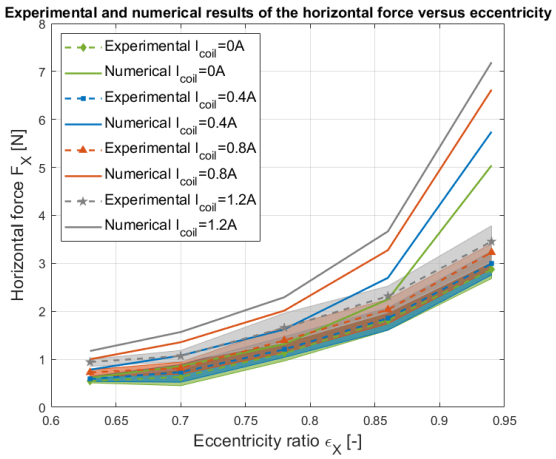

(a) Horizontal force (F_X)

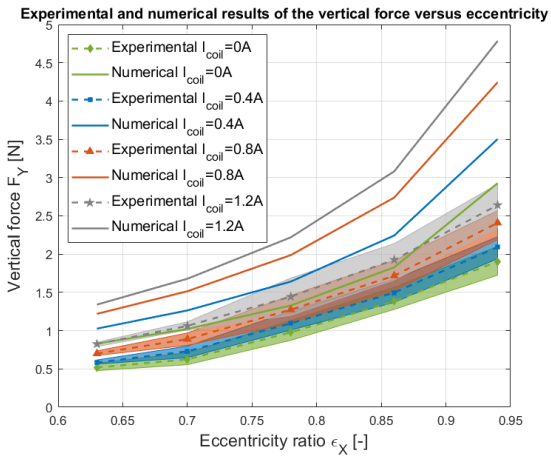

(b) Vertical force (F_Y)

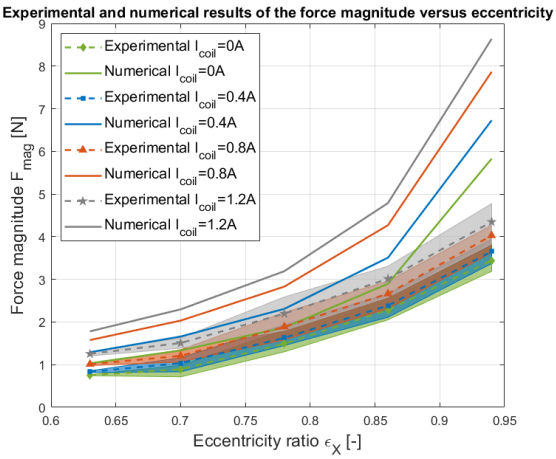

(c) Force magnitude (F_{mag})

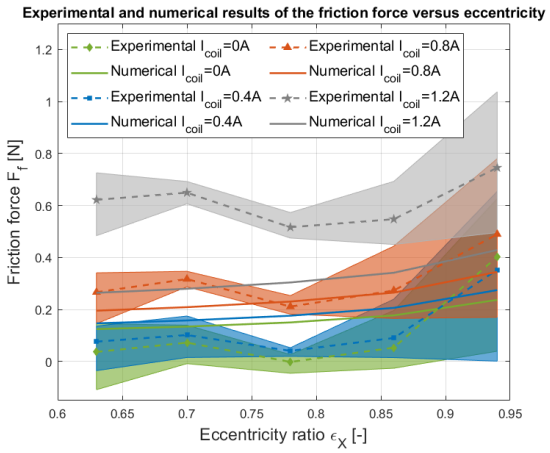

(d) Friction force (F_f) plotted versus eccentricity ratio.

Figure 4.8: Experimental and numerical results of the generated forces in the bearing with MR fluid lubricant for different values of I_{coil}.

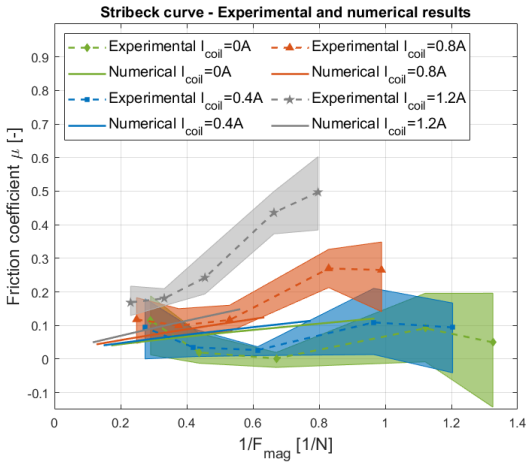

Figure 4.9: Experimental and numerical Stribeck curves for MR fluid for a constant speed of ω = 50rpm.

The repeatability of the experiments is slightly worse than for the experiments with hydraulic oil, which is expected due to the temperature differences between measurements. The spread on the friction force is again quite large.

Comparing the experimental and numerical results for the load-carrying forces (F_X, F_Y and F_{mag}) it can be seen that the general trend is similar, where all are increasing for increasing eccentricity ratio. Furthermore, all of them increase for increasing current applied. However, significant differences between the experimental and numerical results are also present. First, the numerical model results for all three forces are larger than the experimental measurements. This difference is largest for the vertical force, while for the horizontal force the difference is slightly smaller. Secondly, note that the numerical forces increase more rapidly with increasing eccentricity ratio compared to the experimental results, resulting in an increase in difference between both results. Especially for the highest eccentricity ratio (ϵ_X = 0.94) the differences become very large. Analyzing the effect of the applied current on the results, it is clear that in the numerical model the increase in generated forces is much larger than in the experimental results (although for both the forces do increase with increasing applied current).

Looking at the friction force, a large spread in the experimental results is observed, making it more difficult to analyze the trend of the results. The numerical friction force increases slightly but steadily with increasing eccentricity ratio while the experimental friction force remains approximately constant for ϵ_X = 0.63-0.86 and increases for ϵ_X = 0.94. Especially for I_{coil} = 0 and 0.4A the experimental friction force increases a lot for ϵ_X = 0.94. Both the numerical and experimental results show an increase in friction force for increasing applied current; however, the increase is greater for the experimental results compared to the numerical results (in contrast to the results for the load-carrying forces). The magnitude of the experimental friction force is smaller for I_{coil} = 0 and 0.4A, while for I_{coil} = 0.8 and 1.2A the experimental friction force is greater than the numerical one.

The Stribeck curve is again constructed using the force magnitude and the friction force results. For the numerical results, the friction coefficient increases roughly linearly with increasing $\frac{1}{F_{mag}}$. For the experimental results, the friction coefficient fluctuates slightly, but increases slightly with increasing $\frac{1}{F_{mag}}$ when I_{coil} = 0 and 0.4A (except for the point with the lowest value of $\frac{1}{F_{mag}}$ which corresponds to ϵ_X = 0.94) and increases more strongly with increasing $\frac{1}{F_{mag}}$ for I_{coil} = 0.8 and 1.2A.

Furthermore, the slope of the Stribeck curves (both numerical and experimental) increases with increasing applied current. The increase in slope is larger for the experimental results. The lower experimental force magnitude can also be observed in the Stribeck curve. The difference in the friction coefficient increases for increasing values of applied current, as the numerical F_{mag} increases more with increasing applied current, while the friction force increases less with increasing applied current compared to the experimental results.

4.2.2. Discussion

The observed agreement between the numerical and experimental results is worse than for the results with hydraulic oil as lubricant. The differences in generated forces and maximum pressure are given as a percentage of the numerical results in Table 4.4. It can be quickly observed that the generated load-carrying forces and the maximum pressure are larger for the numerical results as compared to the experimental results. For the friction force, it is clear that for increasing applied current, the experimental friction force increases much more. The discussion of the causes of the differences in the results with oil as lubricant in subsection 4.1.2 is still valid; therefore, only additional effects (due to the usage of MR fluid) are discussed.

P_{max}	I_{coil} 0	0.4	0.8	1.2
ϵ_X 0.63	-14%	-23%	-26%	-24%
0.7	-17%	-24%	-25%	-22%
0.78	-6%	-17%	-22%	-20%
0.86	14%	2%	-7%	-9%
0.94	-33%	-37%	-37%	-36%

(a) P_{max}

F_{mag}	I_{coil} 0	0.4	0.8	1.2
ϵ_X 0.63	-27%	-36%	-36%	-30%
0.7	-33%	-38%	-41%	-34%
0.78	-20%	-29%	-33%	-31%
0.86	-21%	-32%	-38%	-37%
0.94	-41%	-46%	-49%	-50%

(b) F_{mag}

F_X	I_{coil} 0	0.4	0.8	1.2
ϵ_X 0.63	-11%	-25%	-27%	-20%
0.7	-26%	-32%	-40%	-32%
0.78	-15%	-26%	-31%	-28%
0.86	-19%	-31%	-38%	-37%
0.94	-43%	-48%	-51%	-52%

(c) F_X

F_Y	I_{coil} 0	0.4	0.8	1.2
ϵ_X 0.63	-38%	-43%	-43%	-41%
0.7	-39%	-42%	-41%	-39%
0.78	-26%	-33%	-36%	-37%
0.86	-24%	-33%	-37%	-39%
0.94	-35%	-40%	-43%	-46%

(d) F_Y

F_f	I_{coil} 0	0.4	0.8	1.2
ϵ_X 0.63	-70%	-48%	36%	135%
0.7	-46%	-35%	52%	132%
0.78	-101%	-77%	-8%	70%
0.86	-70%	-56%	3%	60%
0.94	70%	28%	42%	74%

(e) F_f

Table 4.4: Difference between the numerical and experimental results as percentage of numerical results for MR fluid lubrication. A positive value means that the experimental result is larger than the numerical result.

Maximum pressure

Let us first look at the differences in maximum pressure. Where for the results with oil as lubricant, the experimental maximum pressure was mostly larger than the model, it is now smaller. One potential reason may be the high viscosity of the MR fluid. Due to the high viscosity, it took a lot of time for the MR fluid to reach equilibrium in the pressure tubes. Equilibrium was assumed as soon as the fluid did not increase more than 1mm in ten minutes of continuous operation. This does not guarantee that full equilibrium is reached, so it might be that the measured pressure is slightly lower than the actual pressure. The fluid column is not expected to rise much higher, as tests were performed in which the setup was operated continuously for significantly more time and no measurable change was observed. However, to be absolutely sure, the setup could be operated continuously for e.g. a day to see whether the fluid column height increases significantly (however, temperature would need to remain constant to not influence the pressure buildup as well). Moreover, when a magnetic field is present the MR fluid has a yield stress. As the shear rate is very small inside the pressure tubes, it could be possible that the yield stress is not fully overcome and that part of the pressure difference is taken up by friction between the fluid and the pressure tubes. The impact of both of these effects also increases with applied current (larger applied current means higher viscosity and yield stress), which explains why the differences become larger with increasing applied current.

Load-carrying forces

The numerical horizontal force, vertical force and force magnitude are, for the tests with MR fluid, all larger than the experimentally determined forces, where for the test with hydraulic oil the results for the horizontal force and force magnitude matched quite well. The vertical force has similar (or somewhat

larger) relative differences in magnitude compared to the results for hydraulic oil. The absolute differences are larger than the differences found in the tests with hydraulic oil, which is expected because of the higher viscosity of the MR fluid. The higher viscosity causes a small difference in e.g. film height to have a larger effect on the generated pressure and forces (since these scale linearly with viscosity).

The difference in vertical force could be larger because the neglected weight of the lubricant in the pressure tubes where the fluid did not reach the measurement threshold (see Figure 4.2) is much larger since the density of the MR fluid is higher. However, this was not found to be the case as only for the first 3 or 4 pressure tubes the MR fluid did not reach above the measurement threshold, where for the experiments with oil this was the case for 5-6 tubes due to the lower viscosity. Again, even assuming that all tubes would be filled at least to the measurement threshold (a large overestimation), it would account for only $\sim$0.038N, which is significantly less than the difference between the numerical and experimental vertical force.

Another reason for the larger differences could be the accuracy of the numerical model. The MR fluid is strongly shear-thinning, especially at low shear rates as encountered with the operating conditions in the experiments (encountered shear rates are in the range of 10-2500s^-1). The numerical model uses the shear rate in the middle of the fluid film to determine the viscosity of the MR fluid, not taking into account the variation in shear rate and thus viscosity over the film thickness. The shear rate over the film thickness is both larger and smaller compared to the shear rate in the middle, so the exact effect of this assumption is difficult to determine. It could definitely cause a significant difference in the generated forces (since viscosity directly influences the generated pressure). Implementation of the generalized Reynolds equation is needed to determine the effect of this simplification.

Lastly, the increase in the differences between the numerical and experimental results for increasing applied current has to be discussed. The difference in generated pressure and forces due to an applied magnetic field in the experimental results is much smaller compared to the numerical increase. The biggest reason for this is probably the effect of temperature. The electromagnet gets very hot when a current is applied, increasing the temperature of the lubricant. The lubricant temperature was measured and implemented in the model; however, the temperature could not be measured inside the bearing. It may be possible that the temperature in the film inside the bearing is higher than the temperature measured on the side of the bearing, resulting in a smaller increase in the generated pressure and forces than modeled.

Note that again the differences are largest for ϵ_X = 0.94, but as explained in the discussion of the results with hydraulic oil as lubricant, the very small film height in combination with the tolerances and alignment of the setup plays a significant effect for these measurements. Therefore, a discussion of the differences for these results is of less interest.

Friction force

The final measured force that needs to be discussed is the friction force. The experimental friction force is smaller for I_{coil} = 0 and 0.4A than the numerical friction force, but increases more strongly with increasing applied current. The magnitude of the effect of the neglected weight of the lubricant in some pressure tubes can also be estimated again. By assuming the extreme case where all tubes would be filled at least to the top of the bearing (the measurement threshold), the measured friction force would increase by at most 0.034N. This is smaller than the differences between the numerical and experimental friction force and would cause the difference to be even larger for I_{coil} = 0.8 and 1.2A. Therefore, an additional reason must be found to explain the larger increase in experimental friction force with increasing applied current compared to the numerical friction force.

An additional factor influencing mainly the friction force results for large applied currents is the calibration measurements. Due to the generated magnetic field the electromagnet (and thus bearing) is pulled towards the shaft. As the electromagnet is located on the right side of the bearing and the shaft has an eccentricity towards the right during experiments, this causes a positive moment on the force sensors. This should be corrected for by the calibration measurements; however, small differences in the magnetic field strength (and thus force) between the reference measurements and the actual measurements could quickly have a significant effect on the measured friction force. A small increase in force causes a significant increase in the measured friction force, while it is less significant on the (much larger) horizontal and vertical forces. A potential reason for the magnetic force to be slightly

higher during operation is the presence of MR fluid between the bearing and shaft (during calibration measurements the shaft is stationary and thus no lubricant is present between the bearing and shaft). The MR fluid used should have a relative magnetic permeability close to, but slightly above, 1 as explained in subsection 3.2.2. As its slightly above 1, it means that it slightly increases the magnetic field strength and thus potentially increases the magnetic force between the electromagnet and shaft. This increase scales with applied current and could thus cause an additional increase in the measured friction force with increasing applied current (next to the expected increase due to the increase in viscosity of the MR fluid).

Lastly, the assumption of neglecting the variation in shear rate and thus viscosity across the film height could potentially affect the friction force results more significantly than the load-carrying forces. The effect of this assumption could also be more significant for increasing applied current, as the shear rate profile is also influenced by the magnetic field.

Stribeck

Upon analysis of the Stribeck curve, quite large differences can be seen between the numerical and experimental curves. Interesting to note is that although the differences are relatively large, the general trend of larger maximum force magnitude (larger maximum load capacity), higher friction coefficient and steeper slope for increased applied current is present for both numerical and experimental results. The experimental friction coefficient decreases for increasing $\frac{1}{F_{mag}}$ from the most left data point for I_{coil} = 0 and 0.4A, which is not expected. However, this data point corresponds to ϵ_X = 0.94, for which mainly the friction force increased significantly (compared to the other eccentricity ratios). As explained before, the differences for ϵ_X = 0.94 were generally much larger compared to the other eccentricity ratios tested for as the film thickness is too small for the tolerances of the setup (the bearing and shaft might even come into contact during operation). Therefore, these experimental results cannot be easily compared with the results for other eccentricity ratios and the numerical model.

4.3. Visual results and demonstrator performance

Part of the second sub-objective was to create a visual demonstrator setup, where the effect of a magnetic field on the pressure distribution in a hydrodynamic journal bearing would be made visual. Pictures of the pressure distribution with an applied current of 0 and 1.2A and for two different eccentricity ratios are shown in Figure 4.10. Clearly, a large increase in the height of the fluid columns (which represents the pressure) can be seen when comparing ϵ_X = 0.78 and 0.94, with the largest increases in the tubes on the right. A (small) increase in the height of the fluid columns can be seen in all tubes when comparing for I_{coil} = 0 and 1.2A, where the largest increase is for the second and third tubes from the right. This shows that the setup does perform as a demonstrator which is able to show the effect of the eccentricity and magnetic field on the pressure; however, the performance is far from ideal.

First, because of the high viscosity of the MR fluid, the fluid flows very slowly into the tubes and it takes around an hour for the fluid to reach equilibrium. Once the magnetic field is increased it takes around 30 minutes to reach equilibrium again, during which the fluid column rises slowly but steadily. As the fluid rises so slowly, it is hard to see the increase by just looking at the setup and only when measuring the fluid column height the difference becomes obvious. A possible improvement would be to use diluted MR fluid with a lower viscosity so that it flows better in the tubes; however, this would also impact the magnetorheological effect. Diluting the fluid also decreases the yield stress of the MR fluid (under applied magnetic field) making it easier for the fluid to flow when a current is applied to the electromagnet. Another option would be to increase the tube diameter; however, due to space constraints, not much increase is possible. Increasing the applied current (and thus the magnetic field strength) would increase the change in column height as well; however, it would also raise the temperature even further, which is directly the second limitation of the setup.

As the temperature cannot be controlled and the electromagnet heats up quite significantly with increasing applied current, the temperature of the oil increases for increasing magnetic field strength. As shown in section 2.6 the viscosity of the MR fluid decreases with increasing temperature, which means the increase in viscosity (and thus pressure) due to the increase in magnetic field is counteracted by the decrease in viscosity (and thus pressure) due to the increase in temperature.

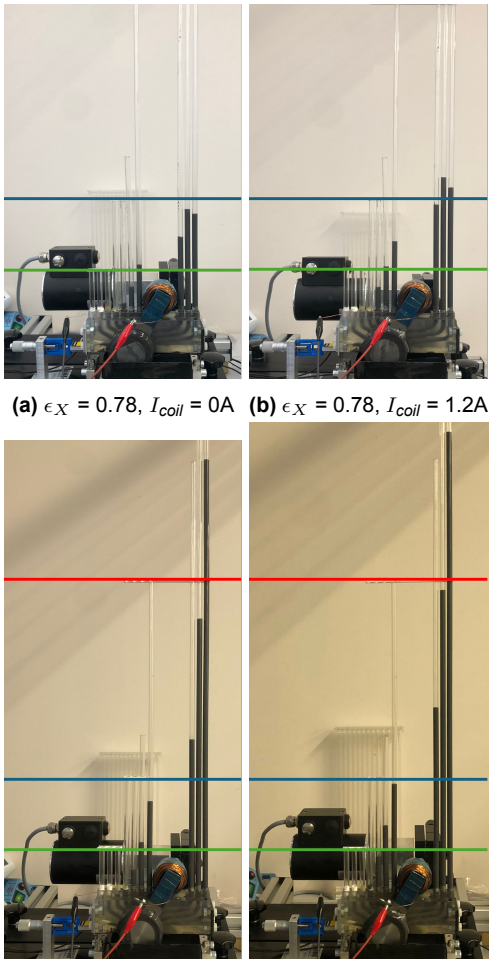

(a) ϵ_X = 0.78, I_{coil} = 0A **(b)** ϵ_X = 0.78, I_{coil} = 1.2A

(c) ϵ_X = 0.94, I_{coil} = 1.2A **(d)** ϵ_X = 0.94, I_{coil} = 1.2A

Figure 4.10: Visual comparison of the pressure distribution at ϵ_X = 0.78 and ϵ_X = 0.94 for I_{coil} = 0 and 1.2A with MR fluid lubricant. Green, red and blue lines are used as reference for the fluid column height.

4.4. Performance in relation to research objective

The research objective of this thesis was to increase the maximum load capacity for a specified minimum film thickness while not increasing the friction coefficient in the hydrodynamic lubrication regime. The hypothesis was that this is possible by changing the magnetic field strength and thus the viscosity of the MR fluid based on operating conditions such that an optimal Stribeck curve could be created.

Using the experimental results, the improved Stribeck curve can be shown by changing the applied magnetic field. In Figure 4.11, the experimentally determined Stribeck curves for different values of I_{coil} are again shown with the minimum film thickness set at 0.075mm (ϵ_X = 0.94), together with the ”optimal” Stribeck curve represented by the black line. Normally, when a lubricant is chosen, the designer is stuck with one Stribeck curve. However, using electromagnets and MR fluid, we can change the Stribeck curve during operation by changing the magnetic field strength. This means that an optimum selection of Stribeck curves can be made for different values of I_{coil}. By increasing the applied current, the Stribeck curve is moved to the left, meaning a larger maximum load capacity at the cost of higher friction coefficient as the slope of the Stribeck curve increases. However, as soon as the applied load F_{mag} on the bearing is sufficiently decreased (or equivalently, the operating velocity is increased for a constant applied load), the applied current could be decreased to transition to the next Stribeck curve, decreasing the friction coefficient. This ”ideal” Stribeck curve is displayed with the solid black line. However, because the experimental results were not perfect and tests were performed only for discrete values of applied current, the Stribeck curve shown is far from the optimal Stribeck curve that could potentially be achieved using MR fluid and electromagnets.

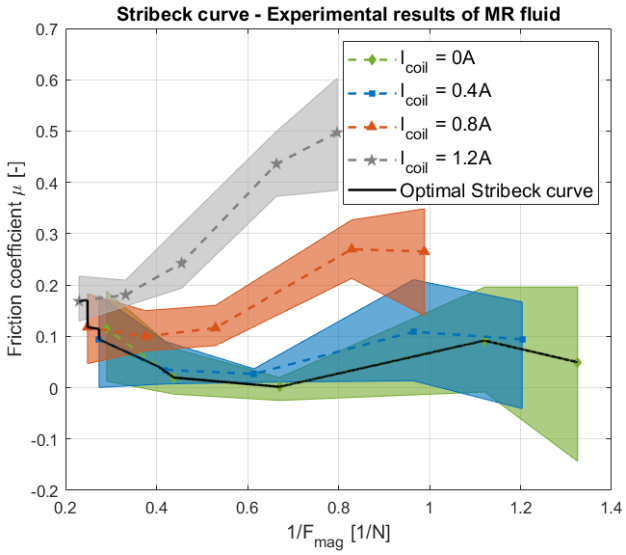

Figure 4.11: Experimental optimal Stribeck curve when I_{coil} is varied from 0 to 1.2A in steps of 0.4A.

Numerically, we can easily demonstrate how the research objective can be reached even better. In Figure 4.12 the Stribeck curves for different values of I_{coil} have been plotted. All Stribeck curves have been plotted for the same eccentricity ratio range (ϵ_X = 0.6 - 0.94), which means that the maximum load capacity is determined by a minimum set film thickness (which in a real implementation would be slightly above the film height where the bearing moves from mixed lubrication to hydrodynamic lubrication). Again, the optimal Stribeck curve for these discrete values of applied current is displayed by the solid black line. However, if we would allow for continuous values of applied current, we could create an infinite number of Stribeck curves resulting in approximately the dashed black line. Where with a normal lubricant a compromise needs to be made between maximum load capacity and performance at lower load capacity (or equivalently for a constant load: a compromise between a lower lift-off speed, the speed for which hydrodynamic lubrication occurs, and low friction coefficient at high operating velocity), MR fluid excited with electromagnet(s) can achieve both. Having the dashed black line as the Stribeck curve means that the bearing can be operated at a very low friction coefficient for small applied load while a higher load capacity can be reached by increasing the applied current.

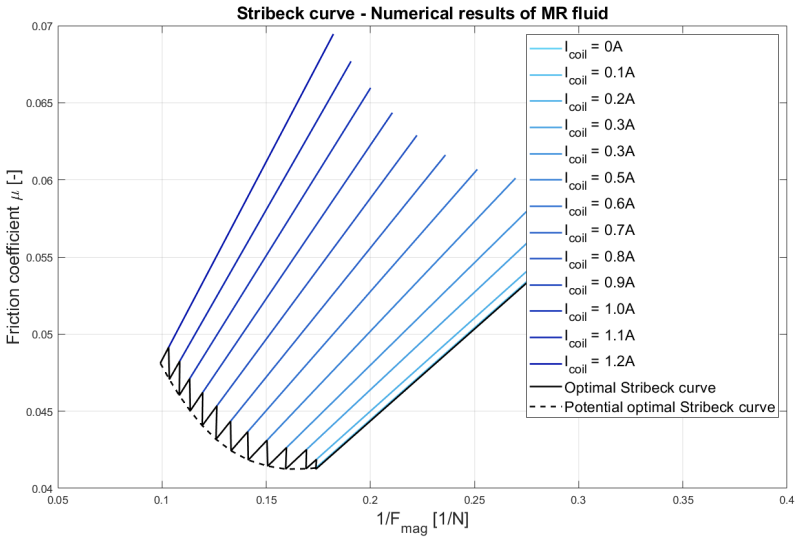

Figure 4.12: Numerical optimal Stribeck curve when I_{coil} is changed in small steps.

5 Conclusion

5.1. Conclusions

The objective of this thesis was to create a numerical model and experimental demonstrator setup to investigate the friction coefficient and load capacity of a hydrodynamic journal bearing lubricated with MR fluid for different magnetic field strengths. The goal of this model and setup was to fulfill the research objective, which was:

Increase the maximum load capacity of a hydrodynamic half journal bearing for a specified minimum film thickness, while not increasing the friction in the hydrodynamic lubrication regime using MR fluid and electromagnets.

This section summarizes the most important conclusions of this research.

- It has been shown that a relatively simple demonstrator setup can be produced which can visually show the pressure distribution in a hydrodynamic journal bearing and the effect of an applied magnetic field on the pressure distribution. The setup can be used for educational purposes as its simplicity allows for simple tests resulting in both qualitative (visual) and quantitative (generated forces and calculated pressure) results related to magnetorheological lubrication of a hydrodynamic journal bearing. However, due to slow experiments and relatively large differences between the experimental and numerical results, the performance should be improved.
- The fluid flow in a hydrodynamic journal bearing lubricated with MR fluid and controlled using electromagnet(s) can be modelled using the two dimensional Reynolds equation and a magnetic field model to simulate the generated magnetic field; however, significant differences are present between experimental and numerical results. Further improvements of the test setup are needed to investigate whether the generalized Reynolds equation needs to implemented to improve the accuracy of the model, whether the experimental results do not accurately represent the hydrodynamic forces generated in the bearing or whether the model is not an accurate representation of the experimental setup (for example due to inaccuracies in the experimental setup which are not implemented in the model).
- The current experimental setup cannot accurately determine the generated forces (especially the friction force) and also finds a very large increase in friction force with increasing magnetic field strength while the increase in load-carrying forces is small compared to the numerical model.
- The force magnitude (load-carrying capacity) of a hydrodynamic half journal bearing can be increased by applying a magnetic field to the MR fluid at the cost of an increase in friction force.
- Is has been proven both numerically and experimentally that semi-active control of a hydrodynamic journal bearing lubricated with magnetorheological fluid can increase the maximum load capacity while not increasing the friction coefficient in the hydrodynamic regime (when compared to the MR fluid without application of a magnetic field).
- The optimal Stribeck curve by means of semi-active control of the hydrodynamic journal bearing has been identified both numerically and experimentally, and with this the potential of this technology has been shown. However, the experimental setup needs to be improved to more accurately show the potential of this technology.

5.2. Recommendations for further research

The force results are somewhat comparable between the model and the experiments, but significant differences are still present. Several causes for these differences have been identified and potential improvements to the setup and model will be proposed here. The purpose of the test setup was to be simple and not as complex as the setups used in most of the literature. Furthermore, the setup should be able to serve as a demonstrator which can be used for educational purposes. Keeping that in mind, some improvements that could be made without significantly increasing complexity are as follows.

- **Improve bearing tolerances.** The tolerances of the 3D printed bearing turned out to be worse than expected. Two 2D scans of the bearing were used to compensate for this in the numerical model, but having better tolerances would decrease the uncertainty on the parameters. Using different printer settings and different post-processing steps, the tolerances could be improved. The best way to do this would be to post-process the bearing with a CNC machine. By CNC machining the bearing surface after 3D printing, a more smooth and circular bearing could be created.
- **Implement capacitive distance sensors.** One of the main causes of the differences between the model and the experiments is believed to be the uncertainty on the eccentricity ratio in the horizontal and vertical directions. By implementing capacitive distance sensors, the bearing eccentricity could be accurately measured and implemented in the model.
- **Experiments with diluted or different MR fluids.** Diluting the MR fluid results in a decrease in viscosity and therefore in a reduction in the restriction of lubricant flow into the pressure tubes. This would significantly improve the time it takes for the lubricant to reach equilibrium in the pressure tubes, improving the demonstration capabilities of the setup. However, diluting occurs at the cost of a decrease in the magnetorheological effect, decreasing the pressure increase because of a magnetic field. Another advantage of diluting the MR fluid is that the fluid would potentially become less shear-thinning. This would probably make the model more accurate, as the model currently uses the non-generalized Reynolds equation (which does not take variation in shear rate into account across the film thickness). Investigating different MR fluids (different carrier fluid, particle size, adjectives, etc.) is also possible to improve setup performance or investigate the differences in bearing performance for different fluids.
- **Temperature control.** Improvements to perform experiments at a more constant temperature can be made in two ways. First, experiments should be performed in a laboratory with a more constant temperature such that the operating conditions between subsequent measurements are more comparable (in the current experiments a temperature difference of $\sim 5°$C was observed purely due to changes in room temperature). This would ensure that the experiments are more repeatable and do not have to be adjusted for temperature. Secondly, some sort of cooling of the electromagnet would be beneficial as limiting the temperature increase of the MR fluid due to the electromagnet would ensure a larger change in generated pressure. This could be done using a heat sink or additional airflow by means of a small fan.
- **More clear bearing material.** Currently, the bearing was produced using stereolithography 3D printing with clear resin. The bearing turned out partially transparent, making it possible to see the lubricant in the pressure tubes but impossible to accurately see how far the pressure tubes were filled. By producing the bearing from a more transparent material, it would be possible to also measure the fluid height inside the bearing, making sure that the pressure can also be determined when the fluid does not reach above the bearing (measurement threshold). Consequently, the fluid weight could be more accurately implemented in calculating the vertical force and friction force, as the fluid column height would be known for all pressure tubes (and not just for the tubes where the fluid protrudes above the measurement threshold).
- **Data acquisition device with more bits.** Due to the 12 bit data acquisition device, the minimum step size in the friction force was $\sim$0.03 N. This is quite large, because the change in friction force with increasing eccentricity ratio is generally much smaller. Using a 32-bit data acquisition device would allow for measuring changes in friction force in the order of magnitude of 10^{-8}N; however, this would only work if the noise and oscillations are also greatly reduced e.g. by improving the bearing tolerances and alignment of the setup.

- **Apply a constant weight instead of prescribing the eccentricity.** This would require quite large changes to the current setup; however, this would still result in a relatively simple demonstrator setup. A schematic drawing of this setup is shown in Figure 5.1. The bearing would be put on top of the shaft and a (small) weight would be connected to it via a support frame. The mass would be placed such that the bearing is balanced and stays horizontal when the shaft is stationary. Capacitive distance sensors would be needed to measure the eccentricity, as the eccentricity is not prescribed anymore. An advantage of such a setup would be that the friction force (and increase in friction force) is made visual as the setup would rotate due to the friction force and the rotational angle is a measure for the magnitude of the friction force. A higher friction force would result in a larger bearing rotation. Another advantage is that potentially even the lift-off speed (transition speed from boundary lubrication to full-film lubrication) can be determined, although this might be difficult depending on the bearing tolerances. Also, this setup is slightly more representative for how hydrodynamic bearings are usually loaded (a purely vertical load is applied, instead of prescribing the eccentricity of the shaft). The disadvantage of this type of setup is the need for capacitive distance sensors (to measure the eccentricity). Another disadvantage is that the weight of the entire setup needs to be quite small (or the generated pressure needs to be large, but this is again limited by the length of the pressure tubes, maximum motor velocity and tolerances of the bearing) as the hydrodynamic vertical force needs to exceed the bearing setup weight, otherwise full film lubrication would not occur. Furthermore, the weight of the lubricant in the pressure tubes would again influence the friction force measurements and would still need to be accounted for. Also, it might be difficult to ensure the bearing would not move in axial direction, as it is not constrained.

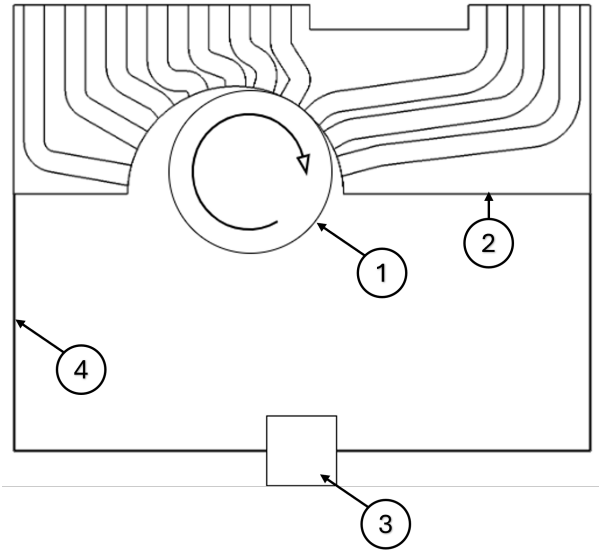

Figure 5.1: Schematic drawing of an experimental setup where a constant load is applied. 1 - Shaft, 2 - Bearing, 3 - Weight, 4 - Support frame of the weight (3).

In the numerical model, some improvements can also be made:

- **Implement the generalized Reynolds equation.** By implementing the generalized Reynolds equation, the variations in fluid properties across the film can be taken into account [15]. This is primarily important to take into account as the MR fluid is strongly shear-thinning and therefore the viscosity changes strongly across the film thickness due to the changing shear rate. In the current model, the viscosity is assumed to be constant across the film thickness based on the shear rate in the middle of the film, which is quite a large simplification. By also implementing a viscoplastic rheological model (e.g. one of the models given in Appendix D), the viscosity of the MR fluid as function of shear rate can be efficiently implemented.
- **Implement a temperature model.** The temperature of the lubricant changed strongly as a result of the implementation of the electromagnet. The temperature was measured close to the elec-

tromagnet at the side of the bearing using a thermocouple and this temperature was used when determining the viscosity of the lubricant. In reality, the temperature changes throughout the film, which can be taken into account by creating a temperature model that solves an energy equation. An additional advantage of modeling the temperature is that the increase in temperature due to the electromagnet can be modeled so that the temperature increase can also be predicted instead of only being compensated for after the experiments are performed.

In addition to improvements in the experimental setup and numerical model, the research performed with the current setup could also be extended.

- **Perform tests with a bearing without pressure tubes.** This removes uncertainty in modeling the pressure tubes but more importantly removes the uncertainty in the effect of the weight of the lubricant in the pressure tubes on the force measurements and calculation of the friction force. Furthermore, it makes testing significantly faster because it is not necessary to wait the long period of time for the lubricant to reach equilibrium in the pressure tubes. However, it does remove the visual pressure results, meaning that the setup cannot serve as a visual demonstrator anymore. To still be able to measure the pressure distribution, pressure sensors could be implemented.
- **Compare the MR fluid to a comparable hydraulic oil.** The hydraulic oil used in the experiments had a much lower viscosity compared to the MR fluid in absence of a magnetic field. Therefore, the comparison between the results with MR fluid as lubricant versus oil is not very relevant. Using a hydraulic oil with a somewhat comparable viscosity can provide a relevant comparison that shows the potential of semi-active control of a hydrodynamic bearing lubricated with MR fluid versus the performance of the bearing lubricated with a standard oil.
- **Experiments with different electromagnet angles or multiple electromagnets.** By changing the bearing slightly, the electromagnet could be mounted at different angles (locations) or even multiple electromagnets could be implemented. In this way, the optimal magnetic field distribution around the bearing can be investigated and determined, where the applied current per individual electromagnet can also be varied. This could potentially further improve the performance of the hydrodynamic bearing.
- **Investigate the implementation of tunable magnets.** Tunable magnets are magnets consisting of a combination of a permanent magnet and a coil, where the magnetic field strength is changed by momentarily applying a current [21]. The advantage of these is that the power consumption is not continuous and power only needs to be applied to change the magnetic field strength, eliminating Joule heating during operation [21]. This reduces the temperature increase of the fluid (beneficial as the viscosity will be reduced less) and reduces the power consumption of the electromagnet (improving efficiency). Tunable magnet have, to the knowledge of the author, not been applied in MR lubricated hydrodynamic bearings to date.
- **Create a full journal bearing setup.** Performing tests on a full journal bearing (instead of a half journal bearing) is a closer representation of the most actual use cases of a hydrodynamic bearing; however, this would require significant changes to the current setup as, among others, a system to supply the lubricant would need to be integrated.

Bibliography

[1] A. van Beek, *Advanced engineering design: Liftetime performance and reliability*. Delft University of Technology, 2009, ISBN: 978-90-810406-1-7.

[2] G. W. Stachowiak and A. W. Batchelor, "Hydrodynamic Lubrication," in *Engineering Tribology*, Fourth Edition, Butterworth-Heinemann, 2014, pp. 105–210, ISBN: 978-0-12-397047-3. DOI: 10.1016/B978-0-12-397047-3.00004-7.

[3] Y. Wang and Q. J. Wang, "Stribeck curves," in *Encyclopedia of Tribology*, Q. J. Wang and Y.-W. Chung, Eds. Boston, MA: Springer US, 2013, pp. 3365–3370, ISBN: 978-0-387-92897-5. DOI: 10.1007/978-0-387-92897-5_148.

[4] M. Michalec, P. Svoboda, I. Krupka, and M. Hartl, "Tribological behaviour of smart fluids influenced by magnetic and electric field – A review," *Tribology in Industry*, vol. 40, no. 4, pp. 515–528, Dec. 2018, ISSN: 03548996. DOI: 10.24874/ti.2018.40.04.01.

[5] F. Quinci, W. Litwin, M. Wodtke, and R. van den Nieuwendijk, "A comparative performance assessment of a hydrodynamic journal bearing lubricated with oil and magnetorheological fluid," *Tribology International*, vol. 162, Oct. 2021, ISSN: 0301679X. DOI: 10.1016/j.triboint.2021.107143.

[6] G. H. G. van der Meer, F. Quinci, W. Litwin, M. Wodtke, and R. A. J. van Ostayen, "Experimental comparison of the transition speed of a hydrodynamic journal bearing lubricated with oil and magnetorheological fluid," *Tribology International*, vol. 189, 2023. DOI: https://doi.org/10.1016/j.triboint.2023.108976.

[7] N. R. Fisco and H. Adeli, "Smart structures: Part I - Active and semi-active control," *Scientia Iranica*, vol. 18, no. 3, pp. 275–284, 2011, ISSN: 10263098. DOI: 10.1016/j.scient.2011.05.034.

[8] P. Mittasch, "Instruction Manual TM 260 Drive unit for tribological investigations," Tech. Rep., 2020.

[9] Gunt, "Experiment Instructions TM 260.06 Experimental Module Journal Bearing Pressure Distribution," Tech. Rep., 2011.

[10] N. Moles, "Actively controllable hydrodynamic journal bearing design using magnetorheological fluids," Ph.D. dissertation, University of Akron, 2015.

[11] H. Urreta, Z. Leicht, A. Sanchez, A. Agirre, P. Kuzhir, and G. Magnac, "Hydrodynamic bearing lubricated with magnetic fluids," in *Journal of Intelligent Material Systems and Structures*, vol. 21, Oct. 2010, pp. 1491–1499. DOI: 10.1177/1045389X09356007.

[12] Z. T. K. Phay and S. W. Oo, "Force Exerted by the Flowing Incompressible Fluid on a Pipe Bend," Tech. Rep. 1, 2022.

[13] M. Hemmatian, R. Sedaghati, and S. Rakheja, "Temperature dependency of magnetorheological fluids' properties under varying strain amplitude and rate," *Journal of Magnetism and Magnetic Materials*, vol. 498, Mar. 2020, ISSN: 03048853. DOI: 10.1016/j.jmmm.2019.166109.

[14] S. Alakhramsing, R. A. J. van Ostayen, and R. Eling, "Thermo-hydrodynamic analysis of a plain journal bearing on the basis of a new mass conserving cavitation algorithm," *Lubricants*, vol. 3, no. 2, pp. 256–280, Jun. 2015, ISSN: 20754442. DOI: 10.3390/lubricants3020256.

[15] D. Dowson, "A generalized Reynolds equation for fluid-film lubrication," *International Journal of Mechanical Sciences*, vol. 4, no. 2, pp. 159–170, 1962, ISSN: 00207403. DOI: 10.1016/S0020-7403(62)80038-1.

[16] H. Moes, *Lubrication and Beyond*. University of Twente, 2000.

[17] E. P. Furlani, *Permanent Magnet and Electromechanical Devices*. Academic press, 2001, ISBN: 978-0-12-269951-1.

[18] "COMSOL Multiphysics Reference Manual 5.5," COMSOL, Tech. Rep., 2019.

[19] J. Zheng, S. Chen, and Y. Xiao, *Effective permeability model of magnetorheological fluids and its experimental verification*, Nov. 2022. DOI: 10.1016/j.jmmm.2022.169774.

[20] The Engineering Toolbox. "Permeabiltiy." (2016), [Online]. Available: https://www.engineeringtoolbox.com/permeability-d_1923.html (visited on 06/10/2024).

[21] S. G. Viëtor, J. W. Spronck, and S. H. Hosseinnia, "Tunable Magnets: modeling and validation for dynamic and precision applications," in *Conference on Precision Mechatronics*, Sint Michielsgestel, 2018.

[22] D. Farhadi, *Compliant Mechanisms (ME46115). Week 6. Synthesis and Analysis in Compliant Mechanisms (Part II). [PowerPoint slides]*, 2022.

[23] E. C. Bingham, "PLASTICITY AND ELASTICITY," *Journal of the Franklin Institute*, vol. 197, no. 1, pp. 99–115, 1924. DOI: https://doi.org/10.1016/S0016-0032(24)90500-X.

[24] J. G. Oldroyd, “A rational formulation of the equations of plastic flow for a bingham solid,” in *Mathematical Proceedings of the Cambridge Philosophical Society*, Cambridge University Press, vol. 43, 1947, pp. 100–105.

[25] W. H. Herschel and R. Bulkley, “Konsistenzmessungen von Gummi-Benzollösungen,” *Kolloid-Zeitschrift*, vol. 39, pp. 291–300, 1926. DOI: https://doi.org/10.1007/BF01432034.

[26] N. Casson, “Flow equation for pigment-oil suspensions of the printing ink-type,” *Rheology of disperse systems*, pp. 84–104, 1959.

[27] M. Keentok, “The measurement of the yield stress of liquids,” *Rhoologica Acta Rheol. Acta*, vol. 21, pp. 325–332, 1982.

[28] G. A. Dimock, J. E. Lindler, and N. M. Wereley, “Bingham biplastic analysis of shear thinning and thickening in magnetorheological dampers,” in *Smart Structures and Materials 2000: Smart Structures and Integrated Systems*, N. M. Wereley, Ed., International Society for Optics and Photonics, vol. 3985, SPIE, 2000, pp. 444–455. DOI: 10.1117/12.388847.

[29] T. C. Papanastasiou, “Flows of materials with yield,” *Journal of rheology*, vol. 31, no. 5, pp. 385–404, 1987.

[30] A. Ghaffari, S. H. Hashemabadi, and M. Ashtiani, “A review on the simulation and modeling of magnetorheological fluids,” *Journal of Intelligent Material Systems and Structures*, vol. 26, no. 8, pp. 881–904, May 2015, ISSN: 15308138. DOI: 10.1177/1045389X14546650.

[31] K. P. Gertzos, P. G. Nikolakopoulos, and C. A. Papadopoulos, “CFD analysis of journal bearing hydrodynamic lubrication by Bingham lubricant,” *Tribology International*, vol. 41, no. 12, pp. 1190–1204, Dec. 2008, ISSN: 0301679X. DOI: 10.1016/j.triboint.2008.03.002.

[32] R. Stanway, “Smart fluids: Current and future developments,” *Materials Science and Technology*, vol. 20, no. 8, pp. 931–939, Aug. 2004, ISSN: 02670836. DOI: 10.1179/026708304225019867.

[33] A. G. Olabi and A. Grunwald, “Design and application of magneto-rheological fluid,” *Materials and Design*, vol. 28, no. 10, pp. 2658–2664, 2007, ISSN: 18734197. DOI: 10.1016/j.matdes.2006.10.009.

[34] D. A. Bompos and P. G. Nikolakopoulos, “CFD simulation of magnetorheological fluid journal bearings,” *Simulation Modelling Practice and Theory*, vol. 19, no. 4, pp. 1035–1060, Apr. 2011, ISSN: 1569190X. DOI: 10.1016/j.simpat.2011.01.001.

[35] J. Peng and K. Q. Zhu, “Effects of electric field on hydrodynamic characteristics of finite-length ER journal bearings,” *Tribology International*, vol. 39, no. 6, pp. 533–540, Jun. 2006, ISSN: 0301679X. DOI: 10.1016/j.triboint.2005.03.017.

[36] J. Rabinow, “The Magnetic Fluid Clutch,” *Transactions of the American Institute of Electrical Engineers*, vol. 67, pp. 1308–1315, 1948, ISSN: 00963860. DOI: 10.1109/T-AIEE.1948.5059821.

[37] S. W. Charles, “The preparation of magnetic fluids,” in *Ferrofluids: Magnetically Controllable Fluids and Their Applications*, S. Odenbach, Ed. Berlin, Heidelberg: Springer Berlin Heidelberg, 2002, pp. 3–18, ISBN: 978-3-540-45646-9. DOI: 10.1007/3-540-45646-5_1.

[38] M. Ashtiani, S. H. Hashemabadi, and A. Ghaffari, “A review on the magnetorheological fluid preparation and stabilization,” *Journal of Magnetism and Magnetic Materials*, vol. 374, pp. 716–730, Jan. 2015, ISSN: 03048853. DOI: 10.1016/j.jmmm.2014.09.020.

[39] J. de Vicente, D. J. Klingenberg, and R. Hidalgo-Alvarez, “Magnetorheological fluids: A review,” *Soft Matter*, vol. 7, no. 8, pp. 3701–3710, Apr. 2011, ISSN: 1744683X. DOI: 10.1039/c0sm01221a.

[40] K. van der Wal, R. A. J. van Ostayen, and S. G. E. Lampaert, “Ferrofluid rotary seal with replenishment system for sealing liquids,” *Tribology International*, vol. 150, Oct. 2020, ISSN: 0301679X. DOI: 10.1016/j.triboint.2020.106372.

[41] K. Raj and R. Moskowitz, “COMMERCIAL APPLICATIONS OF FERROFLUIDS,” *Journal of Magnetism and Magnetic Materials*, vol. 85, pp. 233–245, 1990.

[42] K. Raj, B. Moskowitz, and R. Casciari, “Advances in ferrofluid technology,” *Journal of Magnetism and Magnetic Materials*, vol. 149, pp. 174–180, 1995.

[43] S. G. E. Lampaert, *Planar Ferrofluid Bearings Modelling and Design Principles (MSc thesis)*. 2015.

[44] S. G. E. Lampaert, J. W. Spronck, and R. A. J. van Ostayen, “Load and stiffness of a planar ferrofluid pocket bearing,” *Proceedings of the Institution of Mechanical Engineers, Part J: Journal of Engineering Tribology*, vol. 232, no. 1, pp. 14–25, Jan. 2018, ISSN: 2041305X. DOI: 10.1177/1350650117739200.

[45] S. G. E. Lampaert, B. J. Fellinger, J. W. Spronck, and R. A. J. van Ostayen, “In-plane friction behaviour of a ferrofluid bearing,” *Precision Engineering*, vol. 54, pp. 163–170, Oct. 2018, ISSN: 01416359. DOI: 10.1016/j.precisioneng.2018.05.013.

[46] A. S. Boots, L. E. Krijgsman, B. J. M. de Ruiter, S. G. E. Lampaert, and J. W. Spronck, “Increasing the load capacity of planar ferrofluid bearings by the addition of ferromagnetic material,” *Tribology International*, vol. 129, pp. 46–54, Jan. 2019, ISSN: 0301679X. DOI: 10.1016/j.triboint.2018.07.048.

[47] A. S. T. Boots, J. W. Spronck, R. A. J. Van Ostayen, and S. G. E. Lampaert, “Operational range of a ferrofluid pocket bearing,” *Smart Materials and Structures*, vol. 28, no. 11, Oct. 2019, ISSN: 1361665X. DOI: 10.1088/1361-665X/ab2b60.

[48] C. A. Laukiavich, M. J. Braun, and A. J. Chandy, “A comparison between the performance of ferro- and magnetorheological fluids in a hydrodynamic bearing,” *Proceedings of the Institution of Mechanical Engineers, Part J: Journal of Engineering Tribology*, vol. 228, no. 6, pp. 649–666, 2014, ISSN: 2041305X. DOI: 10.1177/1350650114523753.

[49] S. Kumar, R. Sehgal, M. F. Wani, and M. D. Sharma, “Stabilization and tribological properties of magnetorheological (MR) fluids: A review,” *Journal of Magnetism and Magnetic Materials*, vol. 538, Nov. 2021, ISSN: 03048853. DOI: 10.1016/j.jmmm.2021.168295.

[50] J. Carlson, D. Catanzarite, and K. St. Clair, “Commercial magneto-rheological fluid devices,” *International Journal of Modern Physics B*, vol. 10, no. 23n24, pp. 2857–2865, 1996. DOI: 10.1142/S0217979296001306.

[51] X. Z. Zhang, X. L. Gong, P. Q. Zhang, and Q. M. Wang, “Study on the mechanism of the squeeze-strengthen effect in magnetorheological fluids,” *Journal of Applied Physics*, vol. 96, no. 4, pp. 2359–2364, Aug. 2004, ISSN: 00218979. DOI: 10.1063/1.1773379.

[52] G. Bossis, O. Volkova, S. Lacis, and A. Meunier, “Magnetorheology: Fluids, structures and rheology,” in *Ferrofluids: Magnetically Controllable Fluids and Their Applications*, S. Odenbach, Ed. Berlin, Heidelberg: Springer Berlin Heidelberg, 2002, pp. 202–230, ISBN: 978-3-540-45646-9. DOI: 10.1007/3-540-45646-5_11.

[53] J. de Gans, H. Hoekstra, and J. Mellema, “Non-linear magnetorheological behaviour of an inverse ferrofluid,” *Faraday Discuss*, vol. 112, pp. 209–224, 1999.

[54] D. J. Klingenberg, J. C. Ulicny, and M. A. Golden, “Mason numbers for magnetorheology,” *Journal of Rheology*, vol. 51, no. 5, pp. 883–893, Sep. 2007, ISSN: 0148-6055. DOI: 10.1122/1.2764089.

[55] G. R. Iglesias, M. T. López-López, J. D. Durán, F. González-Caballero, and A. V. Delgado, “Dynamic characterization of extremely bidisperse magnetorheological fluids,” *Journal of Colloid and Interface Science*, vol. 377, no. 1, pp. 153–159, Jul. 2012, ISSN: 00219797. DOI: 10.1016/j.jcis.2012.03.077.

[56] J. S. Choi, B. J. Park, M. S. Cho, and H. J. Choi, “Preparation and magnetorheological characteristics of polymer coated carbonyl iron suspensions,” *Journal of Magnetism and Magnetic Materials*, vol. 304, no. 1, Sep. 2006, ISSN: 03048853. DOI: 10.1016/j.jmmm.2006.02.055.

[57] B. D. Chin, J. H. Park, M. H. Kwon, and O. O. Park, “Rheological properties and dispersion stability of magnetorheological (MR) suspensions,” *Rheologica Acta*, vol. 40, no. 3, pp. 211–219, 2001. DOI: 10.1007/s003970000150.

[58] K. H. Song, B. J. Park, and H. J. Choi, “Effect of magnetic nanoparticle additive on characteristics of magnetorheological fluid,” *IEEE Transactions on Magnetics*, vol. 45, no. 10, pp. 4045–4048, 2009, ISSN: 00189464. DOI: 10.1109/TMAG.2009.2025390.

[59] G. T. Ngatu, N. M. Wereley, J. O. Karli, and R. C. Bell, “Dimorphic magnetorheological fluids: Exploiting partial substitution of microspheres by nanowires,” *Smart Materials and Structures*, vol. 17, no. 4, Aug. 2008, ISSN: 09641726. DOI: 10.1088/0964-1726/17/4/045022.

[60] W. Jiang, Y. Zhang, S. Xuan, C. Guo, and X. Gong, “Dimorphic magnetorheological fluid with improved rheological properties,” *Journal of Magnetism and Magnetic Materials*, vol. 323, no. 24, pp. 3246–3250, Dec. 2011, ISSN: 03048853. DOI: 10.1016/j.jmmm.2011.07.024.

[61] J. Y. Lee, S. H. Kwon, and H. J. Choi, “Magnetorheological characteristics of carbonyl iron microparticles with different shapes,” *Korea Australia Rheology Journal*, vol. 31, no. 1, pp. 41–47, Feb. 2019, ISSN: 20937660. DOI: 10.1007/s13367-019-0005-6.

[62] G. Wang, Y. Ma, G. Cui, N. Li, and X. Dong, “Two-dimensional Fe3O4/MoS2 nanocomposites for a magnetorheological fluid with enhanced sedimentation stability,” *Soft Matter*, vol. 14, no. 10, pp. 1917–1924, 2018, ISSN: 17446848. DOI: 10.1039/c7sm02425h.

[63] M. S. Kim, Y. D. Liu, B. J. Park, C. Y. You, and H. J. Choi, “Carbonyl iron particles dispersed in a polymer solution and their rheological characteristics under applied magnetic field,” *Journal of Industrial and Engineering Chemistry*, vol. 18, no. 2, pp. 664–667, Mar. 2012, ISSN: 1226086X. DOI: 10.1016/j.jiec.2011.11.062.

[64] S. T. Lim, M. S. Cho, I. B. Jang, H. J. Choi, and M. S. Jhon, “Magnetorheology of carbonyl-iron suspensions with submicron-sized filler,” *IEEE Transactions on Magnetics*, vol. 40, no. 4 II, pp. 3033–3035, 2004, ISSN: 00189464. DOI: 10.1109/TMAG.2004.830400.

[65] S. T. Lim, M. S. Cho, I. B. Jang, and H. J. Choi, “Magnetorheological characterization of carbonyl iron based suspension stabilized by fumed silica,” *Journal of Magnetism and Magnetic Materials*, vol. 282, pp. 170–173, Nov. 2004, ISSN: 03048853. DOI: 10.1016/j.jmmm.2004.04.040.

[66] J. Svoboda, *Magnetic Techniques for the Treatment of Materials*. Springer, 2004, ISBN: 1-4020-2107-0.

[67] S. K. Baik, D. W. Ha, J. M. Kwon, Y. J. Lee, and R. K. Ko, "Magnetic force on a magnetic particle within a high gradient magnetic separator," *Physica C: Superconductivity and its Applications*, vol. 484, pp. 333–337, Jan. 2013, ISSN: 09214534. DOI: 10.1016/j.physc.2012.03.033.

[68] T. B. Jones, *Electromechanics of particles*. Cambridge University Press, 1995.

[69] A. Rodriguez-Barroso, G. Camacho, O. Martinez-Cano, J. Rafael Morillas, and J. de Vicente, "Magnetophoretic force and homogeneity optimization in multiplexed magnetic tweezers for microrheometry applications," *Measurement: Journal of the International Measurement Confederation*, vol. 222, Nov. 2023, ISSN: 02632241. DOI: 10.1016/j.measurement.2023.113552.

[70] M. C. de Graaf, *A new concept in bearing technology: Magnetorheological texturing (MSc thesis)*. 2019.

[71] J. D. Carlson, "What makes a good MR fluid?" *Journal of Intelligent Material Systems and Structures*, vol. 13, no. 7-8, pp. 431–435, 2002, ISSN: 1045389X. DOI: 10.1106/104538902028221.

[72] S. R. Sunkara, T. W. Root, J. C. Ulicny, and D. J. Klingenberg, "Iron oxidation and its impact on MR behavior," *Journal of Physics: Conference Series*, vol. 149, p. 012 081, Feb. 2009. DOI: 10.1088/1742-6596/149/1/012081.

[73] J. Frene, D. Nicolas, B. Degueurce, D. Berthe, and M. Godet, *Hydrodynamic lubrication: bearings and thrust bearings*. Elsevier, 1997.

[74] R. Stribeck, "Die wesentlichen eigenschaften der gleit-und rollenlager," *Zeitschrift des Vereines Deutscher Ingenieure*, vol. 46, pp. 1341–1348, 1902.

[75] M. D. Hersey, "The laws of lubrication of horizontal journal bearings," *Journal of the Washington Academy of Sciences*, vol. 4, no. 19, pp. 542–552, 1914.

[76] M. J. Braun and W. M. Hannon, "Cavitation formation and modelling for fluid film bearings: A review," *Proceedings of the Institution of Mechanical Engineers, Part J: Journal of Engineering Tribology*, vol. 224, no. 9, pp. 839–863, Jan. 2010, ISSN: 13506501. DOI: 10.1243/13506501JET772.

[77] F. J. Profito and S. Paulo, "On the Development of Advanced Techniques for Mixed-Elastohydrodynamic Lubrication Modelling of Journal and Sliding Bearing Systems," Tech. Rep., 2015.

[78] D. Dowson and C. M. Taylor, "CAVITATION IN BEARINGS," *Annual Review of Fluid Mechanics*, vol. 11, no. 1, pp. 35–66, 1979.

[79] A. Farjoud, N. Vahdati, and Y. F. Fah, "Mathematical model of drum-type MR brakes using herschel-bulkley shear model," *Journal of Intelligent Material Systems and Structures*, vol. 19, no. 5, pp. 565–572, May 2008, ISSN: 1045389X. DOI: 10.1177/1045389X07077851.

[80] M. I. Varela-Jiménez, J. L. Vargas Luna, J. A. Cortés-Ramírez, and G. Song, "Constitutive model for shear yield stress of magnetorheological fluid based on the concept of state transition," *Smart Materials and Structures*, vol. 24, no. 4, Apr. 2015, ISSN: 1361665X. DOI: 10.1088/0964-1726/24/4/045039.

[81] H. W. Swift, "THE STABILITY OF LUBRICATING FILMS IN JOURNAL BEARINGS.," in *Minutes of the Proceedings of the Institution of Civil Engineers*, 1932, pp. 267–288.

[82] W. Stieber, "Das schwimmlager: Hydrodynamische theorie des gleitlagers," Tech. Rep., 1933.

[83] H. G. Elrod, "A Cavitation Algorithm," *Journal of Lubrication Technology*, vol. 103, no. 3, pp. 350–354, 1981. DOI: 10.1115/1.3251669.

[84] D. Vijayaraghavan and T. G. Keith, "Development and evaluation of a cavitation algorithm," *Tribology Transactions*, vol. 32, no. 2, pp. 225–233, 1989, ISSN: 1547397X. DOI: 10.1080/10402008908981882.

[85] D. Vijayaraghavan and T. G. Keith, "An Efficient, Robust, and Time Accurate Numerical Scheme Applied to a Cavitation Algorithm," *Journal of Tribology*, vol. 112, no. 1, pp. 44–51, 1990. DOI: 10.1115/1.2920229.

[86] T. Woloszynski, P. Podsiadlo, and G. W. Stachowiak, "Efficient Solution to the Cavitation Problem in Hydrodynamic Lubrication," *Tribology Letters*, vol. 58, no. 1, 2015, ISSN: 10238883. DOI: 10.1007/s11249-015-0487-4.

[87] D. Gropper, L. Wang, and T. J. Harvey, "Hydrodynamic lubrication of textured surfaces: A review of modeling techniques and key findings," *Tribology International*, vol. 94, pp. 509–529, Feb. 2016, ISSN: 0301679X. DOI: 10.1016/j.triboint.2015.10.009.

[88] L. Gumbel, "Das problem der lagerreibung," *Mbl. Berlin. Bez. Ver. dtsch. Ing*, vol. 5, pp. 87–104, 1914.

[89] F. White, *Fluid Mechanics*, 7th. New York, N.Y.: McGraw Hill, 2011, ISBN: 9780077422417.

[90] R. L. Batra, "RHEODYNAMIC LUBRICATION OF A JOURNAL BEARING," *Appl. sci. Res.*, vol. 15, pp. 331–344, 1966. DOI: https://doi.org/10.1007/BF00411567.

[91] S. Wada, H. Hayashi, and K. Haga, "Behavior of a Bingham Solid in Hydrodynamic Lubrication : Part 1, General Theory," *Bulletin of JSME*, vol. 16, no. 92, pp. 422–431, 1973. DOI: 10.1299/jsme1958.16.422.

[92] S. Wada, H. Hayashi, and K. Haga, "Behavior of a Bingham Solid in Hydrodynamic Lubrication : Part 3, Application to Journal Bearing," *Bulletin of JSME*, vol. 17, no. 111, pp. 1182–1191, 1974. DOI: 10.1299/jsme1958.16.422.

[93] C. Dorier and J. Tichy, “Behavior of a Bingham-like viscous fluid in lubrication flows,” *Journal of Non-Newtonian Fluid Mechanics*, vol. 45, pp. 291–310, 1992.

[94] S. G. E. Lampaert and R. A. J. van Ostayen, “Lubrication theory for Bingham plastics,” *Tribology International*, vol. 147, Jul. 2020, ISSN: 0301679X. DOI: 10.1016/j.triboint.2020.106160.

[95] J. A. Tichy, “Hydrodynamic lubrication theory for the Bingham plastic flow model,” *Journal of Rheology*, vol. 35, no. 4, pp. 447–496, 1991. DOI: 10.1122/1.550231.

[96] A. Babin, A. Fetisov, and V. Tyurin, “Numerical Modelling of Fluid-Film Bearing Lubricated with Magnetorheological Fluid,” in *Proceedings of the 5th International Conference on Industrial Engineering (ICIE 2019)*, Springer International Publishing, 2020, pp. 1303–1310, ISBN: 9783030220402. DOI: 10.1007/978-3-030-22041-9{_}136.

[97] T. A. Osman, G. S. Nada, and Z. S. Safar, “Effect of using current-carrying-wire models in the design of hydrodynamic journal bearings lubricated with ferrofluid,” *Tribology Letters*, vol. 11, no. 1, pp. 61–70, 2001.

[98] H. Montazeri, “Numerical analysis of hydrodynamic journal bearings lubricated with ferrofluid,” *Proceedings of the Institution of Mechanical Engineers, Part J: Journal of Engineering Tribology*, vol. 222, no. 1, pp. 51–60, Feb. 2008, ISSN: 13506501. DOI: 10.1243/13506501JET314.

[99] T. A. Osman, G. S. Nada, and Z. S. Safar, “Static and dynamic characteristics of magnetized journal bearings lubricated with ferrofluid,” Tech. Rep., 2001, pp. 369–380.

[100] T. A. Osman, G. S. Nada, and Z. S. Safar, “Different magnetic models in the design of hydrodynamic journal bearings lubricated with non-Newtonian ferrofluid,” *Tribology Letters*, vol. 14, pp. 211–223, 2003. DOI: https://doi.org/10.1023/A:1022869432202.

[101] J. Zapoměl and P. Ferfecki, “A new concept of a hydrodynamic bearing lubricated by composite magnetic fluid for controlling the bearing load capacity,” *Mechanical Systems and Signal Processing*, vol. 168, Apr. 2022, ISSN: 10961216. DOI: 10.1016/j.ymssp.2021.108678.

[102] J. Zapoměl and P. Ferfecki, “The influence of ferromagnetic fluids on performance of hydrodynamic bearings,” *Vibroengineering Procedia*, vol. 27, pp. 133–138, Sep. 2019, ISSN: 23450533. DOI: 10.21595/vp.2019.20950.

[103] J. Zapoměl and P. Ferfecki, “Vibration control of rotors mounted in hydrodynamic bearings lubricated with magnetically sensitive oil by changing their load capacity,” *Bulletin of the Polish Academy of Sciences: Technical Sciences*, vol. 69, no. 6, 2021, ISSN: 23001917. DOI: 10.24425/bpasts.2021.137988.

[104] J. Zapoměl, P. Ferfecki, and J. Kozánek, “Avoiding disc collisions and nonlinear vibration of unbalanced rotors by means of position control of the rotor journal mounted in magnetorheological hydrodynamic bearings,” *International Journal of Non-Linear Mechanics*, vol. 151, May 2023, ISSN: 00207462. DOI: 10.1016/j.ijnonlinmec.2023.104378.

[105] L. Peng, D. Hua, X. Liu, D. Andriukaitis, G. Królczyk, and Z. Li, “Research on control strategy of an active magnetorheological fluid bearing based on improved gray wolf optimization approach,” *Journal of Low Frequency Noise Vibration and Active Control*, 2023, ISSN: 20484046. DOI: 10.1177/14613484231186695.

[106] D. A. Bompos and P. G. Nikolakopoulos, “Journal bearing stiffness and damping coefficients using nanomagnetorheological fluids and stability analysis,” *Journal of Tribology*, vol. 136, no. 4, 2014, ISSN: 15288897. DOI: 10.1115/1.4027748.

[107] X. Wang, H. Li, M. Li, H. Bai, G. Meng, and H. Zhang, “Dynamic characteristics of magnetorheological fluid lubricated journal bearing and its application to rotor vibration control,” *Journal of Vibroengineering*, vol. 17, no. 4, pp. 1912–1928, 2015, ISSN: 1392-8716.

[108] X. Wang, H. Li, W. Lu, and G. Meng, “Stiffness and Damping Properties of (Semi) Floating Ring Bearing Using Magnetorheological Fluids as Lubricant,” *Journal of Tribology*, vol. 139, no. 5, pp. 1–14, Sep. 2017, ISSN: 15288897. DOI: 10.1115/1.4035773.

[109] A. K. Bhat, N. Vaz, Y. Kumar, R. D’Silva, P. Kumar, and K. G. Binu, “Comparative study of journal bearing performance with ferrofluid and MR fluid as lubricant,” in *AIP Conference Proceedings*, vol. 2080, American Institute of Physics Inc., Mar. 2019, ISBN: 9780735418103. DOI: 10.1063/1.5092926.

[110] N. Vaz *et al.*, “Experimental Investigation of Frictional Force in a Hydrodynamic Journal Bearing Lubricated with Magnetorheological Fluid,” *Journal of Mechanical Engineering and Automation*, vol. 7, no. 5, pp. 131–134, 2017. DOI: 10.5923/j.jmea.20170705.01.

[111] S. Zhang, Z. Long, and X. Yang, “Lubrication performance of magnetorheological fluid-lubricated rubber stern bearing test ring,” *Journal of the Brazilian Society of Mechanical Sciences and Engineering*, vol. 43, no. 1, Jan. 2021, ISSN: 18063691. DOI: 10.1007/s40430-020-02796-3.

[112] D. A. Bompos and P. G. Nikolakopoulos, “Experimental and Analytical Investigations of Dynamic Characteristics of Magnetorheological and Nanomagnetorheological Fluid Film Journal Bearing,” *Journal of Vibration and Acoustics*, vol. 138, no. 3, Jun. 2016, ISSN: 15288927. DOI: 10.1115/1.4032900.

[113] X. Wang, H. Li, and G. Meng, "Rotordynamic coefficients of a controllable magnetorheological fluid lubricated floating ring bearing," *Tribology International*, vol. 114, pp. 1–14, 2017, ISSN: 0301679X. DOI: 10.1016/j.triboint.2017.04.002.

[114] K. Sahu and S. C. Sharma, "A Simulation Study on the Behavior of Magnetorheological Fluid on Herringbone-Grooved Hybrid Slot-Entry Bearing," *Tribology Transactions*, vol. 62, no. 6, pp. 1099–1118, Nov. 2019, ISSN: 1547397X. DOI: 10.1080/10402004.2019.1649775.

[115] K. Sahu, S. C. Sharma, and N. Ram, "Misalignment and Surface Irregularities Effect in MR Fluid Journal Bearing," *International Journal of Mechanical Sciences*, vol. 221, May 2022, ISSN: 00207403. DOI: 10.1016/j.ijmecsci.2022.107196.

[116] S. C. Sharma and A. Kumar, "On the behaviour of roughened conical hybrid journal bearing system operating with MR lubricant," *Tribology International*, vol. 156, Apr. 2021, ISSN: 0301679X. DOI: 10.1016/j.triboint.2020.106824.

[117] K. Sahu, S. C. Sharma, and A. K. Tomar, "Analysis of MR fluid lubricated slot entry hybrid conical journal bearing with texturing arrangements," *Tribology International*, vol. 188, Oct. 2023, ISSN: 0301679X. DOI: 10.1016/j.triboint.2023.108788.

[118] S. C. Sharma and A. K. Tomar, "Study on MR fluid hybrid hole-entry spherical journal bearing with micro-grooves," *International Journal of Mechanical Sciences*, vol. 202-203, Jul. 2021, ISSN: 00207403. DOI: 10.1016/j.ijmecsci.2021.106504.

[119] S. C. Sharma and N. Agrawal, "Performance of a Spherical Hybrid Thrust Bearing Considering the Influence of Surface Irregularities and MR Lubricant Behavior," *Tribology Transactions*, vol. 65, no. 3, pp. 457–478, 2022, ISSN: 1547397X. DOI: 10.1080/10402004.2022.2050967.

[120] A. K. Tomar, S. C. Sharma, and K. Sahu, "Performance analysis of textured spherical hybrid journal bearings operated with magneto-rheological fluid," *Journal of Tribology*, pp. 1–24, Sep. 2023, ISSN: 0742-4787. DOI: 10.1115/1.4063495.

[121] H. Urreta, G. Aguirre, P. Kuzhir, and L. N. Lopez de Lacalle, "Actively lubricated hybrid journal bearings based on magnetic fluids for high-precision spindles of machine tools," *Journal of Intelligent Material Systems and Structures*, vol. 30, no. 15, pp. 2257–2271, Sep. 2019, ISSN: 15308138. DOI: 10.1177/1045389X19862358.

[122] S. G. E. Lampaert, F. Quinci, and R. A. J. van Ostayen, "Rheological texture in a journal bearing with magnetorheological fluids," *Journal of Magnetism and Magnetic Materials*, vol. 499, Apr. 2020, ISSN: 03048853. DOI: 10.1016/j.jmmm.2019.166218.

[123] S. G. E. Lampaert and R. A. J. van Ostayen, "Virtual textured hybrid bearings," in *Proceedings of the 44th Leeds-Lyon symposium on tribology, Lyon*, 2017, pp. 4–6.

[124] G. H. G. van der Meer, *Modelling self-healing magnetic textures in hydrodynamic bearings (MSc thesis)*. 2020.

[125] B. J. W. Lucieer, *Experimental investigation of self-healing magnetorheological surface textures (MSc thesis)*. 2020.

[126] T. L. van Kuik, *The transition from structures to textures in magnetorheological fluids (MSc thesis)*. 2022.

[127] M. Rahman, Z. C. Ong, S. Julai, M. M. Ferdaus, and R. Ahamed, "A review of advances in magnetorheological dampers: their design optimization and applications," *Journal of Zhejiang University: Science A*, vol. 18, no. 12, pp. 991–1010, Dec. 2017, ISSN: 18621775. DOI: 10.1631/jzus.A1600721.

[128] J. D. Carlson, D. M. Catanzarite, and K. St. Clair, "Commercial Magneto-Rheological Fluid Devices," *International Journal of Modern Physics B*, vol. 10, no. 23-24, pp. 2857–2865, 1996. DOI: 10.1142/S0217979296001306.

[129] X. Zhu, X. Jing, and L. Cheng, *Magnetorheological fluid dampers: A review on structure design and analysis*, May 2012. DOI: 10.1177/1045389X12436735.

[130] J. Hesselbach and C. Abel-Keilhack, "Active hydrostatic bearing with magnetorheological fluid," *Journal of Applied Physics*, vol. 93, no. 10, pp. 8441–8443, May 2003, ISSN: 00218979. DOI: 10.1063/1.1555850.

[131] J. M. Guldbakke and J. Hesselbach, "Development of bearings and a damper based on magnetically controllable fluids," *Journal of Physics Condensed Matter*, vol. 18, no. 38, Sep. 2006, ISSN: 09538984. DOI: 10.1088/0953-8984/18/38/S29.

[132] S. G. E. Lampaert and R. A. J. van Ostayen, "Experimental results on a hydrostatic bearing lubricated with a magnetorheological fluid," *Current Applied Physics*, vol. 19, no. 12, pp. 1441–1448, Dec. 2019, ISSN: 15671739. DOI: 10.1016/j.cap.2019.09.004.

[133] J. Peng and K. E. Zhu, "Hydrodynamic characteristics of ER journal bearings with external electric field imposed on the contractive part," *Journal of Intelligent Material Systems and Structures*, vol. 16, no. 6, pp. 493–499, Jun. 2005, ISSN: 1045389X. DOI: 10.1177/1045389X05052312.

[134] K.-Q. Zhu and J. Peng, "HYDRODYNAMIC CHARACTERISTICS OF ER FLUID FLOWS IN JOURNAL BEARINGS," Tech. Rep., 2003, pp. 205–208.

[135] T. H. Leek, S. Lingard, R. J. Atkin, and W. A. Bullough, “An experimental investigation of the flow of an electro-rheological fluid in a Rayleigh step bearing,” *Journal of PHysics D: Applied Physics*, vol. 26, pp. 1592–1600, 1993.

[136] Y. B. Lee, “Behavior analysis of controllable electrorheology fluid plain journal bearings,” *Journal of Dynamic Systems, Measurement and Control, Transactions of the ASME*, vol. 137, no. 6, Jun. 2015, ISSN: 15289028. DOI: 10.1115/1.4029369.

[137] A. D. Dimarogonas and A. Kollias, “Electrorheological fluid-controlled “smart” journal bearings,” *Tribology Transactions*, vol. 35, no. 4, pp. 611–618, 1992, ISSN: 1547397X. DOI: 10.1080/10402009208982163.

[138] P. G. Nikolakopoulos and C. A. Papadopoulos, “Controllable high speed journal bearings, lubricated with electro-rheological fluids. An analytical and experimental approach,” *Tribology International*, vol. 31, no. 5, pp. 225–234, 1998.

[139] S. Jang and J. A. Tichy, “Internal damper characteristics of rotor system with submerged ER fluid journal bearing,” *International Journal of Rotating Machinery*, vol. 3, no. 1, pp. 61–71, 1997, ISSN: 15423034. DOI: 10.1155/S1023621X97000079.

[140] P. G. Nikolakopoulos and C. A. Papadopoulos, “Controllable Misaligned Journal Bearings, Lubricated with Smart Fluids,” *Journal of Intelligent Material Systems and Structures*, vol. 8, 1997.

[141] A. K. Tomar and S. C. Sharma, “A Study of Hole-Entry Grooved Surface Hybrid Spherical Journal Bearing Operating with Electrorheological Lubricant,” *Journal of Tribology*, vol. 142, no. 11, Nov. 2020, ISSN: 15288897. DOI: 10.1115/1.4047298.

[142] S. C. Sharma and N. Kumar, “Performance of electro-rheological (ER) lubricant operated hybrid circular thrust pad bearing considering 3D surface irregularities,” *Tribology International*, vol. 185, Jul. 2023, ISSN: 0301679X. DOI: 10.1016/j.triboint.2023.108554.

[143] K. Sahu, S. C. Sharma, and A. K. Tomar, “Effect of bearing shell deformation and ER fluid behavior on two-lobed slot-entry hybrid journal bearing,” *Proceedings of the Institution of Mechanical Engineers, Part J: Journal of Engineering Tribology*, Nov. 2023, ISSN: 1350-6501. DOI: 10.1177/13506501231213774.

[144] S. Kumar, V. Kumar, and A. K. Singh, “Dynamic performance analysis of ER fluid lubricated journal bearing,” in *AIP Conference Proceedings*, vol. 2357, American Institute of Physics Inc., May 2022, ISBN: 9780735441897. DOI: 10.1063/5.0080603.

[145] A. Kumar and S. C. Sharma, “Textured conical hybrid journal bearing with ER lubricant behavior,” *Tribology International*, vol. 129, pp. 363–376, Jan. 2019, ISSN: 0301679X. DOI: 10.1016/j.triboint.2018.08.040.

[146] C. B. Khatri and S. C. Sharma, “Analysis of textured multi-lobe non-recessed hybrid journal bearings with various restrictors,” *International Journal of Mechanical Sciences*, vol. 145, pp. 258–286, Sep. 2018, ISSN: 00207403. DOI: 10.1016/j.ijmecsci.2018.07.014.

[147] S. C. Sharma and C. B. Khatri, “Performance of textured 3-lobe slot-entry hybrid journal bearing system operating with electro-rheological (ER) lubricant,” in *73rd Society of Tribologists and Lubrication Engineers Annual Meeting and Exhibition 2018*, 2018, pp. 268–270.

[148] J. S. Basavaraja, S. C. Sharma, and S. C. Jain, “A study of misaligned electrorheological fluid lubricated hole-entry hybrid journal bearing,” *Tribology International*, vol. 43, pp. 1059–1064, May 2010, ISSN: 0301679X. DOI: 10.1016/j.triboint.2009.12.052.

A

Leaf springs sizing

As the leaf springs were shortened due to the implementation of the load cells, the stiffness would increase. To ensure that the horizontal force was of a comparable order of magnitude as for the original setup, the thickness of the leaf springs was decreased. Based on a Pseudo Rigid-Body Model (PRBM) of a large-length flexure, the stiffness of the original springs and shortened springs was determined. As the bearing is supported by four leaf springs, the angle of the leaf springs with respect to the ground and bearing remains at 90° meaning a fixed-guided boundary condition for the PRBM should be used (see Figure A.1).

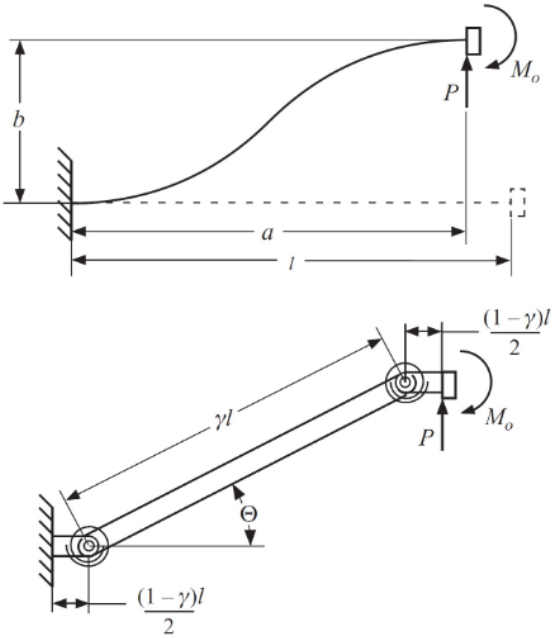

Figure A.1: Schematic drawings with parameter definitions for a large-length flexure with a fixed-guided boundary condition. Taken from [22].

The force needed for a displacement of angle Θ is given in Equation A.1 [22], where P is the force, K_Θ = 2.65, E is the E-modulus of the leaf spring material, I is the moment of inertia of the leaf spring and l is the length of the flexure (measured from the edge of the attachment holes, as this is the effective length that can deform). The relation between linear displacement x (in the direction of force P) and displacement angle Θ is given in Equation A.2, where γ = 0.8517.

$$P = \frac{4K_\Theta EI\Theta}{l^2 \cos\Theta} \tag{A.1}$$

$$x = \sin(\Theta)\gamma l \tag{A.2}$$

By multiplying the calculated force P for a specific linear displacement x by 4 (since there are four leaf springs) and subsequently dividing by the linear displacement x, the combined stiffness of the four leaf springs was calculated. The calculated stiffness of the original leaf springs and the new (short) leaf springs for three different thicknesses is given in Table A.1. A thickness of 0.3mm would result in a stiffness closest to the stiffness of the original leaf springs. A smaller thickness results in a lower stiffness and thus a smaller horizontal force, which is beneficial as the horizontal force on the vertical load cells is reduced. However, making the leaf springs too thin results in large vibrations in the system. More importantly, the horizontal force needs to be larger than the horizontal hydrodynamic force during experiments, as otherwise the bearing would lose contact with the micrometer screw (and the eccentricity ratio would become unknown). For this reason, leaf springs with a thickness of 0.25mm were selected, as they provided sufficient stiffness to overcome the hydrodynamic forces encountered during the experiments while limiting the horizontal force. The stiffness was not experimentally validated as these calculations were just done to initially design and size the leaf springs and during experiments the horizontal force due to deformation of the leaf springs was found to be sufficient (larger than the generated hydrodynamic horizontal force).

Leaf spring	l [mm]	Thickness [mm]	Stiffness [N/mm]
Original	46.1	0.5	12
New	27.05	0.3	12.9
	27.05	0.25	7.5
	27.05	0.2	3.8

Table A.1: Stiffness of the leaf spring for different dimensions.

B

Compliant joint effects

To minimize the friction force at the interface between the micrometer screw and the bearing, two mitigating methods were attempted: pushing against the bearing by hand during operation and implementing a compliant joint. The effectiveness of both methods and the impact of the finite stiffness of the compliant joint (and therefore the higher eccentricity as the bearing displacement is smaller than the micrometer screw displacement) are analyzed in section B.1 and section B.2 respectively.

B.1. Vertical load measurement improvement

To test the performance of the two methods to reduce the friction force at the micrometer screw, a simple test was performed. A known weight was applied on top of the bearing and removed sequentially. The difference between the measurements should represent the weight. This was done for several different horizontal displacements applied using the micrometer screw and for three different situations: normal - no compliant joint between bearing and micrometer screw, normal with touching - no compliant joint between bearing and micrometer screw but a small push was given against the bearing after every change in weight application, compliant - compliant joint between micrometer screw and the bearing. The weight was added and removed a total of ten times, resulting in ten measurements per set displacement. The mean error as a percentage of the average weight when the weight was applied directly to a force sensor (the 'correct' weight) including the spread of the individual measurements (indicated by the bars) for each method is shown in Figure B.1.

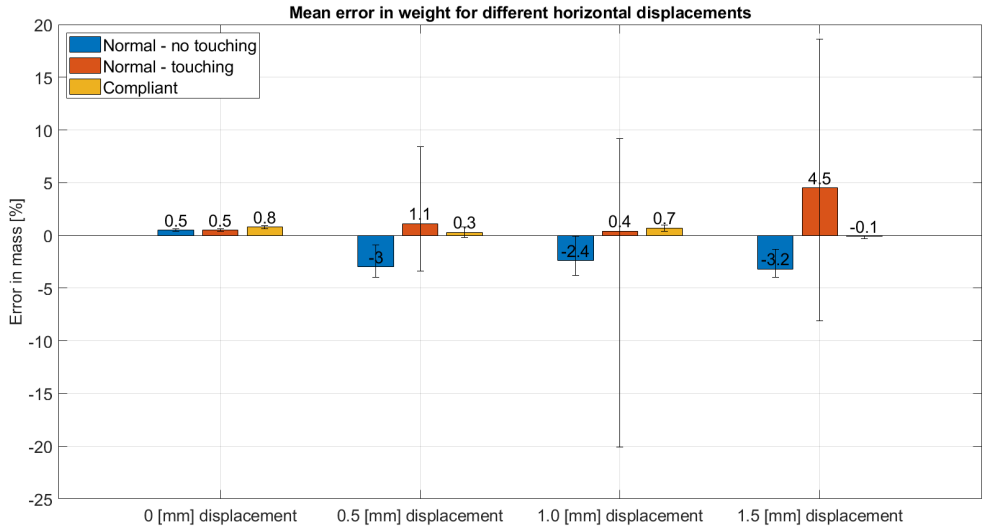

Figure B.1: Mean error in measured weight for different horizontal displacements and mitigating measures.

First, it should be noted that an error of 0.5-0.8% is present even for zero displacement. This is probably due to the fact that some internal forces are generated even without displacement, as the bearing is over-constrained due to the attachment to the two vertical load cells or due to the fact that the load cells are not perfectly loaded at their centers. Moreover, the fact that two sensors are used instead of one can also introduce a larger uncertainty.

It can be clearly seen that an error of $\sim 3\%$ is introduced when no measures are taken and a horizontal displacement is introduced. Also note that the error is always negative (for the 'normal - no touching' measurements), meaning the measured mass is lower than the actual weight. This supports the hypothesis that the friction takes up part of the load. The touch mitigation method clearly shows a very large spread in measured weight, indicating that it does not perform well and actually increases the friction force introduced at the interface. The introduction of the compliant joint shows that the error is reduced to $0.1 - 0.7\%$ with a very small spread of the measurements around the mean. This indicates that the compliant joint effectively decreases the error in measured weight due to friction even for the relatively large displacement of 1.5mm. It should be kept in mind that an error in the measured force of $\sim 1\%$ can still be expected due to friction at the interface between the micrometer screw and the compliant joint.

Important to note is that the error in vertical force measured could also be (partly) caused by another issue in the setup. Due to the horizontal force of the leaf springs, the vertical load cells will be loaded not only in the pure vertical direction, but also in the horizontal direction. It was attempted to investigate the effect of the horizontal force on the vertical force measurement; however, it is not easily isolated from a friction force introduced by introducing a horizontal displacement. Experiments could be designed to solely determine the effect of friction and the effect of horizontal force on the load cell. However, with the test described above both effects are captured together, which is the situation that is present in the experimental setup and is therefore a sufficient measure of the introduced uncertainty or error.

B.2. Stiffness of the compliant joint

The compliant joint introduces uncertainty in the horizontal displacement as prescribed by the micrometer screw due to its finite stiffness. A schematic mass-spring system representation of the bearing supported by the leaf springs and the prescribed displacement by the micrometer screw through the compliant joint is given in Figure B.2. For a known horizontal force F_h and displacement $x_{micrometer}$, the displacement of the bearing $x_{bearing}$ needs to be determined.

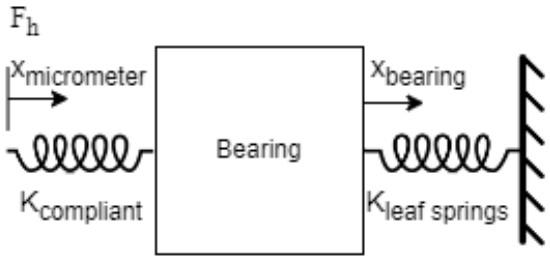

Figure B.2: Schematic mass-spring system representation of the bearing mounted on leaf springs and the displacement introduced via the compliant joint.

The change in the length of the spring that represents the compliant joint is equal to $\delta_{compliant} = x_{micrometer} - x_{bearing}$, while the change in the length of the spring that represents the leaf springs is equal to $\delta_{leaf\ springs} = x_{bearing}$. The sum of these should be equal to the displacement of the micrometer screw $x_{micrometer}$, resulting in Equation B.1.

$$x_{micrometer} = \delta_{compliant} + \delta_{leaf\ springs} \tag{B.1}$$

We can replace $\delta_{complaint}$ by $\frac{F_h}{K_{compliant}}$, replace $\delta_{leaf\ springs}$ by $x_{bearing}$ and by rearranging we arrive at Equation B.2.

$$x_{bearing} = x_{micrometer} - \frac{F_h}{K_{compliant}} \tag{B.2}$$

Only $K_{compliant}$ is unknown and was determined experimentally. During the experiment, the horizontal force F_h and the displacement $x_{micrometer}$ were measured with and without the compliant joint for a displacement of 0 and 1mm. Infinite stiffness of the bearing and load cell was assumed. Using the measurement without the compliant joint, the stiffness of the leaf springs was calculated as $K_{leaf\ springs} = \frac{F_h}{\delta_{leaf\ springs}}$. The equivalent stiffness of the compliant joint and leaf springs mounted in series was calculated based on the measurement with the compliant joint as $K_{eq} = \frac{F_h}{x_{micrometer}}$. For springs mounted in series, the equivalent stiffness is calculated as $\frac{1}{K_{eq}} = \frac{1}{K_1} + \frac{1}{K_2}$, which can be rearranged to calculate the stiffness of the compliant joint as in Equation B.3 (with K_1 = $K_{compliant}$ and K_2 = $K_{leaf\ springs}$).

$$K_{compliant} = \frac{1}{\frac{1}{K_{eq}} - \frac{1}{K_{leaf\ springs}}} \tag{B.3}$$

The range of displacements (0 to 1mm) was chosen so that the horizontal force range was comparable to the force encountered in the experiments. The stiffness of the compliant joint was found to be equal to 247N/mm.

C

Reynolds equation assumptions

	Assumption	Comments
1	Body forces are neglected	Not fully valid for magnetorheological lubricants as the external magnetic field exerts a force on the fluid; however, still generally used as an assumption for MR lubricated bearings.
2	Pressure is constant through the film	Always valid, since the thickness of hydrodynamic films is in the range of several micrometers. There might be some exceptions, e.g. with elastic films.
3	No slip at the boundaries	Always valid, since the velocity of the oil layer adjacent to the boundary is the same as that of the boundary.
4	Lubricant behaves as a Newtonian fluid	Usually valid, however not for MR lubricants. Models like Bingham or Hershel-Bulkley can be included in the generalized Reynolds equation with small adaptations.
5	Flow is laminar	Usually valid, except for large bearings, e.g. turbines.
6	Fluid inertia is neglected	Valid for low bearing speeds or high loads. Inertia effects are included in more exact analyses.
7	Fluid density is constant	Usually valid for fluids when there is not much thermal expansion. Definitely not valid for gases.
8	Viscosity is constant throughout the generated fluid film	Crude assumption but necessary to simplify the calculations, although it is not true. Definitely not true for MR fluids due to dependency on magnetic field. Change in viscosity due to the magnetic field strength can be taken into account by the generalized Reynolds equation.

Table C.1: Assumptions of the Reynolds equation. Taken and adapted from [2].

D

Viscoplastic rheological models

Rheological model	Reference	Equation
Bingham plastic	[23, 24]	$\tau = \tau_y + \eta\dot{\gamma} \quad \lvert\tau\rvert > \tau_y$
Herschel-Bulkley	[25]	$\tau = \tau_y + \eta(\dot{\gamma})^n \quad \lvert\tau\rvert > \tau_y$
Casson	[26]	$\sqrt{\tau} = \sqrt{\tau_y} + \sqrt{\eta\dot{\gamma}} \quad \lvert\tau\rvert > \tau_y$
Biviscous	[27]	$\tau = \begin{cases} \eta_r\dot{\gamma} & \tau \leqslant \tau_1 \\ \tau_y + \eta\dot{\gamma} & \tau > \tau_1 \end{cases}$
Biplastic Bingham	[28]	$\tau = \begin{cases} \tau_1 + \eta_r\dot{\gamma} & \tau \leqslant \tau_2 \\ \tau_y + \eta\dot{\gamma} & \tau > \tau_2 \end{cases}$
Papanastasiou	[29]	$\tau(\dot{\gamma}) = \tau_N(\dot{\gamma})W_1(\dot{\gamma}) + \tau_{Bn}(\dot{\gamma})W_2(\dot{\gamma})$

Table D.1: Viscoplastic rheological models for MR fluids. Taken and adapted from [30].

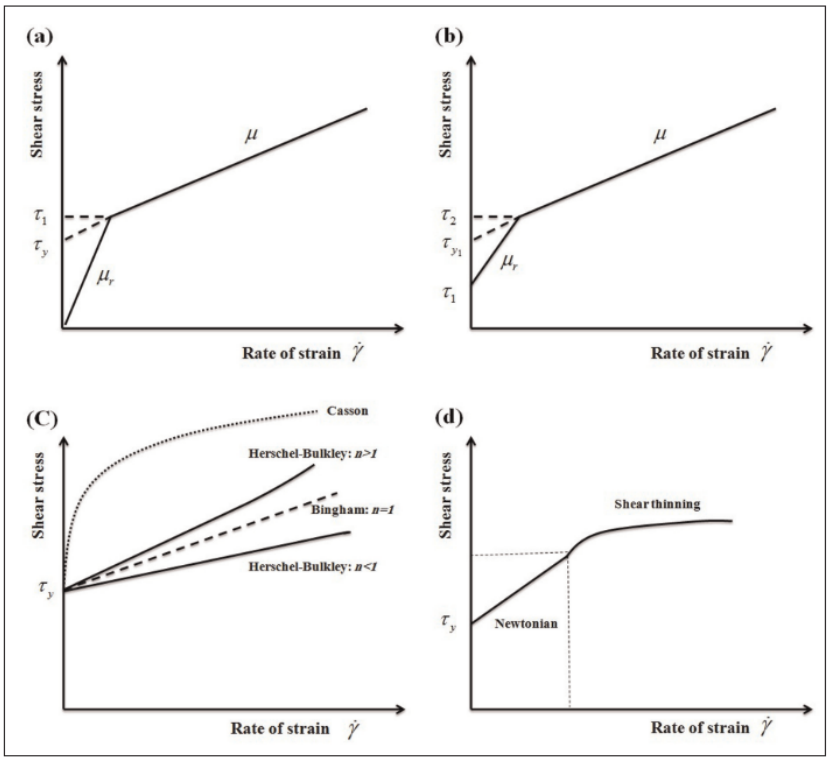

Figure D.1: Viscoplastic rheological models: (a) biviscous model; (b) biplastic Bingham model; (c) Bingham, Herschel-Bulkley, and Casson models; (d) Papanastasiou model. Taken from [30].

E

Verification of the model

To ensure proper implementation of the equations in COMSOL, verification has been performed using literature. Both the fluid flow model and the magnetic field model need to be validated. Verification of the fluid flow model implies verification of the implementation of Equation 3.3 (the Reynolds equation), which is done in section E.1. Verification of the magnetic field model implies verification of the implementation of Equation 3.22, Equation 3.23, Equation 3.24 and Equation 3.25, which is done in section E.2.

E.1. Reynolds equation verification

The Reynolds equation including cavitation algorithm implemented in this thesis is based on the paper of Alakhramsing et al. [14]. In their paper, they compared their method with reference measurement results, which showed good agreement. An important difference between the implementation of Alakhramsing et al. and the implementation in this thesis is that Alakhramsing et al. used non-dimensional parameters for numerical robustness. To verify correct implementation of the dimensional Reynolds equation, the dimensional Reynolds equation was solved and the resulting parameters were made dimensionless (dimensionless pressure P = $\frac{p(\Delta R)^2}{\eta U R_S}$ and dimensionless film-height H = $\frac{h}{\Delta R}$) which were then compared to the results presented by Alakhramsing et al.

Figure E.1 shows a comparison of the implementation of the 2D Reynolds equation from Alakhramsing et al. [14], including their comparison to literature, and the implementation of this thesis. Figure E.1a and Figure E.1b show the pressure distribution and Figure E.1c and Figure E.1d show the mass fraction distribution. Perfect agreement between the figures can be observed, verifying the implementation of the 2D Reynolds equation.

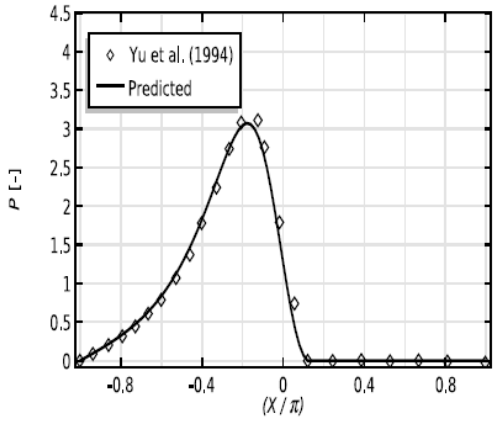

(a) Pressure distribution. Taken from [14].

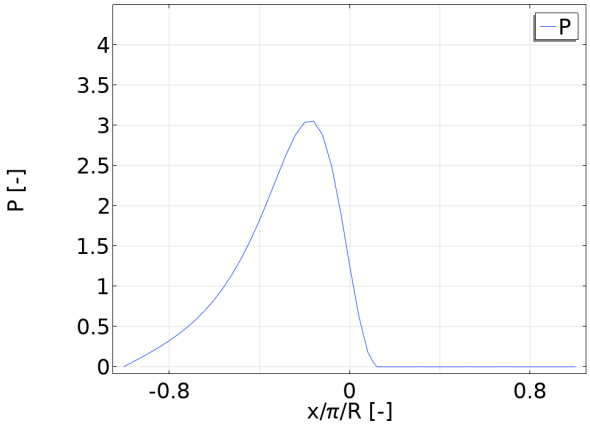

(b) Pressure distribution. Thesis implementation.

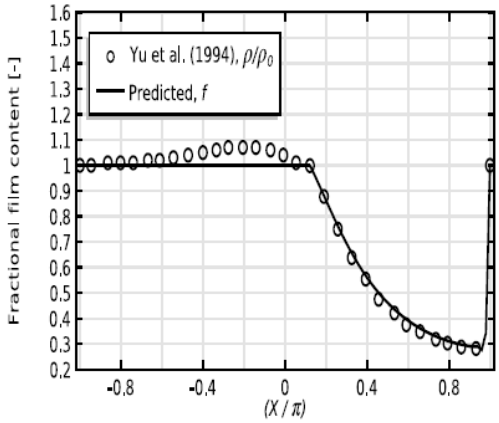

(c) Mass fraction distribution.Taken from [14].

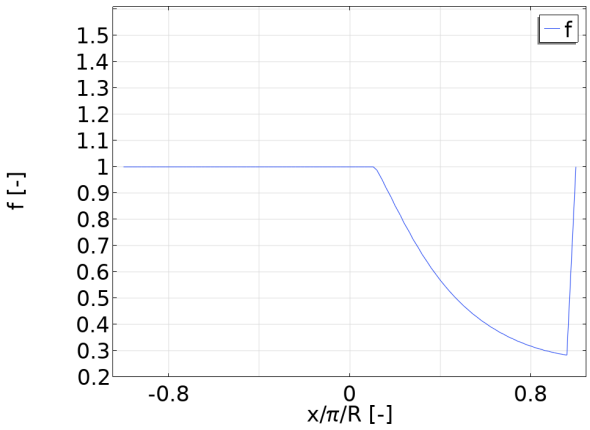

(d) Mass fraction distribution. Thesis implementation.

Figure E.1: Comparison of the 2D Reynolds equation implementation in [14] and this thesis. Pressure on all boundaries of the domain is set equal to 0. Results for $\epsilon = 0.6$ and plotted at y = 0.2R_B.

As in this thesis not only the pressure is analyzed, but more importantly the load capacity and friction force, it is important to also verify the implementation of Equation 3.8, Equation 3.9 and Equation 3.18. A comparison of the dimensionless load capacity ($F_{mag}(\Delta R)^2/(\eta\omega R_S^3 L_B)$) as a function of the eccentricity ratio and the dimensionless friction coefficient ($\mu R_S/\Delta R$) as a function of the Sommerfeld number ($S_o = \mu\omega R_S L_B \frac{R_S}{\Delta R}^2/(\pi F_{mag})$) is given in Figure E.2, where the implementation in this thesis is compared to the results of Gertzos et al. [31]. Gertzos et al. simulate the journal bearing by means of a CFD simulation with the Half-Sommerfeld boundary condition to take cavitation into account.

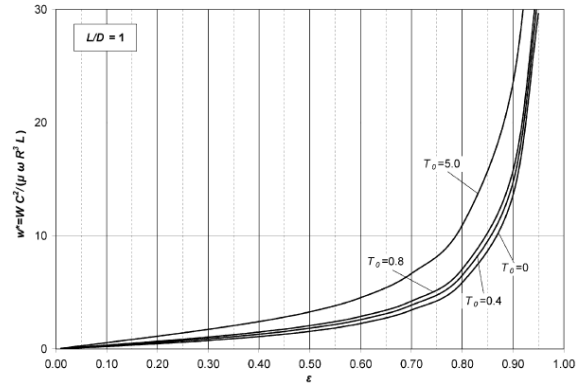

(a) Dimensionless load capacity. Taken from [31].

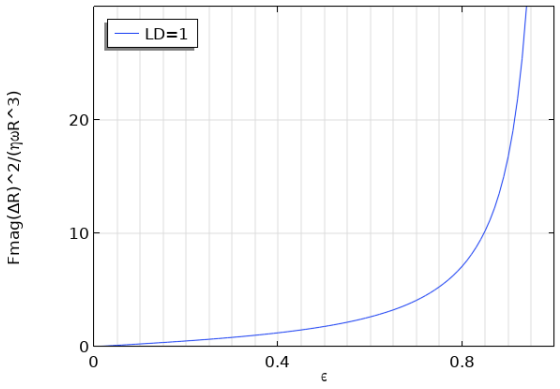

(b) Dimensionless load capacity. Thesis implementation.

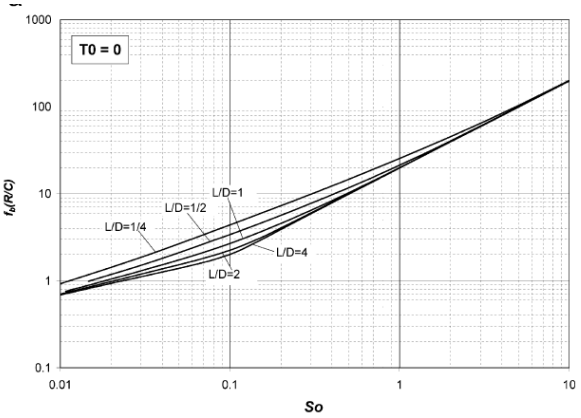

(c) Dimensionless friction coefficient. Taken from [31].

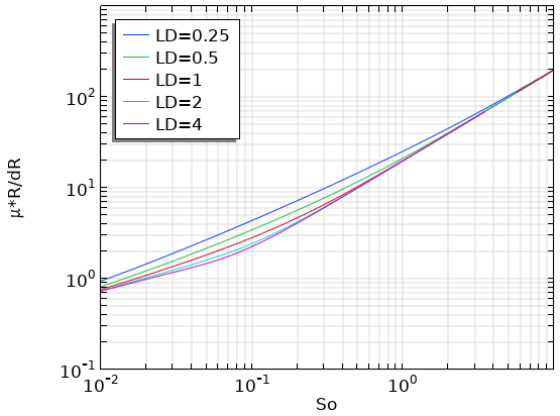

(d) Dimensionless friction coefficient. Thesis implementation.

Figure E.2: Comparison of the 2D Reynolds equation implementation in [31] and this thesis. Load capacity is plotted for various values of T_0 in [31], however only the line where $T_0 = 0$ should be used for comparison. Dimensionless friction coefficient is plotted for several L/D ratios.

The results are very comparable; however, it should be noted that the dimensionless load capacity found by Gertzos et al. is slightly lower compared to the load capacity found by the implementation of this thesis. This is due to the fact that the Half-Sommerfeld boundary condition causes a slightly lower maximum pressure compared to the cavitation algorithm as used in this thesis (when implementing the Half-Sommerfeld boundary condition in the implementation used in this thesis the results are identical to the results in Gertzos et al.). The dimensionless friction coefficient is in good agreement, which means that the friction force calculated by both models also has to be in good agreement. As the results correspond with literature, it can be concluded that the implementation of the Reynolds equation and calculation of load capacity and frictional force is done correctly.

E.2. Magnetic field model verification

The electromagnet design was based on the design used in Moles [10]. Therefore, the magnetic field model could easily be adapted to the exact design used in the thesis of Moles, which could thus be used as verification for the implementation in this thesis. In Figure E.3 a comparison is given of the magnetic field strength normal to the film height, inside the fluid film and at the center of the electromagnet.

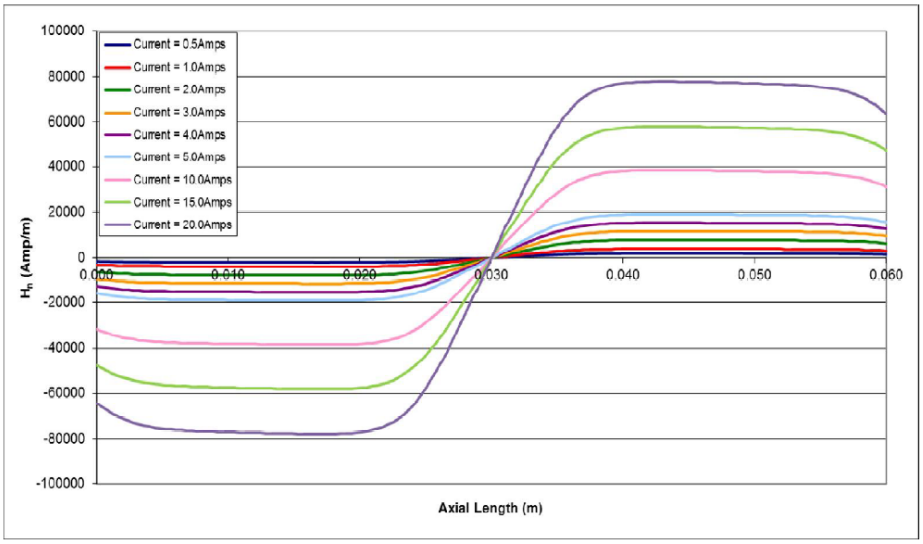

(a) Magnetic field strength. Taken from [10].

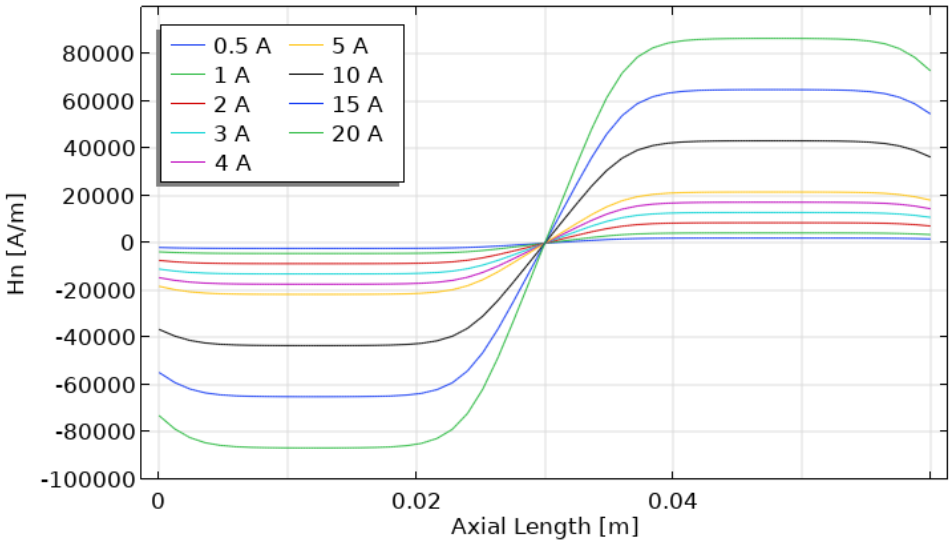

(b) Magnetic field strength. Thesis implementation.

Figure E.3: Comparison of magnetic field model implementation in [10] and this thesis. Magnetic field strength normal to film height within the fluid film at the center of the electromagnet for different values of the current through the coil.

It can be seen that the general shape of the magnetic field is comparable and also the magnitude is comparable, although in the implementation of this thesis it is slightly higher ($\sim 10\%$). This difference can be due to small differences in assumptions of the magnetic permeability of the fluid or due to slight differences in the modeled electromagnet and coil geometry. However, as the differences are not too large and the difference between the models is a constant factor, it can be assumed that the magnetic field model is implemented correctly. Furthermore, the magnitude of the magnetic field strength calculated in this thesis is tuned by determining the magnetic permeability of the materials by comparing the model results with experimental measurements (see subsection 3.2.2). Therefore, it is made sure that the magnetic field model will provide an accurate representation of the experimental magnetic field.

Raw data of the results

In this appendix, the 'raw' experimental results where the hydraulic oil was used as lubricant are presented without the adjustment for temperature.

F.1. Pressure

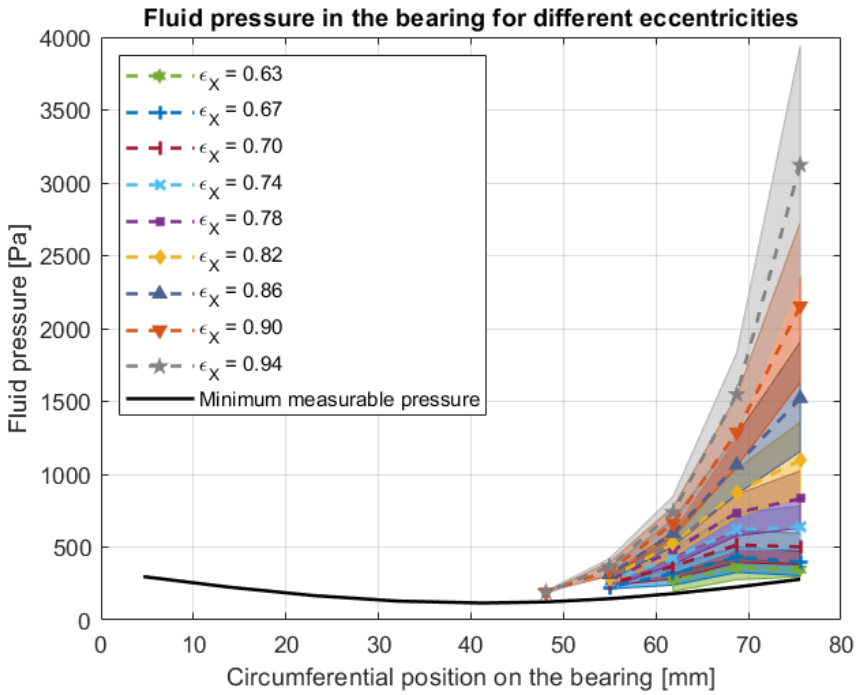

Figure F.1: Experimental pressure distribution for different eccentricity ratios with hydraulic oil lubricant. Raw data.

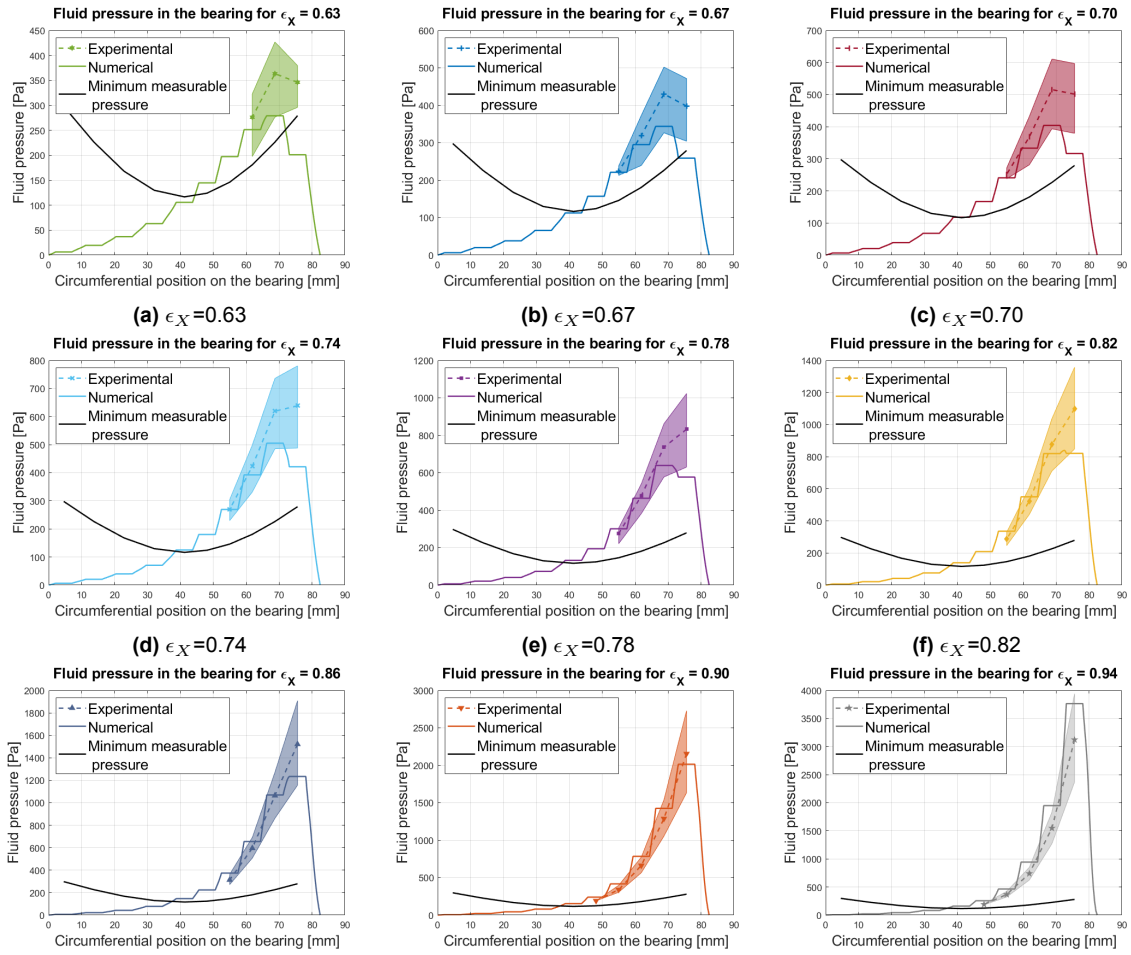

(a) ϵ_X=0.63 **(b)** ϵ_X=0.67 **(c)** ϵ_X=0.70

(d) ϵ_X=0.74 **(e)** ϵ_X=0.78 **(f)** ϵ_X=0.82

(g) ϵ_X=0.86 **(h)** ϵ_X=0.90 **(i)** ϵ_X=0.94

Figure F.2: Experimental and numerical results of the pressure distribution at the center of the bearing with hydraulic oil lubricant for different eccentricity ratios. Raw data.

F.2. Generated forces

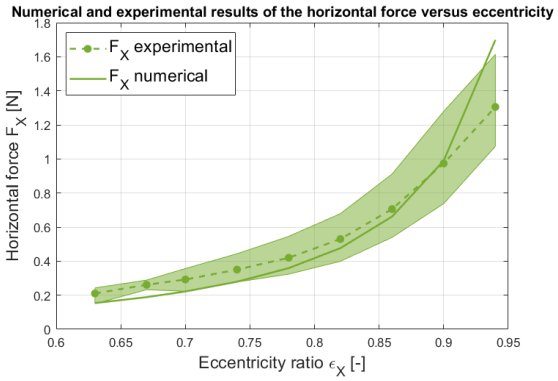

(a) Experimental and numerical horizontal force (F_X) plotted versus eccentricity ratio.

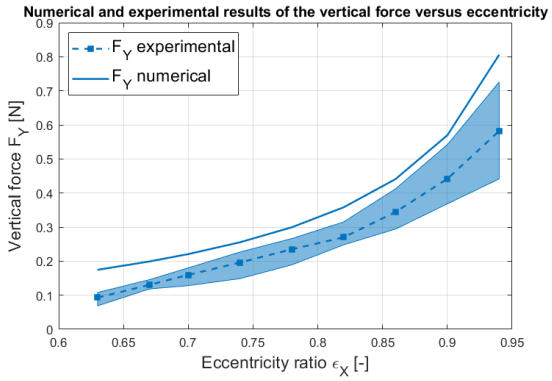

(b) Experimental and numerical vertical force (F_Y) plotted versus eccentricity ratio.

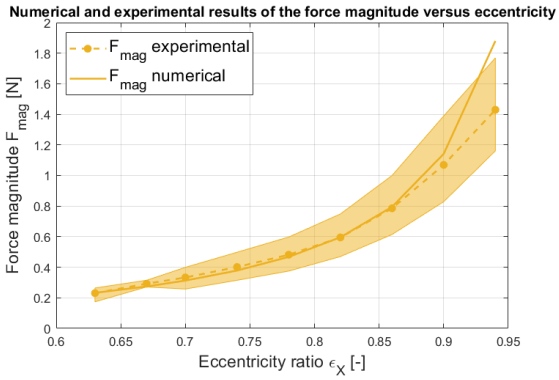

(c) Experimental and numerical force magnitude (F_{mag}) plotted versus eccentricity ratio.

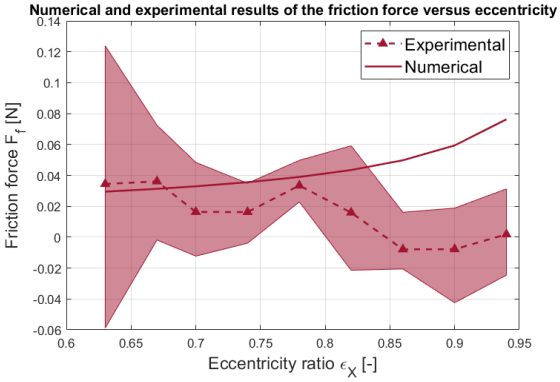

(d) Experimental and numerical Friction force (F_f) plotted versus eccentricity ratio.

Figure F.3: Experimental and numerical results of the generated forces in the bearing with hydraulic oil lubricant. Raw data.

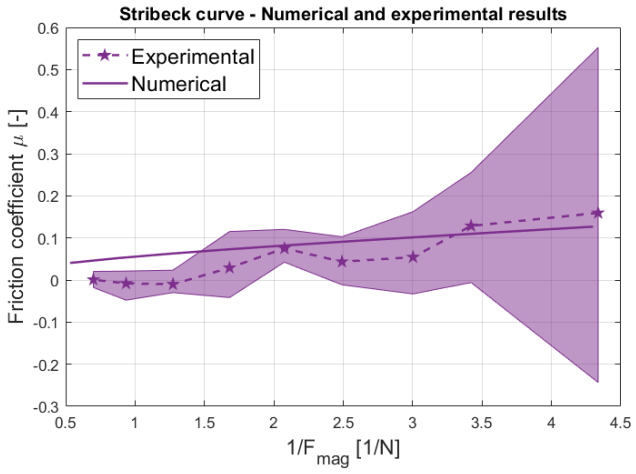

Figure F.4: Experimental and numerical Stribeck curve for hydraulic oil for a constant speed of ω = 50rpm. Raw data.

G

Results MR lubricated bearing

This appendix contains all the plots where the numerical and experimental results of the MR lubricated bearing are presented.

G.1. Pressure comparison

In this section the numerical and experimental pressure distribution for different eccentricity ratios and magnetic field strengths is presented.

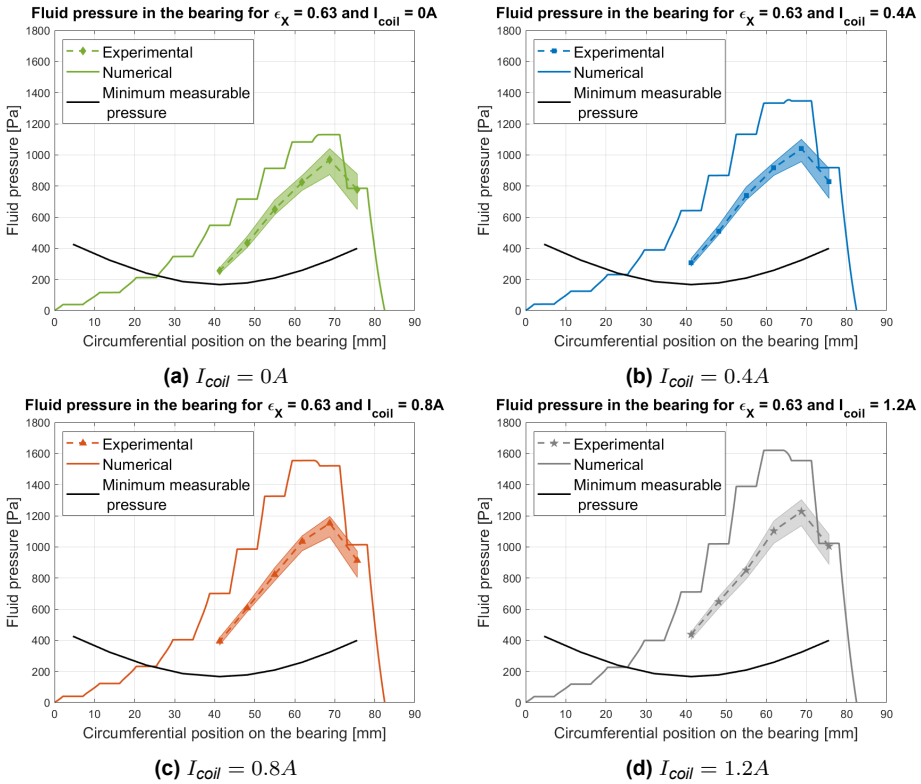

(a) $I_{coil} = 0A$ **(b)** $I_{coil} = 0.4A$

(c) $I_{coil} = 0.8A$ **(d)** $I_{coil} = 1.2A$

Figure G.1: Experimental and numerical pressure distribution for $\epsilon_X = 0.63$ with MR fluid lubricant for different values of applied current.

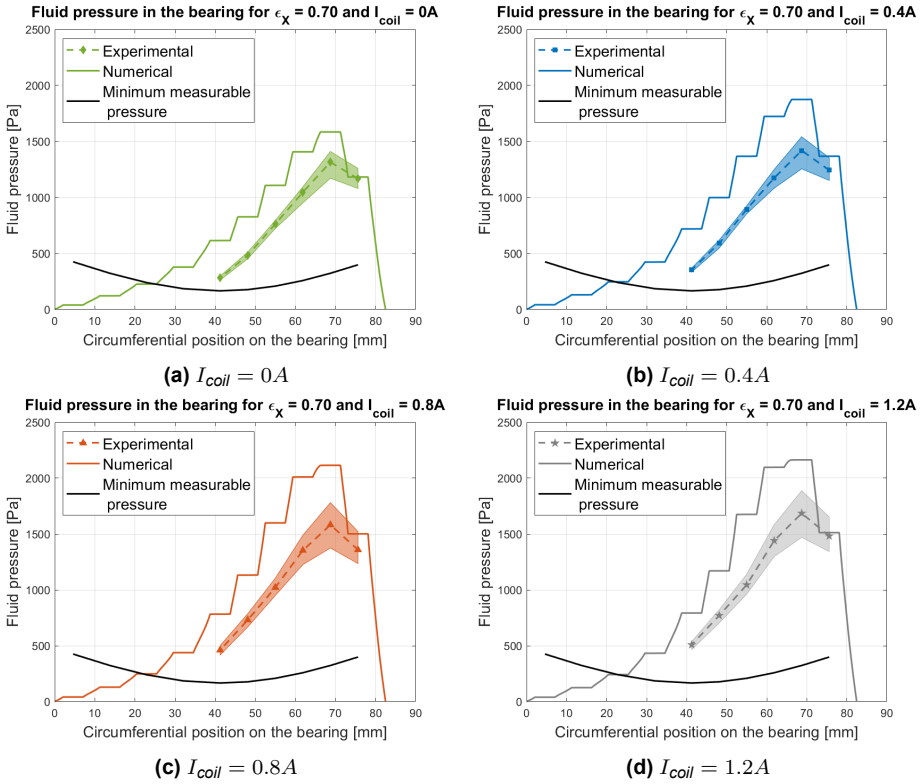

(a) $I_{coil} = 0A$ **(b)** $I_{coil} = 0.4A$

(c) $I_{coil} = 0.8A$ **(d)** $I_{coil} = 1.2A$

Figure G.2: Experimental and numerical pressure distribution for $\epsilon_X = 0.70$ with MR fluid lubricant for different values of applied current.

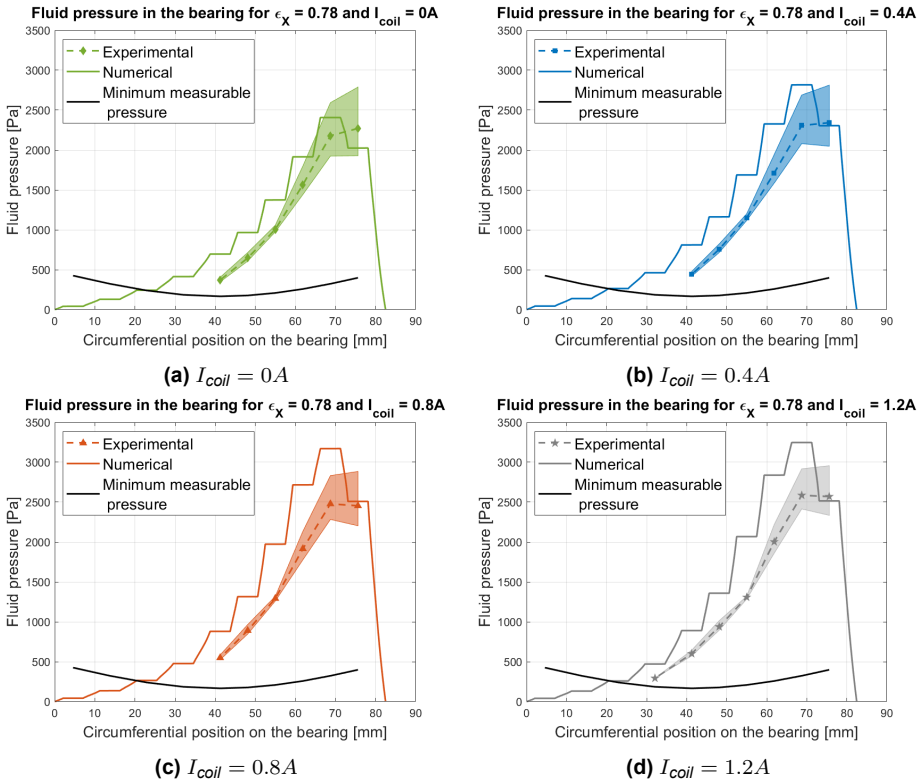

(a) $I_{coil} = 0A$ **(b)** $I_{coil} = 0.4A$

(c) $I_{coil} = 0.8A$ **(d)** $I_{coil} = 1.2A$

Figure G.3: Experimental and numerical pressure distribution for $\epsilon_X = 0.78$ with MR fluid lubricant for different values of applied current.

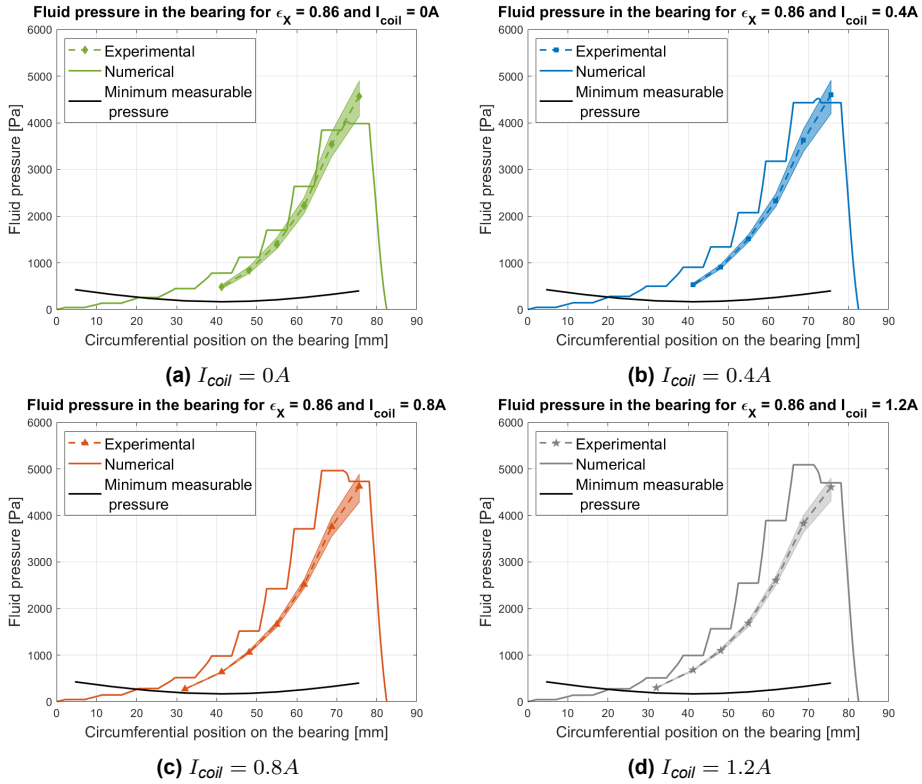

(a) $I_{coil} = 0A$ **(b)** $I_{coil} = 0.4A$

(c) $I_{coil} = 0.8A$ **(d)** $I_{coil} = 1.2A$

Figure G.4: Experimental and numerical pressure distribution for $\epsilon_X = 0.86$ with MR fluid lubricant for different values of applied current.

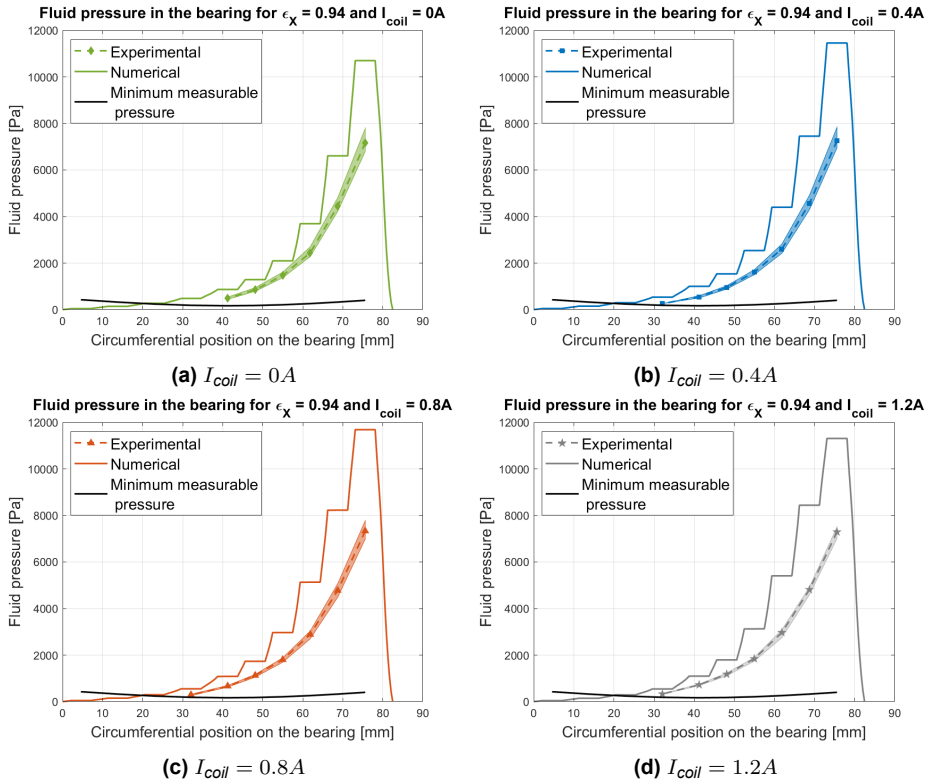

(a) $I_{coil} = 0A$ **(b)** $I_{coil} = 0.4A$

(c) $I_{coil} = 0.8A$ **(d)** $I_{coil} = 1.2A$

Figure G.5: Experimental and numerical pressure distribution for $\epsilon_X = 0.94$ with MR fluid lubricant for different values of applied current.

G.2. Generated forces comparison

In this section the horizontal force F_X, vertical force F_Y, force magnitude F_{mag}, friction force F_f and Stribeck curve found experimentally and numerically are compared for each eccentricity ratio and applied current separately.

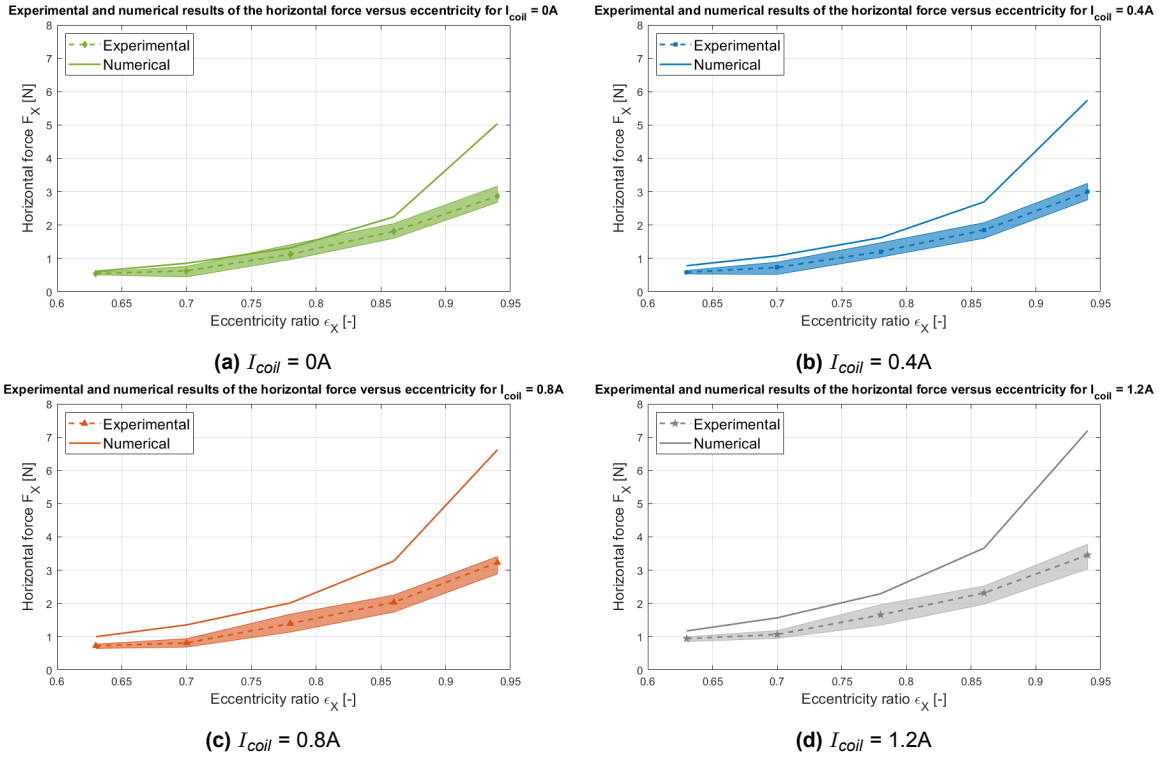

(a) I_{coil} = 0A

(b) I_{coil} = 0.4A

(c) I_{coil} = 0.8A

(d) I_{coil} = 1.2A

Figure G.6: Experimental and numerical results for horizontal force F_X plotted versus eccentricity ratio with MR fluid lubricant for different values of I_{coil}.

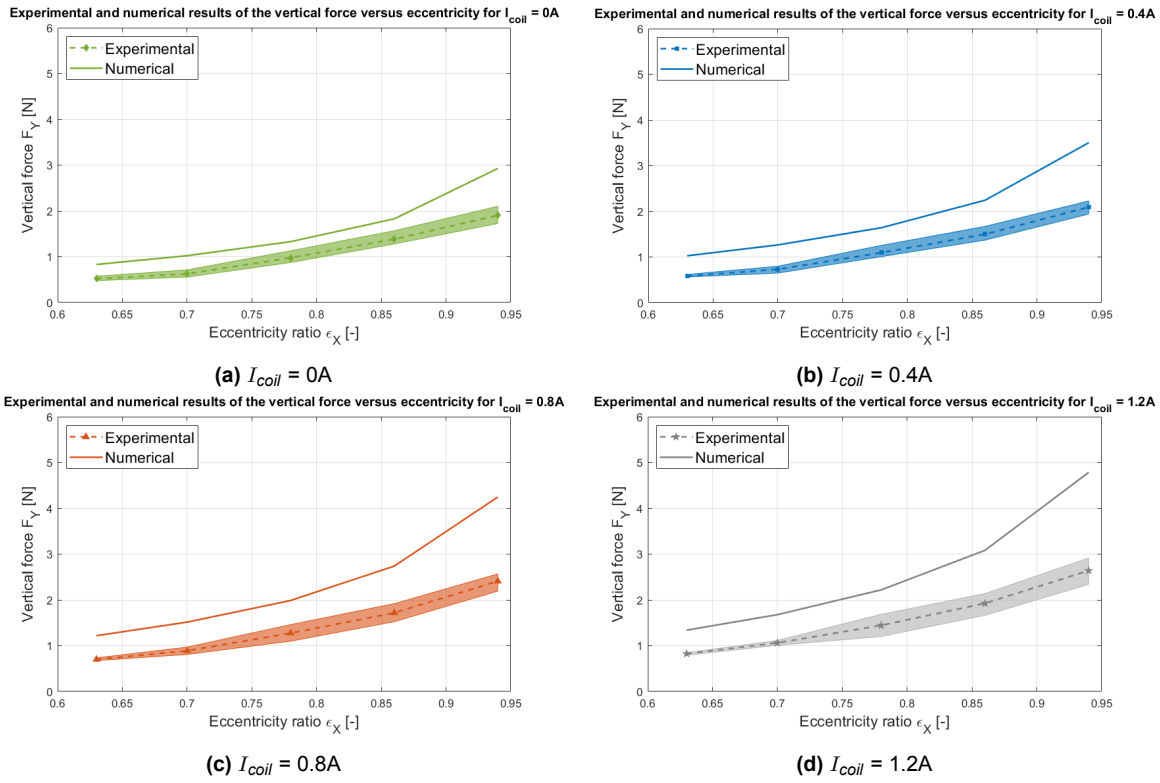

(a) I_{coil} = 0A **(b)** I_{coil} = 0.4A

(c) I_{coil} = 0.8A **(d)** I_{coil} = 1.2A

Figure G.7: Experimental and numerical results for vertical force F_Y plotted versus eccentricity ratio with MR fluid lubricant for different values of I_{coil}.

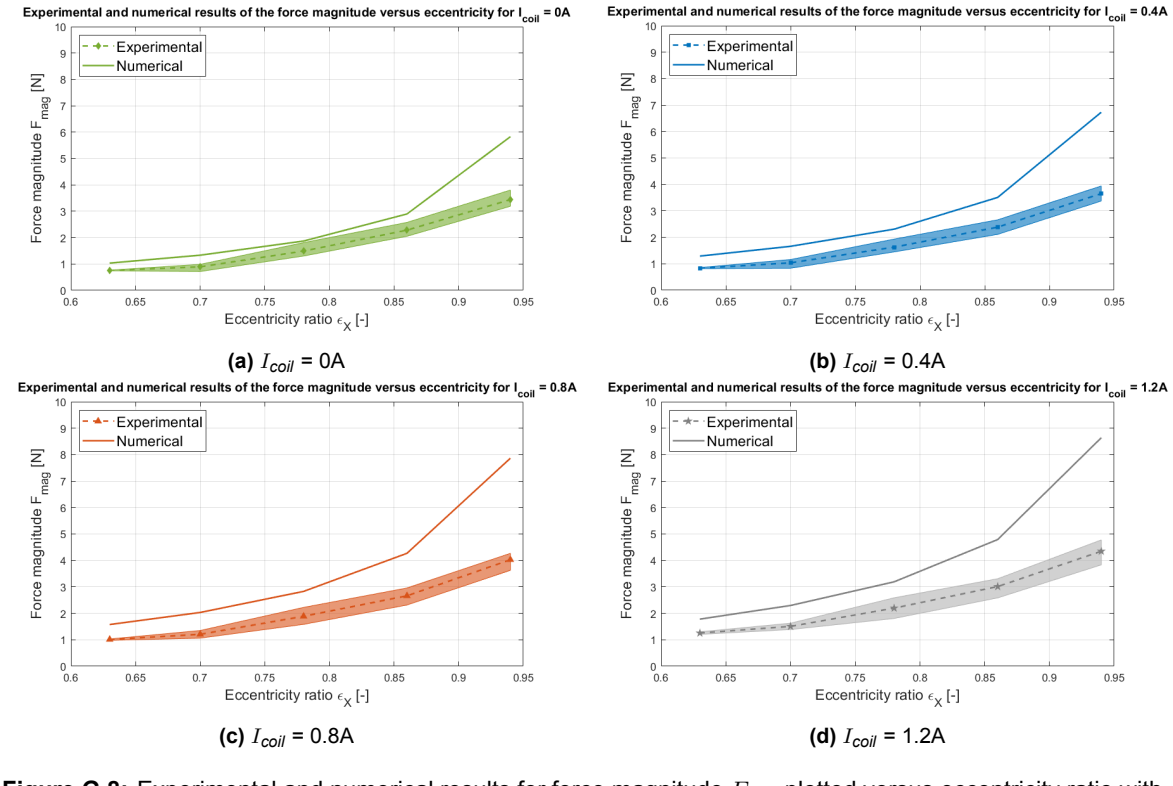

(a) I_{coil} = 0A **(b)** I_{coil} = 0.4A

(c) I_{coil} = 0.8A **(d)** I_{coil} = 1.2A

Figure G.8: Experimental and numerical results for force magnitude F_{mag} plotted versus eccentricity ratio with MR fluid lubricant for different values of I_{coil}.

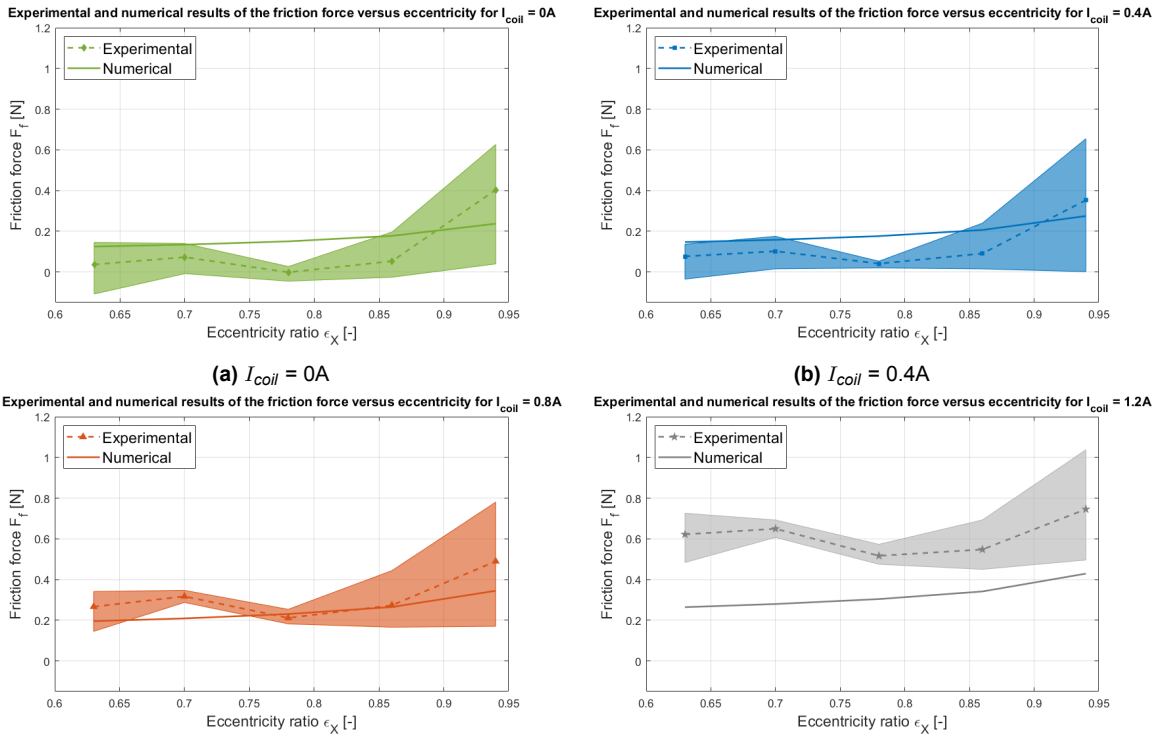

(a) I_{coil} = 0A

(b) I_{coil} = 0.4A

(c) I_{coil} = 0.8A

(d) I_{coil} = 1.2A

Figure G.9: Experimental and numerical results for friction force F_f plotted versus eccentricity ratio with MR fluid lubricant for different values of I_{coil}.

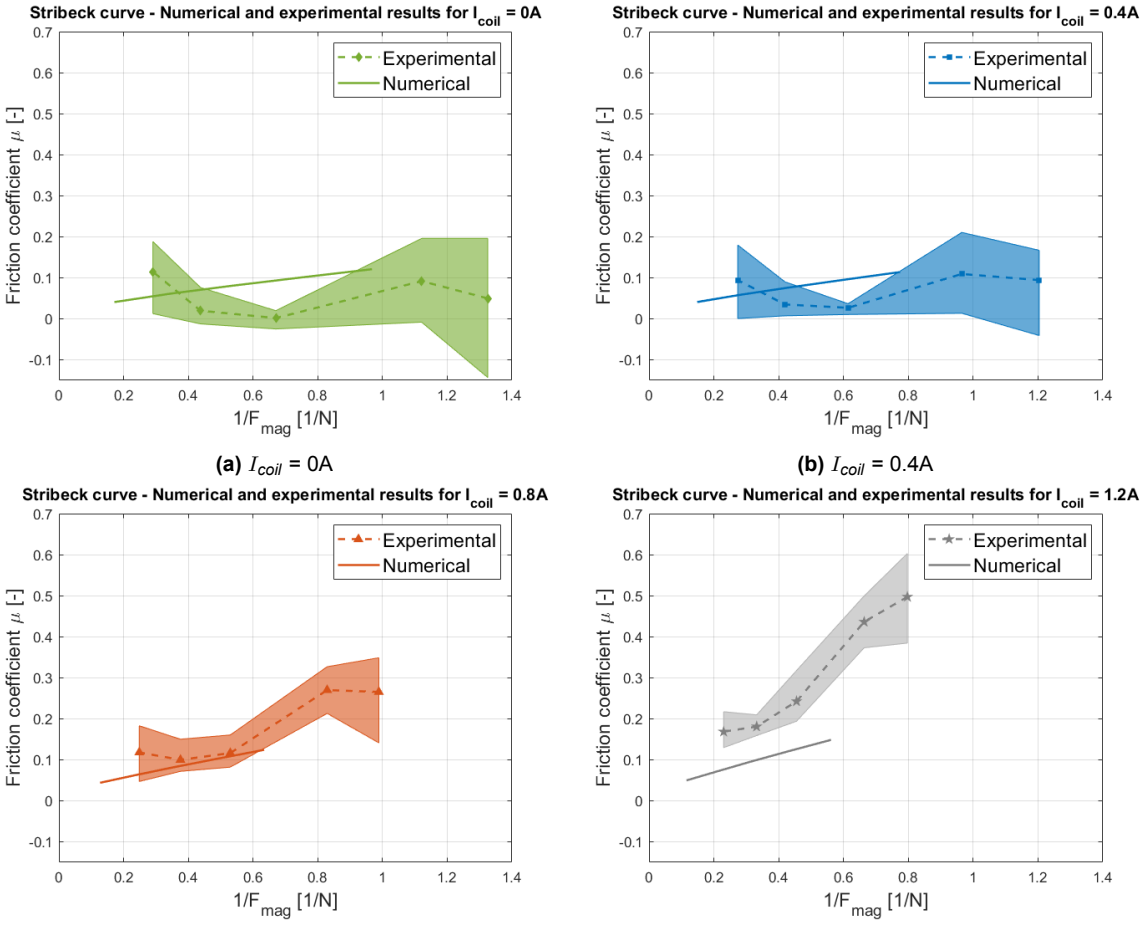

(a) I_{coil} = 0A

(b) I_{coil} = 0.4A

(c) I_{coil} = 0.8A

(d) I_{coil} = 1.2A

Figure G.10: Experimental and numerical Stribeck curve with MR fluid lubricant for different values of I_{coil} for a constant speed of ω = 50rpm.

Technical drawings

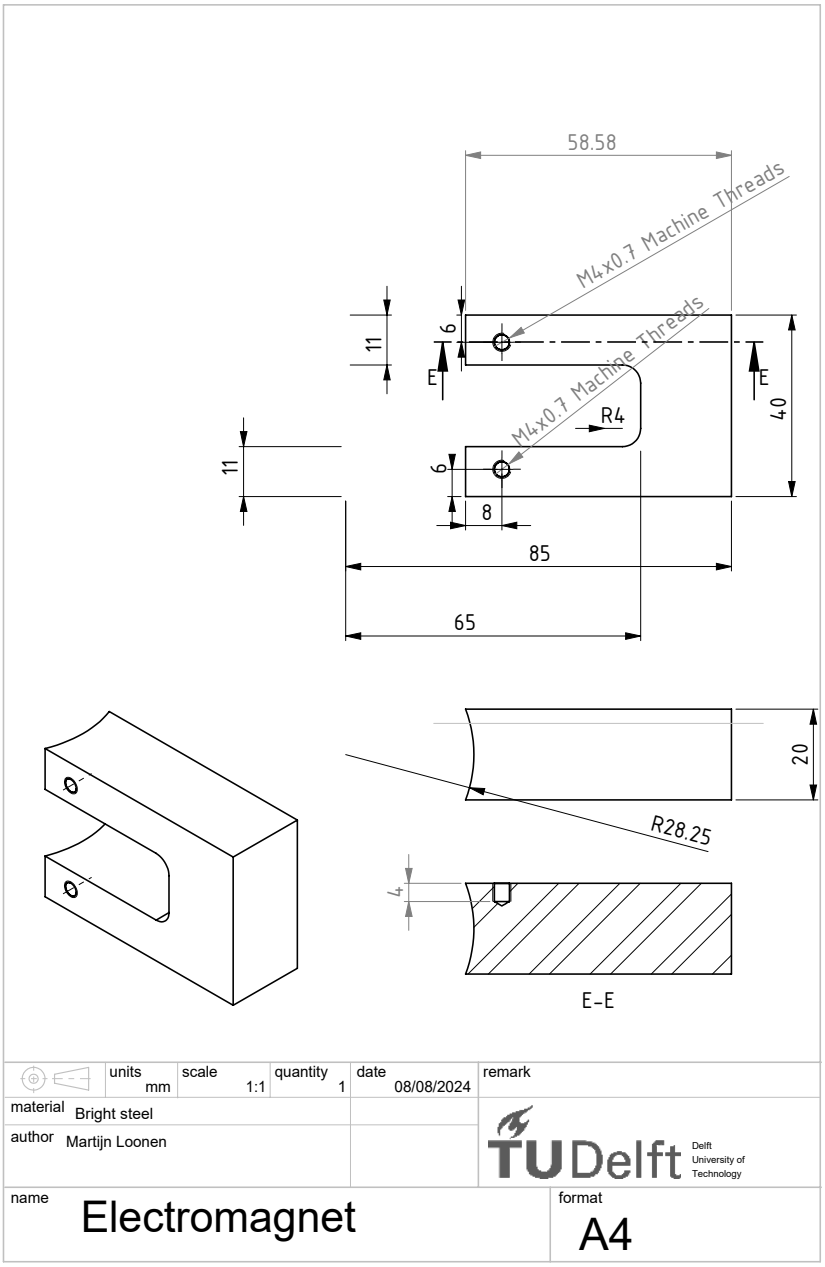

Figure H.1: Technical drawing of the electromagnet yoke.

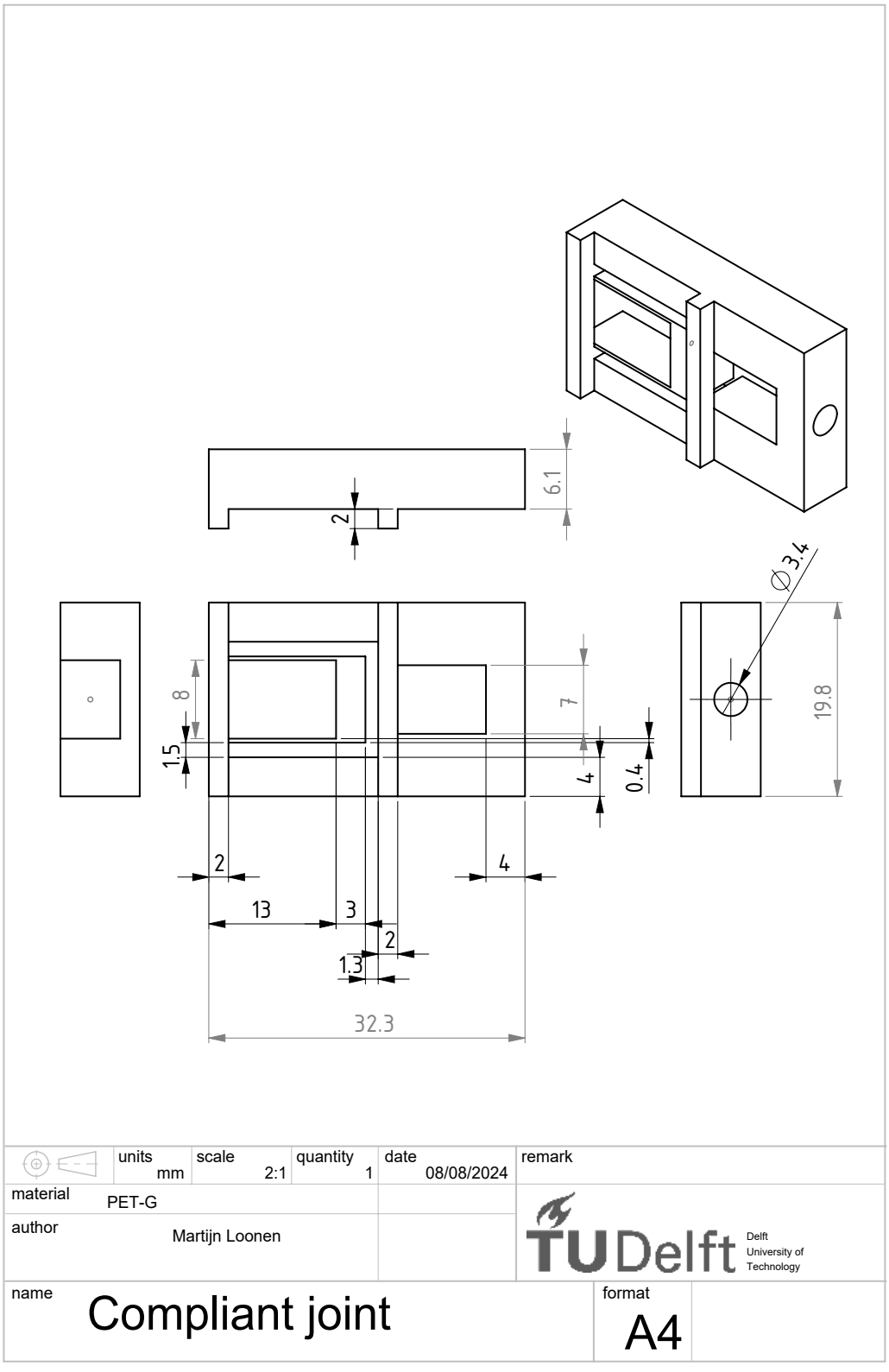

Figure H.2: Technical drawing of the compliant joint

Literature review

This appendix covers relevant (background) literature used and encountered throughout the thesis.

I.1. Magnetorheological fluids

This section gives a general overview of magnetorheological fluids, the operational modes and the most important challenges of the use of MR fluids. A quick introduction of smart fluids is given in subsection I.1 followed by the explanation of the magnetorheological effect in subsection I.1. Section 2.3 introduces the different operational modes of MR fluids. The structural properties formulating the rheological properties of MR fluids are discussed in subsection I.1. Finally, the stability and durability of MR fluids are discussed in subsection I.1 and subsection I.1 respectively.

I.1.1. Smart fluids

Smart fluids are a type of material of which the properties can (reversibly) change due to an external stimulus. A smart fluid consists of a carrier liquid in which nanometer- or micrometer-sized particles are suspended. Many different types of smart fluids exist, of which some interesting ones are magnetorheological and electrorheological fluids. The main difference between the two is that MR fluids are excited by an external magnetic field, while ER fluids are excited by an external electric field [4, 32]. ER fluids require thousands of volts and some milliamperes, while for MR fluids $\sim$2 Ampere and 2-24 V are required [33]. Moreover, MR fluids have a much higher yield strength (about a factor 10) and show better stability in the presence of contaminants [5, 33, 34]. Lastly, another disadvantage of ER fluids is that they need to be perfectly degassed and pressurized to exclude cavitation, which is less of an issue for MR fluids [5, 35]. For these reasons, MR fluids appear to be the most interesting smart fluids for application in hydrodynamic bearings.

I.1.2. Magnetorheological effect

MR fluids were discovered by Jacob Rabinow and the first time they were used was in a magnetorheological clutch at the US National Bureau of Standards in 1948 [36]. A distinction can be made between ferrofluids, fluids with nano-scale particles, and MR fluids, containing micron-sized particles (>1 μm) [4, 33, 37, 38]. When a magnetic field is applied to an MR fluid, a magnetic dipole is induced in every particle (as the particles are magnetically multidomain), resulting in strong interaction between the particles and the formation of structures (mainly chains in the direction of the magnetic field, see Figure I.1). As the particles are relatively large, the magnetic forces between the particles are dominant and the Brownian motion, induced by thermal forces, is generally negligible. This causes the MR fluid to transfer from liquid to semi-solid state, i.e. the magnetic particles introduce a yield stress which is dependent on the magnetic field strength. The apparent viscosity is also increased as a result of the increased flow resistance caused by the particle chains. In the absence of a magnetic field, the particles lose their magnetization and the MR fluid returns to the liquid state. The change in rheological properties of the MR fluid due to the presence of a magnetic field occurs within a few milliseconds. MR fluids are also shear-thinning, meaning their viscosity decreases for higher shear rates [4, 33, 37–39].

Since the magnetic particles in ferrofluids are magnetically single-domain and much smaller (nano-scale) the Brownian motion dominates the magnetic interaction between particles, meaning the ferrofluid will remain liquid even when a strong magnetic field is applied. The main effect of a magnetic field on a ferrofluid is the attraction and guidance of the fluid [4, 33]. Ferrofluids have applications in e.g. seals [40], inertia dampers [41, 42] and planar (pocket) bearings [43–47]. They do not show a significant change in rheological properties under the influence of a magnetic field and therefore cannot

be used as a tunable lubricant within hydrodynamic bearings [11, 48]. Hence, only MR fluids will be considered and discussed.

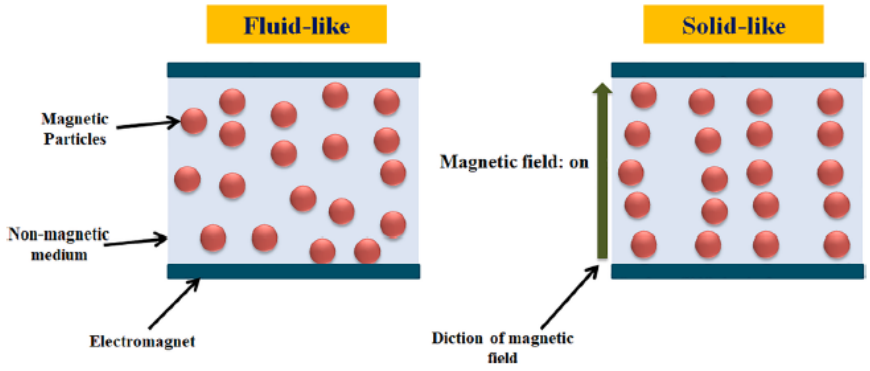

Figure I.1: The picture on the left shows the random orientation of the particles in the absence of an external magnetic field (where the fluid behaves like a Newtonian fluid). The picture on the right shows the formed structures by the particles under the influence of an external magnetic field (where the fluid is in semi-solid state and has a yield stress). Taken from [49].

I.1.3. Operational modes

Devices using MR fluids can be classified into three different operational modes: valve mode, shear mode and squeeze mode (see Figure I.2). All three modes will be briefly discussed below. Important to note is that combinations of the 3 operational modes are often encountered in devices [33, 39]. The proposed research will investigate (journal) bearings, which is a combination of both valve mode (due to the pressure buildup) and shear mode (due to the rotation of the bearing).

Valve mode

This operational mode is applied mainly in shock absorbers and dampers [33]. In valve mode a pressure difference is present that causes the fluid to flow, which is known as Poiseuille flow. The pressure drop consists of a pressure drop due to a viscous component (ΔP_r) and a magnetorheological component (ΔP_{mr}) which is proportional to the magnetic field strength, where the total pressure drop is the sum of the two $\Delta P = \Delta P_r + \Delta P_{mr}$ [33]. Using an electromagnet the pressure drop in e.g. a damper can be controlled resulting in a controllable flow restrictor, which is one of the first applications of MR fluids in the automotive industry [33, 50].

Shear mode

The direct shear mode is mainly used in clutches and brakes. In this mode, we do not look at the pressure drop but at a shear force due to relative movement of the surfaces. The shear force causes the fluid to flow and this type of flow is known as Couette flow. The shear force consists of the sum-

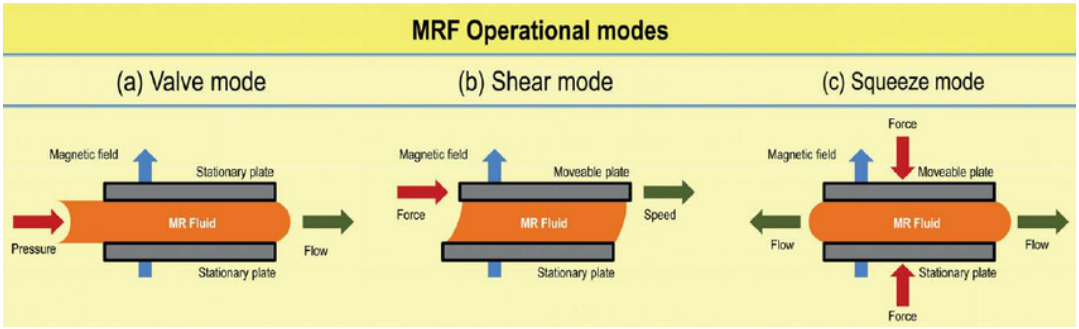

Figure I.2: Basic operational modes for MR fluid devices: (a) valve mode, (b) shear mode and (c) squeeze mode. Taken from [39].

mation of a purely viscous component (F_v) and a magnetorheological component (F_{mr}) which again is proportional to the magnetic field strength, where the total shear force is $F = F_v + F_{mr}$. The magnetorheological component makes the total shear force controllable by means of changing the magnetic field. Applications are already present in many automotive products [33, 50].

Squeeze mode
Little research has been performed on the squeeze mode. Some applications of this operational mode are in small-amplitude vibration dampers. The normal movement of the surfaces causes the fluid to flow as the volume is changed. Despite the limited amount of research performed on this operational mode, it has been suggested that the achievable yield stress could be ten times higher than in the other two operational modes [51].

I.1.4. Structural properties

To formulate the rheological behavior of MR fluids, three dimensionless numbers are generally used: Mason number (Mn), Peclet number (Pe) and lambda (λ).

λ is defined as the ratio between two magnetic moments in the linear regime with respect to the thermal energy [39]. The magnetic moment of an isolated particle surrounded by fluid under the influence of external magnetic field H_0 is given as $m = 4\pi\mu_0\mu_f\beta a^3 H_0$, with contrast factor or coupling parameter β defined as $\beta = \frac{\mu_p - \mu_f}{\mu_p + 2\mu_f}$, where μ_f, μ_p and μ_0 are the relative permeability of the fluid, particle and vacuum respectively and a the radius of the particle [52]. In strong magnetic fields, the particle magnetization saturates and the magnetic moment becomes independent of magnetic field strength. The magnetic moment is then given as $m = \frac{4}{3}\pi\mu_0\mu_f a^3 M_s$, where M_s is the saturation magnetization [39]. The magnetic moments of the particles cause them to align with the magnetic field and to aggregate. The thermal energy however disrupts the formed particle chains. The definition of λ is given in Equation I.1 where k is the Boltzmann constant and T is the temperature [30, 39, 52]. For small values of λ, the movement of the particles is mainly influenced by Brownian forces. For λ > 1 the magnetic forces dominate. Bossis et al. [52] found that for usual magnetic fields, $\lambda > 1$ for magnetorheological fluids (meaning magnetic forces dominate) and $\lambda < 1$ for ferrofluids (meaning Brownian forces dominate). This means that it is not expected to see significant changes in viscosity for ferrofluids in the presence of a magnetic field.

$$\lambda = \frac{1}{4\pi\mu_0\mu_f}\frac{m^2}{a^3}\frac{1}{kT} = \frac{\pi\mu_0\mu_f\beta^2 a^3 H_0^2}{2kT} \tag{I.1}$$

The Mason number is defined as the ratio between hydrodynamic (shear) forces and magnetic forces and is given in Equation I.2, where η_f is the fluid viscosity and $\dot{\gamma}$ is the magnitude of the shear rate tensor [52]. Note that other definitions of the Mason number in literature also exist [53, 54].

$$Mn = \frac{8\eta_f\dot{\gamma}}{\mu_0\mu_f\beta^2 H_0^2} \tag{I.2}$$

The Peclet number is the ratio of hydrodynamic to Brownian forces and is given in Equation I.3. For large values of the Peclet number, the Brownian forces can be neglected [52].

$$Pe = \frac{6\pi\eta_f\dot{\gamma}a^3}{kT} \tag{I.3}$$

These three numbers define the ratios between the most important forces on an MR fluid. They are related to each other as $Mn \cdot \lambda = \frac{2}{3}Pe$. Research showed that (in case of negligible short-range forces) for the same values of Mn, λ and volume fraction (ϕ), all rheological properties have the same magnitude [39, 52].

I.1.5. Stability

One of the big challenges of MR fluids is the stability. The large density difference between the magnetic particles and the carrier fluid causes sedimentation of the particles. Furthermore, aggregation of particles is present even in the absence of an external magnetic field due to remnant magnetization of the particles. These are considered as two fundamental problems of MR fluids. Several solutions to reduce sedimentation and aggregation of MR fluids have been proposed in literature which are discussed below [4, 38, 39, 49, 55]. Some examples of research on these technologies are given, but for a more complete overview the reader is referred to the review papers of Kumar et al. and Ashtiani et al. [38, 49].

1. Reducing particle size: Decreasing the particle size helps prevent the sedimentation of particles; however, this is limited as it decreases the MR effect and by approaching the nanometer range the Brownian forces will dominate (like in ferrofluids).
2. Particle coating: By decreasing the density of particles with a coating (e.g. amorphous silica or organic polymers), the density mismatch between particles and carrier fluid is decreased, limiting sedimentation. Moreover, the core materials are protected against degradation [56].
3. Magnetic nanoparticles: By using a ferrofluid as the carrier fluid, magnetic nanoparticles are introduced into the suspension. The nanoparticles form a cloud around the microparticles, increasing stability against aggregation and sedimentation. Furthermore, several studies show that the addition of magnetic nanoparticles also increases the yield stress [57, 58].
4. Wire/2D-shaped particles: By using wire-shaped particles, 2D sheet-like structures or flake-shaped particles in MR fluids, some researchers have increased the yield stress (improved the MR effect) and the sedimentation stability. Some examples are the addition of nanowires in an MR fluid [59, 60], using flake-shaped carbonyl iron microparticles [61] and using 2D nanocomposites as dispersed particles [62]. Many more examples can be found in [38, 49].
5. Carrier fluid: Another area of research to limit sedimentation is using more viscous fluids like lubricating oil or gel. Although this reduces sedimentation, it also increases the viscosity in the absence of a magnetic field, which is undesirable. An example of carbonyl iron particles dispersed into a polymeric suspension can be found in [63].
6. Additives: Research into many additives for MR fluids has been done to increase the stability. Some examples of additives are surfactants, polymeric compounds and solid fillers (e.g. guar gum, graphite fiber, or fumed silica). The additives increase stability by inhibiting space between the magnetic particles, separating them and thus limiting aggregation. Two examples of research on the effect of additives (graphite nanofibre and fumed silica) on the stability of MR fluids are performed by Lim et al. [64, 65].

Taking into account all the above-discussed methods to increase stability, using a combination of ferrofluids and MR fluids, using nanowires and adding stabilizers appears to be a proper method to improve stability and the MR effect [38].

One other cause for sedimentation could be due to the presence of a non-uniform magnetic field. When a gradient is present in a magnetic field, a magnetic dipole will not only align with the magnetic field, but a force will be exerted on the particle in the direction of the magnetic field gradient [66, 67]. This force, called the magnetophoretic force, is defined as in Equation I.4 [68, 69]. Depending on the magnetic field gradient present in the bearing, this force could cause sedimentation of the particles in the MR fluid. This principle has been used in literature, to generate self-healing surface textures (see also subsection I.4) [70]. In literature where sedimentation was not desired and the aim was to improve bearing performance, this phenomenon has not been addressed to be an issue, probably because the design was always aimed at having a uniform magnetic field. Therefore, the gradient in the magnetic field is generally small and does not cause a significant magnetophoretic force. However, this could be an important phenomenon to keep in mind in the bearing design and primarily in the electromagnet design.

$$F = m\nabla H = 4\pi\mu_0\mu_f\beta a^3 H\nabla H = 2\pi\mu_0\mu_f\beta a^3\nabla(H^2) \tag{I.4}$$

I.1.6. Durability

Another issue of MR fluids is the lack of durability, which is caused by the oxidation of the iron particles [39]. Oxidation of the iron particles causes an increase in off-state viscosity ("in-use-thickening") [71]. This is believed to be caused by the brittle oxidation layer, which breaks apart into nano-sized particles. The increase in solid volume or colloidal forces between the small particles may be the cause of the increase in off-state viscosity. Moreover, a decrease in field-induced yield stress is observed, caused by a decrease in particle magnetizability [72].

I.2. Hydrodynamic bearings

The section will elaborate on hydrodynamic bearings. First, the principle of hydrodynamic lubrication is explored in subsection I.2, after which the friction regimes and the Stribeck curve are discussed in subsection I.2 and subsection I.2 respectively. The concepts of eccentricity and cavitation are discussed in subsection I.2 and subsection I.2 respectively followed by the introduction of the Sommerfeld number in subsection I.2.

I.2.1. Hydrodynamic lubrication principle

Wear and friction occur in every system with relatively moving surfaces, but are both difficult to manage [1]. In a hydrodynamic bearing, the moving surface is fully supported by a pressurized lubricating film, meaning that the bearing surfaces do not make physical contact. Therefore, friction is only caused by viscous shearing of the lubricant and mechanical wear is removed. In contrast to hydrostatic bearings, where the lubricant is pressurized by an external pressure source (e.g. a pump), the lubricating film gets pressurised by the relative motion of the bearing surfaces. For hydrodynamic lubrication to occur, two conditions need to be met [1, 2]:

1. The (bearing) surfaces need to move relatively with sufficient velocity
2. The (bearing) surfaces need to have a relative angle with respect to each other (they cannot be parallel)

Note that the surfaces can be parallel and still generate a pressurized film in two cases: the surfaces are parallel but stepped or the surfaces are parallel but move towards each other [1, 2, 73]. The two most common types of hydrodynamic bearings are thrust bearings (used to support an axial load) and journal bearings (used to support a radial load). As thrust bearings usually have parallel bearing surfaces, tilted pads, a stepped surface or surface textures are needed to generate the hydrodynamic pressure.

The principle of the pressure generation between two non-parallel moving surfaces is shown in Figure I.3. We assume here that the bottom surface is moving. The lubricant is pulled along with the bottom surface in between the two surfaces. To make sure the same amount of lubricant is entering and leaving the wedge-shaped area, a pressure field is generated. On the right side, the entry flow is limited by the increasing pressure. On the left side, the exit flow is increased by the decreasing pressure. The pressure profile causes the lubricant velocity profile as shown in Figure I.3 and also creates a load-bearing capacity between the plates. [1, 2, 73]

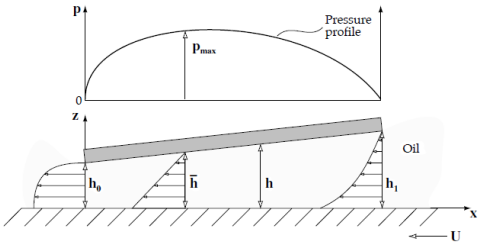

Figure I.3: Hydrodynamic pressure generation principle. Taken from [2].

I.2.2. Friction regimes of hydrodynamic bearings

In order to sustain a specific radial load, the relative surface velocity needs to be large enough such that

a strong enough pressure field is generated which fully supports the bearing load. This situation is called ”hydrodynamic/full-film lubrication”, which is desired as it removes mechanical wear and the friction is significantly lower (compared to the other lubrication regimes). When the velocity is reduced, the film thickness will decrease as the pressure magnitude is proportional to the square of the film thickness. However, for too low velocities the film thickness will be so thin that the surface will come into contact due to surface imperfections, increasing friction and introducing mechanical wear. This situation is called ”mixed lubrication” and the bearing load is partly transmitted by hydrodynamic pressure and partly by mechanical contact. For even lower velocities, complete solid contact of the surfaces occurs, which is called ”boundary lubrication”. In this case, the generated hydrodynamic pressure is negligible and the bearing load is transmitted through mechanical contact, where the lubricant only acts to reduce wear and friction. The friction coefficient in the hydrodynamic regime is about $\mu_{HL} \approx 0.01 - 0.001$, while for boundary lubrication it is about $\mu_{BL} \approx 0.08 - 0.014$ [1]. The minimal film thickness at which the asperities of the bearing surfaces will touch can be estimated using the film thickness parameter Δ, which is defined as in Equation I.5 [1]. Here, Rq_1 and Rq_2 indicate the RMS of the roughness of the surfaces and h is the film thickness. If Δ < 1, the bearing operates in the boundary layer regime and for Δ > 3-4 it operates in the hydrodynamic regime.

$$\Delta = \frac{h}{(Rq_1^2 + Rq_2^2)^{1/2}} \tag{I.5}$$

I.2.3. Stribeck curve

Figure I.4 is an example of a Stribeck curve [74], which plots the friction coefficient versus the dimensionless Hersey number $\frac{\eta N}{P}$ (where η is the dynamic viscosity, N the rotational speed and P load per unit length). Hersey [75] showed that friction due to viscous shear was a unique function of η, N and P. The Stribeck curve is sometimes also plotted versus velocity instead of Hersey number and the x-axis is also regularly plotted on a logarithmic scale (as the boundary layer regime is generally small). This curve shows the friction regimes as mentioned in subsection I.2 and also shows the limitation of hydrodynamic bearings. In order to operate at a low friction coefficient and minimize wear, the velocity needs to be large enough such that hydrodynamic lubrication is generated. However, during speeding up or slowing down, the bearing will go through the boundary and mixed lubrication regimes with much higher friction coefficients and much more wear. By lowering the transition speed (to hydrodynamic lubrication), friction and wear can be reduced. One way of doing this is by increasing the viscosity, however, this would also increase the friction coefficient at higher velocities. This is where MR fluids show an interesting property. As explained in subsection I.1, MR fluids have a larger apparent viscosity when an external magnetic field is applied. When the magnetic field is applied using electromagnets, the magnetic field can be applied at low velocities such that the transition speed is decreased. As soon as the velocity is large enough, the magnetic field could be decreased in strength (or entirely removed) to lower the viscosity while staying in the hydrodynamic regime, minimizing friction. This concept will be elaborated on in more detail in section I.4 where also already performed research on this topic will be discussed.

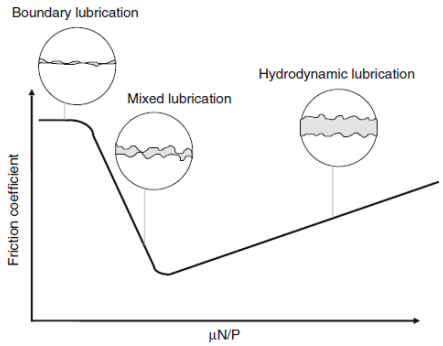

Figure I.4: Stribeck curve showing the three lubrication regimes. Friction coefficient is plotted versus Hersey number. Taken from [3].

I.2.4. Eccentricity

In a journal bearing the shaft is not always centered with the bearing. The displacement of the shaft center with respect to the bearing center is defined as the eccentricity (e), usually given as the eccentricity ratio $\epsilon = \frac{e}{\Delta R}$, where ΔR is the difference between the bearing radius and the shaft radius. An eccentricity ratio of zero means that the shaft is centered in the bearing and ϵ = 1 means the shaft is touching the bearing. Using the eccentricity ratio, the film thickness along the bearing surface can be defined, which is done using Figure I.5. Using figure Figure I.5b we can define the film thickness (h) as in Equation I.6. As α is very small, we can assume $cos(\alpha) \approx 1$ and using the definition of the eccentricity ratio, h can be expressed in terms of ΔR, ϵ and θ (θ is defined from h_{max}) as in Equation I.7 [1, 2].

$$h = e\cos\theta + R_1\cos\alpha - R_2 \tag{I.6}$$

$$h = \Delta R(1 + \epsilon cos\theta) \tag{I.7}$$

(a) Schematic drawing of a journal bearing.

(b) Detailed drawing.

Figure I.5: Schematic drawings of a journal bearing for the definition of film thickness. R_1 and R_2 are the radii of bearing and shaft respectively, O_B and O_S the center of bearing and shaft respectively, e the eccentricity and h the film thickness. Both taken from [2].

I.2.5. Cavitation

If a hydrodynamic bearing has a converging and diverging area, cavitation should be taken into account. An example of such a bearing is a (plain) journal bearing. When a journal bearing is rotating, lubricant is dragged in between the shaft and bearing increasing the pressure in the converging region. In the diverging region the pressure decreases and even becomes negative. However, in fluids negative pressures are suppressed by the cavitation pressure. Three types of cavitation exist [76, 77]:

1. Gaseous cavitation: When the pressure falls below the saturation pressure of the gasses dissolved in the fluid, the gasses will diffuse forming a gas bubble.
2. Pseudo-Cavitation: The gas bubble expands due to depressurization, but no more gas is diffused from the liquid (e.g. the mass of the gas bubble does not increase).
3. Vaporous cavitation: If the pressure goes below the vapor pressure of the lubricant, the lubricant can start to boil causing bubbles to form which collapse, causing cavitation erosion. Vaporous cavitation is normally only present in bearings with dynamic loading [78].

If cavitation would be neglected the pressure distribution in the lubricant of a bearing with both a converging and diverging region would contain negative pressures in the diverging region. A general form of this pressure distribution for a continuous, incompressible lubricant is given in Figure I.6. From this figure, it can be seen that the load capacity of the bearing would essentially be zero, as the positive pressure region (in the converging part of the bearing wedge) cancels out with the negative pressure region (in the diverging part of the bearing wedge). However, it is normally observed that the pressure in the divergent region is approximately constant and around the saturation pressure (often close to ambient pressure, as the lubricant is often exposed to ambient pressure for long periods of time). This asymmetrical pressure distribution creates a load-carrying net force normal to the bearing surface. For this reason, it is important to include a cavitation model to properly model bearings with a convergent-divergent lubricating film (e.g. journal bearings). Some boundary conditions to model this are half-Sommerfeld (Gümbel's model), Reynolds (Swift-Stieber) model and JFO model (for which

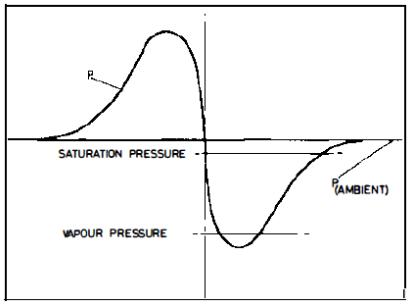

Figure I.6: Pressure distribution in convergent-divergent lubricating film. Taken from [78].

several algorithms exist to improve implementation, see subsection I.3) [76, 77]. These (and more) cavitation models will be discussed in more detail in subsection I.3.

I.2.6. Sommerfeld number

An important parameter in bearing design is the Sommerfeld number. The Sommerfeld number is defined as in Equation I.8 where F_{mag} is the total load capacity, L the length of the bearing, η the viscosity of the fluid, N the surface speed, ΔR the radial clearance and R_S the shaft radius. For a specific shaft diameter and length, the Sommerfeld number is only a function of the eccentricity. Using design graphs, one can find the Sommerfeld number for a specific L, D (shaft diameter) and eccentricity to select the operating parameters for an optimum performance [2]. In literature, the bearing performance parameters are sometimes also plotted versus the Sommerfeld number.

$$\Delta = \frac{F_{mag}}{LN\eta}\left(\frac{\Delta R}{R_S}\right)^2 \tag{I.8}$$

I.3. Models for hydrodynamic bearings and MR fluids

This chapter dives into the models needed to model hydrodynamic bearings lubricated with MR fluid. The equations used to model fluid flow are discussed in subsection I.3 followed by the models to describe the flow of suspensions in subsection I.3. Section 4.3 describes the rheological models available and used in literature for MR fluids. Section 4.4 summarizes the cavitation models available and finally, the effect of including temperature in the models is discussed in subsection I.3.

I.3.1. Fluid flow

Fluid flow is generally described using the Navier-Stokes equations in combination with a continuity equation (to include mass conservation). Simplifications are however normally applied to these equations to make them easier to solve. For hydrodynamic bearings many simplifying assumptions can be made, resulting in the much simpler Reynolds equation. The most important simplification is neglecting the inertial forces, but all the necessary assumptions are given in Appendix C. The Reynolds equation in 2D is given in Equation I.9 [1], where h is the film thickness, ρ the fluid density, η the viscosity, p the pressure and U_1, U_2, V_1 and V_2 the velocity of the boundaries in x- and y-direction respectively (where y is in the longitudinal direction for a journal bearing and z is in the direction of the film thickness).

$$\frac{\partial}{\partial x}\left(\frac{\rho h^3}{12\eta}\frac{\partial p}{\partial x}\right)+\frac{\partial}{\partial y}\left(\frac{\rho h^3}{12\eta}\frac{\partial p}{\partial y}\right)=\frac{U_1+U_2}{2}\frac{\partial \rho h}{\partial x}+\frac{V_1+V_2}{2}\frac{\partial \rho h}{\partial y}+\frac{\rho h}{2}\frac{\partial}{\partial x}(U_1+U_2)+\frac{\rho h}{2}\frac{\partial}{\partial y}(V_1+V_2)+\frac{\partial \rho h}{\partial t} \tag{I.9}$$

In hydrodynamic bearings it is often assumed to only consider the wedge effect. This means that the surface velocity in y-direction is neglected (V_1 and V_2 are 0) and no vertical surface velocity ($\partial h/\partial t = 0$) is present. Furthermore, incompressible fluid is often assumed (so ρ can be cancelled out). This results in the simplified Reynolds equation as given in Equation I.10, where $U = U_1 + U_2$.

$$\frac{\partial}{\partial x}\left(-\frac{h^3}{12\eta}\frac{\partial p}{\partial x}+\frac{Uh}{2}\right)+\frac{\partial}{\partial y}\left(\frac{h^3}{12\eta}\frac{\partial p}{\partial y}\right)=0 \tag{I.10}$$

Dowson [15] derived the generalized Reynolds equation which can also take into account variations in the fluid properties across the film. The generalized Reynolds equation may contain integrals that cannot be solved analytically. When the variation of the density and viscosity with respect to z (coordinate in the direction of fluid thickness) is negligible, the generalized Reynolds equation results back in the Reynolds equation. To implement non-Newtonian fluids in the Reynolds equation (which is the case for MR fluids) the generalized Reynolds equation needs to be modified accordingly as the viscosity is not constant anymore.

I.3.2. Flow of suspensions

MR fluids are a suspension of solid particles. There are two methods of modeling the flow of suspensions, namely the continuum and discrete approach. In the continuum approach the suspension is considered as one homogeneous phase. The main issue with this method is to find a proper rheological model that accurately predicts the flow behaviour and experimental measurements are generally needed to derive the rheological model. The discrete approach is based on a two-phase flow consisting of fluid with dispersed particles and the movement of fluid and particles is modelled separately. It is a more general approach; however, the complexity and computational costs are very high [30]. Furthermore, the exact shape and size of individual particles is often unknown. For these reasons, the continuum approach is used in literature to model hydrodynamic bearings lubricated with MR fluids and will also be used in this thesis. Moreover, the exact movement of the particles is not of interest as this thesis will focus on the bearing performance. The rheological models used for the continuum approach are discussed in the next section.

I.3.3. Rheological models for MR Fluids

As explained theoretically in subsection I.1, MR fluids behave like (shear-thinning) Newtonian fluids in the absence of a magnetic field, but have a yield stress when an external magnetic field is present. Many viscoplastic rheological models exist; the most commonly used in literature are the Bingham plastic and Herschel-Bulkley model (see also section I.4). A summary of all the viscoplastic rheological models used for MR fluids is given in Appendix D [30]. All these models implement a yield stress which is characteristic for MR fluids. The Bingham, biplastic Bingham and biviscous models do not include shear thinning, whereas the other models do include this phenomenon (which is usually present in MR fluids). MR fluid flow in steady-state is mostly modeled using the Bingham plastic model; however, mainly for low shear rates (<1000 s^{-1}). To include the shear-thinning behavior of MR fluids, the Herschel-Bulkley model is often used [79]. The advantage of a cross-model like the Papanastasiou model is its better ability to capture the shear stress dependency on the shear rate over a large range of shear rates (as for low shear rates the relation is linear and for high shear rates shear-thinning is present).

There exist some models to predict the yield stress as a function of volume fraction, magnetic field strength and some constants (like the Dave or Ginder equations or STE model [80]. However, in literature the yield stress for different magnetic field strengths is usually based on measurements using a rheometer or on the lubricants data sheet. The apparent viscosity is then based on the combination of one of the described rheological models (Appendix D) and the plugged-in yield stress (for a specific magnetic field strength).

I.3.4. Cavitation model

As explained in subsection I.2, cavitation can play a significant role in a hydrodynamic bearing. Several boundary conditions exist to take this into account. The Full-Sommerfeld condition is the simplest boundary condition, but it does not take cavitation into account. It assumes the pressure to be zero at the edges of the wedge which means a large negative pressure occurs in the fluid, which is physically unrealistic and the negative and positive pressure cancel out resulting in zero load capacity. The Half-Sommerfeld (or Gumbel) boundary condition sets negative pressures equal to zero. This boundary condition is often applied in literature; however, this boundary condition is not mass-conserving and imposes a discontinuity in the flow. The Reynolds boundary condition (or ”Swift-Stieber” [81, 82]) is also not mass-conserving but differs slightly from the Half-Sommerfeld boundary condition as it states that in the diverging section there is a point where the pressure and pressure gradient are equal to zero. It works reasonably well for the establishment of film rupture but is inaccurate in the prediction of the reformation of the film. A widely accepted model that is mass-conserving is the JFO model [76]. Elrod created a much simpler way of implementing the JFO model in the Reynolds equation by means of a

switch function [83]. Vijayaraghaven and Keith [84, 85] modified the Elrod algorithm to further improve the computational efficiency. Woloszynski et al. [86] developed the Fischer-Burmeister-Newton-Schur (FBNS) algorithm, which is based on the Elrod-Adams algorithm but the complementarity constraint is replaced by a system of Fischer-Burmeister equations. This algorithm results in a continuously differentiable and unconstrained system of discretized equations and furthermore decreased computational time by two orders of magnitude compared to other algorithms [86]. Alakhramsing et al. [14] proposed a cavitation algorithm where both the mass fraction f and the pressure p are replaced by functions of the introduced variable ξ. The modified Reynolds equation is then solved for ξ and the pressure and mass fraction are found using the transformation functions. This method is similar to Elrod's algorithm, however has the advantage that the pressure and mass fraction functions are independent and can thus be optimally scaled for numerical stability. Some papers in literature indicate that a mass-conserving boundary condition is needed for accurate modeling of a hydrodynamic bearing and implementation of the JFO model is often used in literature [87]. The circumferential pressure development based on different boundary conditions is given in Figure I.7.

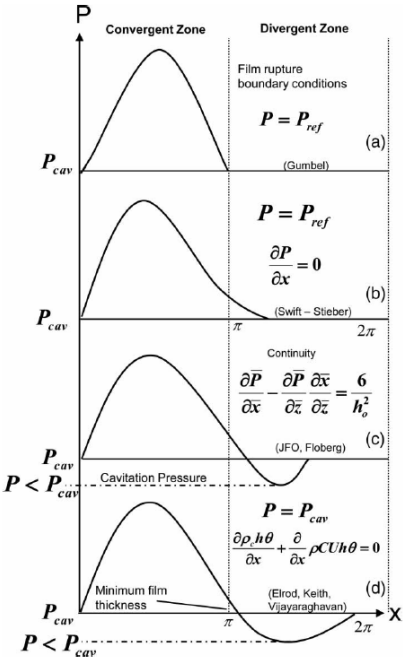

Figure I.7: Circumferential pressure development based on different cavitation models. a: Gumbel [88], b: Swift-Stieber [81, 82], c: JFO and Floberg and d: Elrod [83], and Vijayaraghavan and Keith [84, 85]. Taken from [76].

I.3.5. Temperature effect

The temperature has an effect on both the cavitation pressure and the viscosity. Including the effect of temperature in the simulation means having to solve the energy equation [89]. In literature this is usually not included in the theoretical model, as temperature changes are generally small and it increases the computational costs [6, 31].

I.4. State-of-the-art research on MR Lubricated bearings

In this section state-of-the-art research on magnetorheological fluid applications is summarized, focused on the application in hydrodynamic bearings. In subsection I.4 research on Bingham fluid application in hydrodynamic bearings is summarized. Section 5.2 presents the state-of-the-art on MR lubricated hydrodynamic bearings, divided into theoretical and experimental research. This is followed by research performed on hybrid bearings lubricated with MR fluid in subsection I.4. In subsection I.4 papers on two novel concepts of virtual and self-healing textures are presented. Section 5.5 summarizes the performed research on other applications of MR fluids, such as in hydrostatic bearings and

dampers, to give a broader view of the advantages and implementation of MR fluids. A quick overview of literature on hydrodynamic bearings lubricated with ER fluid is given in subsection I.4. Finally, the literature presented is summarized and categorized in subsection I.4 followed by the literature gap in subsection I.4.

I.4.1. Bingham fluid application in hydrodynamic bearings

MR fluids are often described as Bingham fluids, meaning that theoretical research on hydrodynamic lubrication with Bingham fluids (especially on the methods of simulation) is also of interest. Already in 1966, Batra [90] proposed an analytical solution for a journal bearing lubricated by a Bingham material. This solution was based on a formed core near the bearing at the location of maximum film thickness and a formed core near the shaft close to the region of minimum film thickness. He concluded an increase in load capacity and friction when a Bingham material was used as lubricant in comparison to a Newtonian fluid. Wada et al. [91] introduced a theory for lubrication using Bingham fluids and applied this to journal bearings [92]. They used grease as the lubricating fluid as this behaves as a Bingham fluid and validated their findings with experimental tests. They also concluded an increase in load capacity and friction for a Bingham fluid. Gertzos et al. [31] analyzed hydrodynamic lubrication by a Bingham lubricant using a three-dimensional CFD analysis and came to the same conclusion of increased friction and load capacity, which also increased with increasing yield stress. Furthermore, they suggested semi-active control of a journal bearing using MR or ER fluids.

Dorier and Tichy [93] proposed a method for implementing the Bingham fluid model in the generalized Reynolds equation using a regularization strategy, with the disadvantage that while it converges to the Bingham plastic fluid model (for increasing value of regularization parameter) the computational costs increase. Lampaert and van Ostayen [94] presented a new ”exact” thin-film lubrication simulation for a Bingham fluid which does not need any other approximations compared to the ones needed for the generalized Reynolds equation. The paper did not go into the effect of Bingham fluids on the bearing performance but focused on the new simulation method. This method was compared with the methods of Wada et al. [92] and Gertzos et al. [31] (both papers discussed above) and to the one-dimensional method of Tichy [95], and was found to be both in good agreement and have lower computational costs due to lower degrees of freedom and since no regularization method was used.

I.4.2. MR lubricated hydrodynamic bearings

The research available in literature on hydrodynamic bearings lubricated with MR fluid can be divided into purely theoretical research and experimental research (which most often also includes some theoretical analysis), which are both discussed below.

Theoretical research

Bompos and Nikolakopoulos [34] performed a three-dimensional CFD simulation of a journal bearing lubricated with MR fluid. They used a Bingham model where the shear stress is a function of the magnetic field intensity and used the Half-Sommerfeld boundary condition to model cavitation. The magnetic field is applied between the shaft and the bearing. As for the literature on the effect of using Bingham fluids, their main conclusions also were an increase in friction coefficient and load capacity. Babin et al. [96] created a mathematical model to simulate a journal bearing lubricated with MR fluid activated by means of eight solenoids placed circumferentially around the bearing. They only analyzed the effect of the current in the solenoids on the load capacity and found a significant increase and observed a non-linear relation with respect to the current in the solenoids.

Comparison of ferrofluid and MR fluid Laukiavich et al. [48] investigated the use of ferrofluid and magnetorheological fluid in a hydrodynamic bearing and their capability for active control. They did a three-dimensional simulation by solving the Navier-Stokes equations implementing the Bingham model and Half-Sommerfeld boundary condition to account for cavitation. The magnetic field was applied by means of eight solenoids placed circumferentially around the bearing surface for the MR fluids and by means of eight current-carrying wires for the ferrofluids. They observed only small effects on bearing behavior when using ferrofluids and concluded that due to the large amount of current required to generate small changes in load capacity, ferrofluids are unsuitable for controlling the performance of hydrodynamic bearings. In contrast, they found MR fluids can significantly increase the load capacity due to the active change in viscosity and proposed the usage of solenoids as the magnetic field source

to easily change the magnetic field. Just as in other literature, they did note the downside of using MR fluids which is the increased torque, although they deemed the torque increase as an acceptable side effect of an actively controllable hydrodynamic bearing. Laukiavich et al. also referred to two papers ([97, 98]) where it was found theoretically that ferrofluids could increase the load capacity while decreasing the friction coefficient. Several other papers are in agreement with this [99, 100]. However, Laukiavich et al. mention that when a realistic size hydrodynamic bearing ($\sim$50 mm shaft diameter) would be considered, the required current would be in the range of 200-600 A for a rotational speed of 200 rad/s, which is not deemed realistic.

Semi-active control using MR fluid Zapoměl and Ferfecki [101] investigated semi-active control of a hydrodynamic bearing by changing the provided current. They proposed a new type of bearing design situated at the end of the shaft as shown schematically in Figure I.8, enabling easy application of the magnetic field orthogonal to the flow direction of the lubricant. By changing the current they managed to shift the shaft towards the bearing center, achieving semi-active control. Zapoměl and Ferfecki published several papers based on this same bearing design. In [102] they performed theoretical research using ferrofluids-based magnetorheological fluid where a rigid rotor was excited by unbalance. They observed an increase in load capacity for increasing magnetic field, while not destabilizing the rotor vibration. In [103] they investigated the effect of applying a different force and current. They also presented the response of the bearing over time when introducing a current and changing the load on the shaft. Lastly, they found control to be limited as for too high current the vibration caused by the rotor unbalance becomes unstable. Zapoměl et al. [104] continued on this design and did research on using semi-active control to avoid disc collisions. Using this principle they were able to prevent impacts in a certain velocity interval or decrease the impact forces in case of a collision. Peng et al. [105] performed theoretical research on the control strategy for an active MR lubricated bearing using the Bingham model. They only magnetized the MR fluid locally at the bottom of the bearing and looked at the shaft locus under different currents. They found that with increasing current magnitude the orbit of the shaft decreases and stabilizes, meaning that it has the ability to suppress rotor vibration. Furthermore, they compared different algorithms to implement a PID controller and found the IGWO (improved gray wolf optimization) algorithm performed best in terms of response speed, overshoot and steady-state error, but it is noted that the robustness might not be sufficient under heavy load conditions (performed research was under a load of 1000 N at a rotating speed of 200 rpm).

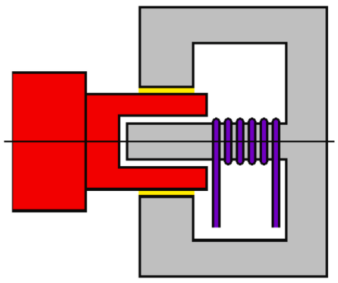

Figure I.8: Schematic drawing of the bearing design used in [101]. Taken from [101]

Stiffness and damping coefficients Some researchers looked at the change in stiffness and damping coefficients when using MR fluids in hydrodynamic bearings. Bompos and Nikolakopoulos [106] compared Newtonian fluids, MR fluids and ferrofluids in a journal bearing looking at the stiffness and damping coefficients. They performed the same type of three-dimensional CFD simulation as in [34]. They observed a high increase in the stiffness coefficient for MR fluid and ferrofluid. Both also showed an increase in the damping coefficient, where ferrofluid even had a significantly higher damping coefficient compared to MR fluid. The problem of ferrofluids is however the lack of controllability, as the rheological properties do not change significantly in their off-state. Wang et al. [107] did a theoretical simulation investigating the dynamic characteristics using a Herschel-Bulkley model (taking shear-thinning into account) and implementing the Reynolds boundary condition for cavitation. Five different lubricants were compared: Newtonian fluid, MR fluid in off-state, MR fluid in on-state and a weak and strong shear-thinning MR fluid. They concluded that MR fluid only increases the load capacity if the shear-thinning effect is not large. Moreover, they concluded that both stiffness and damping are

increased, where the stiffness increase becomes more significant for higher rotating speed. Though, a strong shear-thinning effect can limit the increase or even cause a decrease in stiffness and damping coefficients. Their overall conclusion is that shear-thinning should be taken into account when choosing MR fluids. Wang et al. [108] analyzed the stiffness and damping properties of a (semi-) floating ring bearing by means of a simulation with the Herschel-Bulkley model implemented. The rotating floating ring limits the shear rate and thus the shear-thinning effect of the MR fluid. Furthermore, they found a weaker magnetic field in the inner ring, limiting the friction increase compared to an ordinary journal bearing. Moreover, they concluded that the damping coefficient increases more due to the external magnetic field than the stiffness coefficient and that the damping coefficient improvement is largest for small eccentricity.

Experimental research
Next to the purely theoretical research presented, quite some experimental research has been performed, which will be discussed here.

Comparison of ferrofluid and MR fluid
The first experimental research on hydrodynamic bearings lubricated with MR fluids is performed by Urreta et al. [11]. They compared ferrofluid and MR fluid and also looked at the difference between a carbon steel (magnetic) and stainless steel (non-magnetic) shaft. The magnetic field was applied by means of two electromagnets on opposite sides of the bearing. The magnetic field strength was not varied, but only turned on and off. For the ferrofluid they found the effect to be very low due to a small rheological change of the ferrofluid and thus deemed it not suitable as an active lubricant for a journal bearing. For the MR fluid they did find an increase in load capacity, mainly for lower velocities. The effect on the friction coefficient was not measured. Moreover, they found the carbon steel (magnetic) shaft to have a higher load capacity and the locus to be more stable and linear compared to the non-magnetic shaft. This is probably due to the magnetic field being stronger in the radial direction (normal to lubricant flow velocity) due to the magnetic shaft. Bhat et al. compared the friction in a hydrodynamic journal bearing lubricated with ferrofluid and MR fluid for currents of 0, 10 and 18 Ampere. They found an increase in frictional force for MR fluid under the influence of an increasing magnetic field, whereas the frictional force did not change under the influence of a magnetic field for ferrofluid. They mentioned that a large amount of energy would be required to create very small changes in the viscosity of ferrofluids, which makes MR fluids more applicable for the intended application in this thesis.

Variable magnetic field strengths
Just like in the paper of Bhat et al. [109], several papers have been published in which tests are performed for different magnetic field strengths, instead of just the comparison between MR fluid with and without an external magnetic field. Vaz et al. [110] (same setup as used by Bhat et al. [109]) experimentally investigated the frictional force in an MR lubricated hydrodynamic journal bearing. They only performed measurements on the frictional force in the hydrodynamic lubrication regime and concluded an increase in frictional force for increased current through the coils (measurements were performed for 0, 10 and 18 Ampere). Zhang et al. [111] investigated the performance of a rubber stern bearing test ring with MR fluid. Here, the bearing was loaded axially and the magnetic field was applied in axial direction as well. The magnetic field strength was varied between 10mT, 30mT and 50mT. Next to an increase in the load capacity for increasing magnetic field, a decrease in friction coefficient was found. However, it was deduced from the numerical model that this decrease was mainly due to an increase in the load capacity.

Moles [10] wrote a PhD thesis on actively controllable hydrodynamic journal bearings using MR fluids. He both theoretically and experimentally investigated the performance of a hydrodynamic journal bearing under different magnetic field strengths by means of eight solenoids placed circumferentially. For his theoretical model, he used a modified Reynolds equation implementing the Herschel-Bulkley model and the Elrod cavitation model. He found numerically that for most combinations of speed and eccentricity ratio, an increase of 20% in the load capacity was achievable. Furthermore, the critical mass, the mass that the bearing can support while maintaining stable operation, was increased by 30% when applying a magnetic field. He also noticed that with increasing magnetic field strength the attitude angle generally increases slightly. Mainly at higher eccentricity ratios the steady-state position is noticeably altered. A dynamic analysis was performed to observe the response of the bearing to a small load increase under the influence of an applied magnetic field. This analysis showed that the

applied magnetic field eliminates the overshoot and oscillations in position and significantly reduces the total deflection from the original steady-state position. Removing the electromagnets in the diverging region of the bearing had minimal effect on the load capacity (except for the lowest rotational speed of 250 rpm or at an eccentricity ratio of 0.1). The effect on other parameters like the attitude angle, pressure distribution and fluid flow rate was also minimal.
For his experimental tests the magnetic field was varied by performing measurements with a current of 0, 10 and 20 Ampere. His experimental tests showed a decrease of 15-50% in eccentricity ratio with increasing magnetic field strength, depending on the rotational speed (indicating an increase in load capacity as the applied load was kept constant). Furthermore, an increase of 3-4.5% in frictional torque was measured (again depending on rotational speed). Another test was performed where half of the solenoids, on the low-pressure side of the bearing, were turned off. This test was only performed for one specific rotational speed, but showed a comparable (even slightly lower) eccentricity ratio decrease as when all solenoids were turned on. It was noted that the variability when half of the electromagnets were turned off was noticeably higher, indicating some introduced instability. This measurement implies that the magnetic field on the low-pressure side is not needed to increase the load capacity. More research on this principle, where a local magnetic field is used instead of a global magnetic field in the entire bearing, is discussed in the next section.

Local magnetic field
Quinci et al. [5] performed research on a journal bearing where only the lower section was magnetized (using 35 permanent magnets) to minimize the friction while still maintaining the increase in load capacity. They however still found a high increase in friction. As they used permanent magnets in their configuration they could not turn off or lower the magnetic field (so could not compare the MR fluid with and without an external magnetic field) and they suggested using electromagnets in further research. Moreover, they mentioned they used MR fluid which was not optimized for the specific hydrodynamic application. Lastly, they noticed their FEM and experimental results to generally be in good agreement; however, deviating more for higher operating speed. They attributed this to the exclusion of thermal effects (temperature increase during operation) in the numerical model, which is mainly important for higher operating speeds. Van der Meer et al. [6] continued on the work of Quinci et al. where the journal bearing was again locally magnetized but now by three permanent magnets at the bottom of the journal bearing. Measurements were also performed when the magnets were removed to compare the MR fluid in on- and off-state. The MR fluid was modified to have a viscosity below that of the reference oil at high shear rates and the mass fraction of the particles was reduced from 70 to 20%. They managed to obtain lower friction values with the MR fluid compared to the base oil; however, due to the lower viscosity the transition speed was increased a bit (meaning a decrease in load capacity). Their next step is to find a combination of an MR fluid and a magnetic field that results in a lowered transition speed and minimal friction increase. Their numerical model assumed the MR fluid to be a Newtonian fluid and they used the JFO boundary condition to include cavitation. The numerical and experimental results were in pretty good agreement and the observed differences were attributed to the isothermal approximation and the excluded shear-thinning effect of the MR fluid (both temperature increase and shear-thinning effect decrease the viscosity in the experimental tests).

Stiffness and damping coefficients
Like for the theoretical research, some experimental research was also primarily focused on the stiffness and damping coefficients. Bompos and Nikolakopoulos [112] did experimental research on the dynamic behavior of an MR lubricated journal bearing using an impact excitation method and compared the results when the magnetic field was turned on and off. They found a decrease in the shaft orbit of 75% when applying the magnetic field (the magnetic field was applied by two lateral coils). Furthermore, a decrease in eccentricity was also observed. In terms of stiffness and damping coefficients, they found a large increase for the MR fluid under the influence of an external magnetic field, although the exact changes in these coefficients differ depending on the direction (coefficients differ in x- and y-direction). Wang et al. [113] experimentally investigated a floating ring bearing with MR fluid and focused on the rotordynamic coefficients (similar to their theoretical research in [108]). The magnetic field was applied by means of 4 solenoids placed around the bearing, with opposing magnets having the same polar orientation. The applied current was varied between 0, 0.8, 1.6 and 2.4 Ampere. They found an increase in stiffness and damping coefficients when a magnetic field was applied and thus the ability to change these coefficients by changing the magnetic field.

I.4.3. MR lubricated hybrid bearings

A lot of (mainly theoretical) research has also been performed on hybrid bearings lubricated with MR fluid. As hybrid bearings are a combination of a hydrostatic and a hydrodynamic bearing, many papers still provide interesting findings with respect to the effect of MR fluids on the performance of hydrodynamic bearings. The papers are again subdivided into purely theoretical research and experimental research.

Theoretical research

The theoretical research on hybrid bearings lubricated with MR fluid can be categorized by the shape of the hybrid bearing, namely: straight journal bearings (both the shaft and the bearing housing are straight), conical journal bearings and spherical journal bearings.

Straight hybrid journal bearing

Sahu and Sharma [114] created an FEM simulation of a herringbone-grooved hybrid slot-entry journal bearing. Apart from the alteration in the shape and angle of the herringbone-grooves they also investigated the effect of MR fluid. They found, in line with the other presented literature, an increase in the minimum film thickness, frictional torque, and stiffness and damping coefficients when using MR fluid. In addition, they found an improvement in the stability threshold speed. The textures caused the minimum film thickness to decrease, but the usage of MR fluid counteracted this undesired effect.

Sahu et al. [115] investigated the effect of misalignment and surface irregularities on an MR fluid hybrid slot-entry journal bearing. The magnetic field is applied by two solenoids on both sides of the bearing, creating a magnetic field through the bearing which is not always perpendicular to the flow direction of the lubricant. They found that the application of MR fluid increases the minimum film thickness (also in case of misalignment which decreases the minimum film thickness, so the MR fluid can be used to counteract the minimum film thickness decrease due to misalignment), the frictional torque, stiffness and damping coefficients and also improves the stability threshold speed.

Conical hybrid journal bearing

Sharma and Kumar [116] looked at a roughened conical hybrid journal bearing and found that MR lubricant improves bearing performance at the cost of frictional power loss. Sahu et al. [117] investigated MR lubricated slot-entry hybrid conical journal bearings with texturing arrangements. They theoretically investigated different texturing arrangements, semi-cone angles and the influence of MR fluid versus a Newtonian fluid. Just like in [115] it was found MR fluid increases the minimal film thickness, frictional torque, stiffness and damping coefficients and stability threshold speed. Here, it was found that MR fluid can be used to counteract a decrease in damping coefficients due to the texturing or to counteract the decrease in stability threshold speed due to a higher semi-cone angle.

Spherical hybrid bearing

Sharma and Tomar [118] investigated a hybrid hole-entry spherical journal bearing with micro-grooves by means of a FEM model. Again, it was found that the general bearing performance improved due to MR fluid (increased minimum film thickness, increased stiffness and damping coefficients, lower lubricant flow rate and higher stability threshold speed) at the cost of an increase in frictional torque. Sharma and Agrawal [119] performed an analysis of a spherical hybrid thrust bearing considering the influence of surface irregularities and came to a similar conclusion of improved bearing performance with increased frictional power loss. Tomar et al. [120] did similar research; however, on a hole-entry spherical hybrid journal bearing. The findings concerning the bearing performance when using MR fluid were again in accordance with the other papers on hybrid bearings discussed above.

Experimental research

Urreta et al. [121] looked into the application of a hybrid journal bearing for high-precision spindles of machine tools. The magnetic field was applied in the same way as for [11], by means of two solenoids. They found 50% higher load capacity and stiffness. However, as the bandwidth of the system was found to be below 5 Hz, they concluded that active control by magnetic fluids cannot be considered for compensation of the unbalance in machine tool spindles shafts.

I.4.4. MR lubricated bearings with virtual or self-healing textures textures

De Graaf [70] showed that by means of a local varying magnetic field and MR fluid, a virtual (rheological) MR texture can be formed. Due to the local magnetic field, the apparent viscosity of the MR fluid can

be increased to the point of it behaving as a solid. He then showed that this virtual texture can produce a load capacity even when no solid part is formed, due to the locally increased apparent viscosity. He furthermore discovered that if a magnetic field with a large gradient was applied to a thrust bearing with MR fluid, the magnetic particles would be pulled from the flow. In this way, the particles will pile up and form a surface texture. This formed texture has the same effect as normal bearing surface textures and generates a load capacity. Compared to normal surface textures, it was suggested that these textures are self-healing, as the particles that are worn off remain in the closed system and sediment back onto the texture. More literature is available on both of these concepts, which is discussed below.

Rheological textures
Lampaert et al. [122, 123] theoretically investigated the concept of rheological (virtual) textures in a hybrid journal bearing. The rheological textures were created using activated regions where the viscosity is increased and a yield stress is introduced. By means of rheological textures, the load capacity of the bearing was enhanced, again at the cost of an increase in friction.

Self-healing textures
Van der Meer [124] created a numerical model to simulate the self-healing behavior suggested by de Graaf, alongside experimental tests performed by Lucieer [125] on a vertical journal bearing. The numerical model of van der Meer was constructed to predict the steady-state shape and size of the surface textures. Furthermore, the effect of the textures on the load capacity and friction was modeled. First, the model was compared to the results of de Graaf [70], qualitatively indicating that the texture size scales with shear stress. The numerical model was compared with the experiments of Lucieer [125] but no correspondence was found, measuring differences in torque of 50-100%. The differences were argued to be caused by the whirl present in the experiments. His model was also used to demonstrate the possibility of generating self-healing herringbone textures in a journal bearing. He concluded that this method can be used to stabilize the bearing. Furthermore, by introducing a difference in the magnetic field strength of the individual magnets, a load capacity was generated at zero eccentricity, which is not obtained with standard herringbone textures. Lucieer demonstrated that increasing magnetic field strength results in larger textures but also in increased torque. He also concluded that a minimum critical particle mass percentage exists in order to ensure continuous texture restoration and uniformity of texture on the different magnets. Van Kuik [126] modeled the particles in an MR fluid by means of a discrete model, in order to simulate the transition from structures to textures. He found that the sedimentation of the particles was not caused by the attractive force of the magnet by itself but by a combination of this force and the deformation of the particle structures. When the shear rate was zero, there was only a very slight increase in the particle volume near the magnet. Higher shear rates cause the particle chains to deform and particles to aggregate at locations of highest magnetic field gradients and particles will build up on this aggregation. This finding of particle aggregation behind the magnet(with respect to the flow direction)is in line with the findings of Lucieer [125]. The main relevant conclusion from these papers on the intended application (in this thesis) of MR fluid in a hydrodynamic bearing is that a too large magnetic field gradient will cause sedimentation and texture generation. Therefore, the aim should be to design a uniform, or at least without large gradients, magnetic field.

I.4.5. MR fluid in other applications
Apart from lubricating hydrodynamic and hybrid bearings, research has also been performed on MR fluid in other applications, such as dampers, clutches, breaks, valves and hydrostatic bearings [49]. In fact, MR fluids have already been commercially applied in semi-active dampers and rotary brakes since the mid-90s. MR dampers can rapidly acquire high damping force while using little power by applying a magnetic field through an electromagnet to the MR fluid and are, among others, used in the automotive industry [127–129]. Zhu et al. [129] addresses several different coil designs used in dampers, which can be used as inspiration for MR bearings. In dampers the coil is often placed around the moving part/shaft of the damper, whereas for bearings the electromagnets are generally placed around the bearing housing.

Hesselbach and Abel-Keilhack [130] performed research on MR lubricated hydrostatic bearings aiming to create a constant bearing gap for a changing payload. By changing the magnetic field, they managed to achieve a large change in bearing gap at constant payload, while only using a very limited amount of power. Furthermore, they showed that it is possible to use this principle to achieve a constant bearing

gap. Guldbakke and Hesselbach [131] continued on this research and created a magnetohydrostatic bearing (hydrostatic bearing in which the pressure is generated by the gradient of the magnetic field), which only showed a limited load capacity. Furthermore, they concluded in this paper it is possible to achieve nearly infinite stiffness for moderate gap sizes in MR lubricated hydrostatic bearings with a closed-loop system. More research on hydrostatic bearings lubricated with MR fluid can be found in literature (although limited) such as Lampaert and van Ostayen [132], who showed that it is possible to recreate the pressure profile in a hydrostatic bearing solely using a magnetic field.

I.4.6. ER lubricated hydrodynamic and hybrid bearings

Some limited research has also been performed on hydrodynamic [35, 133–140] and hybrid bearings using ER fluid [141–148]. Very similar types of tests are performed, measuring or determining load capacity, friction and stiffness and damping coefficients. No significantly different results compared to the results found in the extensive literature review on MR fluids in hydrodynamic or hybrid bearings were found. Therefore, a more in-depth discussion of this literature is omitted.

I.4.7. Summary of state-of-the-art

As quite a lot of literature is presented in this chapter, the references have been summarized and categorized in Table I.1. First, they have been categorized by type of fluid, followed by application type (different rows). The papers have then been assigned to their corresponding categories regarding research model or method (type of model used for the simulations and if experimental tests were performed), topic of findings (on what parameters were conclusions drawn in the papers), field strength (are several different field strengths analyzed or were only the situations with and without an external field compared) and field application (was the external field applied locally or globally through the entire bearing or device). The field strength and field application categories are interesting, as this thesis will focus on finding the best field strength and shape for specific operating conditions (and will thus compare several field strengths and different shapes of local magnetic field). The category ”semi-active control” included only papers that performed analysis in which the magnetic field was changed during bearing operation. The papers mentioned did this by analyzing the response of the bearing due to turning the magnetic field on. No papers were present in which the magnetic field was changed based on the operating conditions. This table was used to identify the gaps in the state-of-the-art but can also be used to quickly search for applicable papers.

As the MR fluids used in the experimental research differ significantly and there has not been a conclusion on what MR fluid performs best, the different MR fluids used in the experimental research are summarized in Table J.1. The base viscosity (in the absence of a magnetic field) is included at low shear rate (approximately 1000 s^{-1}). Papers that did not include any information on the fluid used are omitted. Many theoretical papers were based on an MR fluid of Lord Corporation and the details are included in Table J.2.

I.4.8. Literature gap

To conclude, the existing literature on MR lubricated hydrodynamic bearings agrees on the findings that MR fluid can be used in hydrodynamic bearings to increase load capacity, stiffness and damping coefficients at the cost of an increase in friction. MR fluid application in e.g. dampers and valves is far developed and even commercially available, while MR fluid application in (hydrodynamic) bearings is still being researched. Existing literature focuses mainly on the hydrodynamic lubrication regime and does not take into account the change in the transition speed (or equivalently the maximum load capacity at a specified minimum film thickness), except for the paper of van der Meer [6]. Furthermore, most literature considers a constant magnetic field, which does not change with bearing velocity or applied load/load capacity. Some research has been done on locally applied magnetic fields, but not on the optimization of the exact shape of the magnetic field. Semi-active control of the bearing while observing and minimizing the friction has, to the knowledge of the author, not been investigated to date. In subsection I.4 it can also quickly be seen that for MR lubricated hydrodynamic bearings the research on semi-active control, especially in combination with a local magnetic field and experimental tests, is very limited and the combination of the three does not even exist yet.

Table I.1: Categorized State-of-the-art papers

Type of fluid	Application	Research model or method					Topic of findings					Field strength			Field application	
		RE with Bingham	RE with Herschel-Bulkley	RE with other fluid model	CFD (Navier-Stokes)	Experimental	Load capacity	Friction	Stiffness/Damping	MR fluid versus ferrofluid	Texture formation	Multiple	1 setpoint (on/off)	Semi-active control	Local	Global
MR	Hydrodynamic	[5, 11, 105, 111]	[10, 107, 108, 113]	[6, 70, 96, 101–104, 124]	[34, 48, 106, 112]	[5, 6, 10, 11, 109–113, 125]	[5, 6, 10, 11, 34, 48, 70, 96, 101–104, 107, 111, 112, 124]	[5, 6, 10, 34, 48, 108–111, 124, 125]	[106–108, 112, 113, 124]	[11, 48, 109]	[70, 124, 125]	[10, 34, 48, 70, 96, 101–105, 108–111, 113, 124, 125]	[5, 6, 11, 106, 107, 112]	[101–105, 112]	[5, 6, 10, 70, 105, 124, 125]	[10, 11, 34, 48, 96, 101–104, 106–113]
	Hybrid	[114, 115, 117, 118, 120, 122]	[116, 119, 121]			[121]	[114–122]	[114–120, 122]	[114–121]			[117–120, 122]	[114–116, 121]		[122]	[114–121]
	Other applications				[126, 132]	[130–132]	[130–132]				[126]	[130–132]	[126]		[126, 132]	[130, 131]
ER	Hydrodynamic	[135–140]			[35, 133, 134]	[135, 138]	[35, 133, 134, 136–140]	[35, 133, 136]	[137–140]			[35, 133–140]				[35, 133–140]
	Hybrid	[141–148]					[141–143, 145–148]	[141, 143, 145, 146]	[141–148]			[142, 144, 148]	[141, 143, 145–147]			[117, 141, 142, 144–148]
Bingham	Various	[90–94]			[31]	[92]	[31, 90, 92]	[31, 90, 92]				Not applicable			Not applicable	

J

MR fluids used in literature

Paper	Name	Company	Carrier fluid	Mass/volume fraction [%]	Viscosity @40°C $[Pa \cdot s]$
Urreta et al.[11]	MRF-122-2ED	Lord Corporation	Hydrocarbon oil	Mass. 72	0.042
Bhat et al. [109]	n/a	Homemade	Silicone oil	Vol. 10/20	n/a
Quinci et al. [5]	n/a	Unknown	Hydrocarbon oil	Mass. 70	n/a
van der Meer et al.[6]	Modified MRHCCS4-A	Liquids Research Ltd.	Hydrocarbon oil	Mass. 20	$\sim$ 0.09
Moles [10]	n/a	Homemade	ISO 32 hydraulic oil	Mass. 9.24	0.17
Bompos and Nikolakopoulos [112]	n/a	Homemade	SAE-10W oil	Mass. 20	n/a
Wang et al. [113]	n/a	Homemade	ISO VG32 turbine oil	Mass. 30	$\sim$0.032
Urreta et al. [121]	MRF-122-2ED	Lord Corporation	Hydrocarbon oil	Mass. 72	0.042
Lucieer [125]	MRF-122-2EG	Lord Corporation	Hydrocarbon oil	Mass. 72	0.042
Lampaert and van Ostayen [132]	n/a	Homemade	Mineral oil	Mass. 72	0.073

Table J.1: Properties of the MR fluids used in literature. Magnetic particles were made from (carbonyl) iron for all fluids. Viscosity is based on low shear rate (approx 1000 s^{-1}).

Name	Papers	Mass fraction [%]	Viscosity @40°C $[Pa \cdot s]$	Density $[g/cm^3]$
MRF-122-EG	[70, 107, 114–117, 119, 124]	72	0.042 $\pm$ 0.020	2.18-2.48
MRF-122-2ES	[118]	72	0.042	2.28-2.48
MRF-122-2ED	[120, 121]	72	0.042	2.28-2.48
MRF-132-DG	[34, 105, 106, 130, 131]	80.98	0.112 $\pm$ 0.02	2.95-3.15
MRF-140-CG	[48, 96]	85.44	0.280 $\pm$ 0.070	3.54-3.74

Table J.2: Properties of the MR fluids used in theoretical literature. Fluids consist of hydrocarbon oil with iron magnetic particles. All fluids are from the company Lord Corporation. Viscosity is based on shear rate of 800-1200 s^{-1}, except for MRF-122EG for which it is based on a shear rate of 500-800 s^{-1}.